December 2018 Vol. 11 No. 2
ISSN 2005-9043

Leading to tomorrow

KIST Today

Korea Institute of Science and Technology

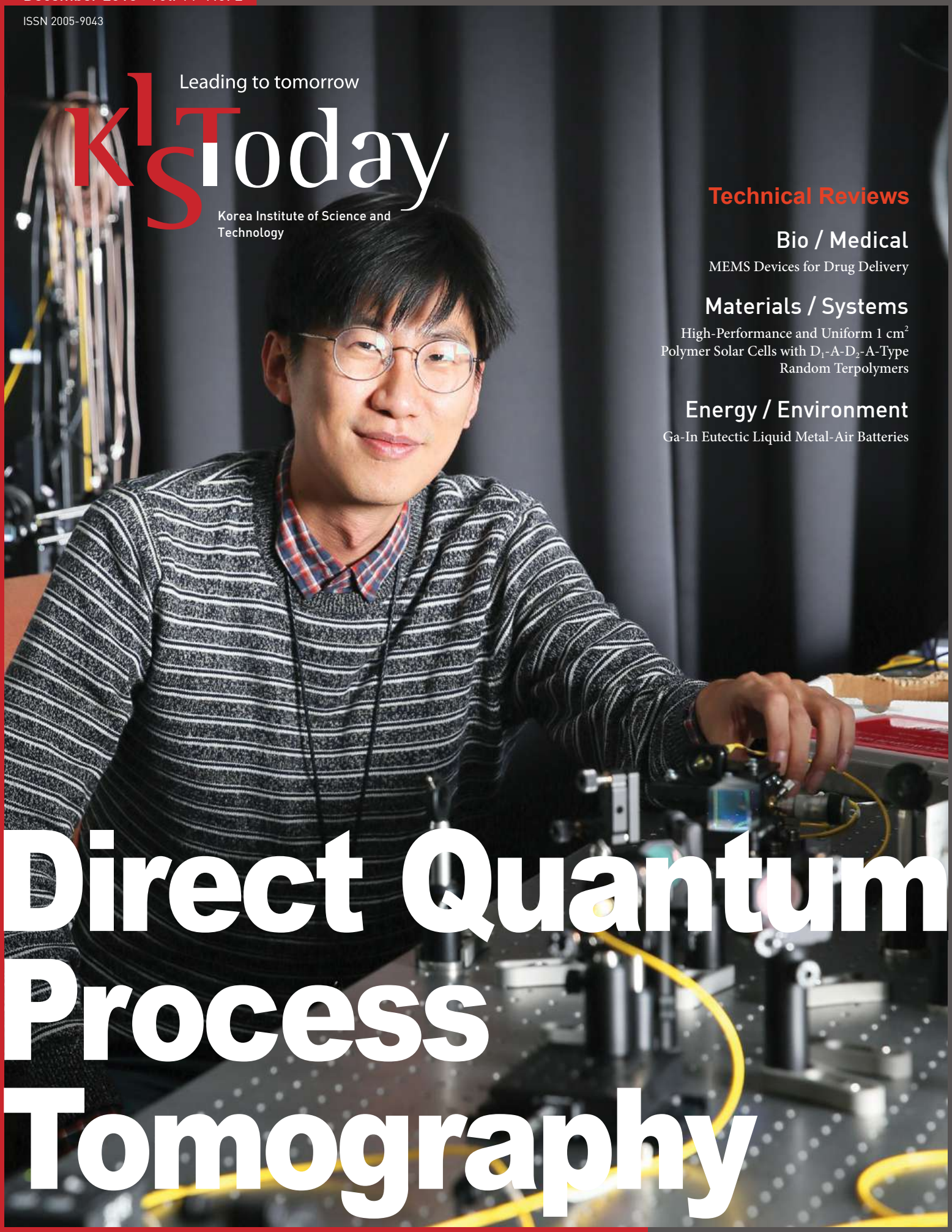

Technical Reviews

Bio / Medical

MEMS Devices for Drug Delivery

Materials / Systems

High-Performance and Uniform 1 cm^2 Polymer Solar Cells with D_1-A-D_2-A-Type Random Terpolymers

Energy / Environment

Ga-In Eutectic Liquid Metal-Air Batteries

Direct Quantum Process Tomography

Cover image_ Dr. Young Wook CHO Center for Quantum Information (see p.70 for interview)

Contents

Korea Institute of Science and Technology

5, Hwarang-ro 14-gil, Seongbuk-gu, Seoul 02792, Republic of Korea
Tel + 82-2-958-6179 www.kist.re.kr/en
E-mail hyhwang@kist.re.kr

Editorial Information

Editor-in-Chief Seok Jin YOON
Editorial Board Members Il Joo CHO, Hyun Kwang SEOK, Seok Won HONG, Hyung Joon KIM, Jong Ho LEE, Young Soon UM, Hye Jin LIM, Jung Hoon JEON
Managing Editor Hyun Young HWANG / hyhwang@kist.re.kr / +82-2-958-6179
English Advisory Services Anne Charlton / The Final Word Editing Services / the_final_word@live.com

Foreword

Each year KIST faces new challenges. In 2018, we launched the K-DARPA Program to create innovative technologies for the public sector, where private investment is scarce, particularly in regard to national security and public safety. Our challenge is to find creative solutions to prepare for natural disasters or security threats and then make those technologies available to the private sector for the benefit of Korean companies as well as public welfare.

Another challenge is to secure source technology for the long term that will let us take advantage of the 4th Industrial Revolution. KIST is particularly focused on basic research that will lead to commercialized results within five to ten years. Examples include advanced robotics, big data and quantum computing. This issue's cover article on direct quantum process tomography illustrates the type of research at the heart of our efforts.

To maximize the benefits of our efforts, we continue to pursue convergence research with other institutions and companies both within and outside Korea. Our policies provide access to advanced equipment and facilities that many organizations would otherwise not have, and we actively share KIST's intellectual properties and demonstrated technologies to enhance the competitiveness of Korean companies.

As we look to the year ahead, we see many hurdles on the horizon, but we remain confident it will bring us one step closer to achieving new integrated technologies that can beneficially transform the lives of people around the world.

Dr. Byung Gwon LEE
President of KIST

Technical Review

MEMS
Devices for Drug Delivery

Il Joo CHO
Principal Researcher
Center for BioMicrosystems
Biomedical Research Institute

ijcho@kist.re.kr

Introduction

With the rapid development in novel pharmaceutical compounds and intervention, there is an increasing need for novel drug delivery systems that can address challenges associated with conventional drug delivery systems. For example, modern drug candidates include a wide spectrum of molecules, including large biomolecules (e.g., peptides and proteins) with low bioavailability, small molecules with poor water solubility, and potent drugs with narrow therapeutic windows. Due to this wide range of physiochemical and pharmacokinetic properties of modern drug candidates, conventional oral or intravenous administration might not be the most suitable route of administration. Evaluation of drug candidates and optimization of drug developments are thus limited by a lack of adequate delivery systems. In addition, with advances in diagnostic techniques, drug delivery is applicable not just to wound healing and immunology but also to cancer treatment, gene delivery, and insulin delivery [1], all of which require targeted drug delivery with controlled release. There are also areas in our body, such as the brain and the posterior eye segment, that are very challenging sites to target through conventional intravenous administration due to the physical barriers (i.e., blood-brain barrier and blood-retinal barrier) that separate the organs from blood circulation. One method for overcoming these difficulties is to formulate nanoscale delivery vehicles to enable site-specific targeted drug delivery with the goal of oral delivery of proteins, peptides, and even imaging nanoprobes [2-4]. Nanoparticle-based drug delivery enables targeted drug delivery to the desired regions, but reliable encapsulation of nanoparticle-size drugs with desired release characteristics are challenging to achieve [5].

Microelectromechanical systems (MEMS) is a promising microtechnology for developing novel drug delivery systems that address current challenges and can accommodate a vast variety of drug delivery applications. By offering miniaturization [4-7], integrations of multiple functions [8, 9], and electromechanical control [10-12], microtechnology allows

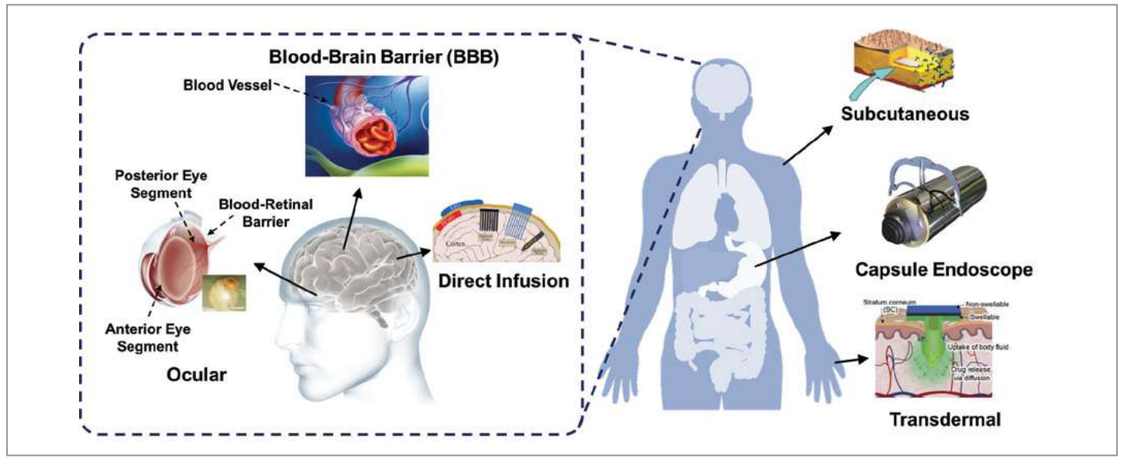

Figure 1 Schematic diagrams of various target organs and their associated physical barriers and targeting strategies using novel drug delivery systems enabled by microtechnology. The blood-brain barrier (BBB), stratum corneum, and retina-blood barrier are shown for brain, skin, and eye, respectively. All figures reprinted with permission.

delivery of a wide range of drugs with high therapeutic efficacy. Also, microtechnology enables localized drug delivery to challenging areas in the body by means of alternative routes of administration. Using MEMS technology, hundreds of thin microneedles can be precisely manufactured in a single array to deliver drugs without incurring harm or pain. In addition, while conventional drug delivery relies mostly on diffusion, MEMS micropump technology allows active control over drug release such as release rates and infusion volumes and provides ways to continuously supply drugs through a reservoir [13]. Thus, advances in microfabrication technology and biocompatible materials have expanded the capability of drug delivery systems in terms of target sites, route of drug administration, patient compliance, spectrum of deliverable drugs, and dosing procedures [14].

Not only to further advance existing drug delivery systems but also to accommodate the need for spatial-, temporal- and dosage-controlled release, it is important to understand the current challenges in the field. However, these challenges differ greatly depending on the drug candidates, target areas, and routes of administration. For instance, while the major challenge in targeting the brain and the posterior eye segment has been transcending the physical barriers, a recent challenge in developing advanced transdermal patches has been less concerned with overcoming the stratum corneum (SC) barrier than on controlling dosage duration (e.g., intermittently, as-needed, or over a long period). Thus, in this review, we first discuss the current challenges in targeting different areas of the body and then discuss recent works that have addressed these problems (Figure 1).

Drug Delivery to the Brain

Given a rapidly aging population, there is an increasing need for effective treatments for neurodegenerative diseases. As an alternative to surgical resection, localized drug delivery to the brain is one of the important therapeutic means to treat brain diseases such as brain tumors and Alzheimer's disease. However, unlike delivering drugs to most parts of the body, delivering drugs to the brain is not straightforward because of the existence of the blood-brain barrier (BBB). The BBB consists of epithelial-like tight junctions within the brain capillary endothelia and serves as a physical and biochemical barrier to keep most molecules from entering the brain. Only a small fraction of small-molecule drugs (i.e., molecules with a molecular weight below 400~500 Da and with high lipid solubility) can penetrate the BBB in a pharmacologically significant amount [15]. Thus, brain diseases that can be effectively targeted are limited in number. In addition, because of their high lipid solubility, these small molecules can penetrate through all biological membranes which consequently affects target specificity, increases the risk of side effects, and limits

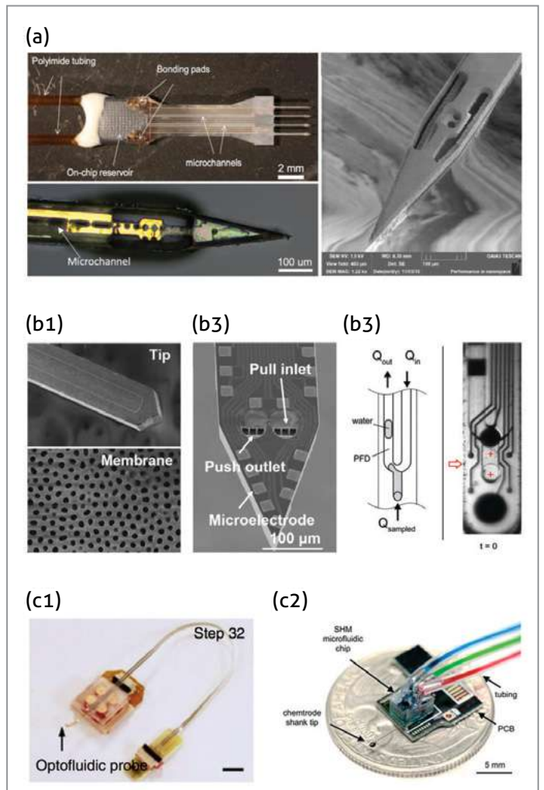

Figure 2 Microneedles with integrated microfluidic channels for brain infusion: (a) silicon-parylene hybrid structure with openings at the tip for the regrowth of neural tissues to enhance biocompatibility, (b1) microneedle integrated with U-shaped channels and nanopores at the tip for microdialysis, (b2) push-pull microneedle to sample neurotransmitters, (b3) droplet-based sampling microfluidics, (c1) fluidic channel integrated with a refillable, multi-drug chamber (scale bar: 5 mm), and (c2) neural probe integrated with microfluidic channel and interfaced with a PDMS chip which consists of 3 input channels, a micromixer, and 1 output channel. All figures reprinted with permission.

therapeutic efficacy. Therefore, various strategies from direct injection to non-invasive BBB disruption [11, 16], endogenous BBB transporter-mediated delivery [17], and transnasal route of administration [18] have been explored to overcome or bypass the BBB (Figure 1). In this review, we focus on two systems for drug delivery to the brain that benefit from microtechnology: transcranial direct brain infusion and BBB disruption using focused ultrasound.

Direct brain infusion is invasive but is the most effective means to deliver a known concentration of therapeutic agents to a specific location in the brain. There are three primary neurosurgical methods for human transcranial brain drug delivery: intracerebral implantation, intracerebroventricular (ICV) infusion, and convection-enhanced diffusion (CED) [19]. There are several factors that need to be considered in choosing the delivery method: desired infusion area, infusion speed, distribution of delivered drugs, area of tissue damage, and sensitivity to drug reflux. While intracerebral implantation and ICV infusion rely on diffusion of drugs from a concentrated source at the implanted sites (e.g., diffusion-based eluting polymer), CED uses external forces to push a bulk flow of drugs at a constant flow rate into the brain through a hollow cannula or needle [25]. Owing to the convective flow at the infusion site, CED allows for a homogeneous distribution of drugs over a longer distance (~cm) regardless of molecular size and the refluxed drugs are within the target volume. The minimum dimension of the cannula is limited by several factors such as fabrication technology and desired flow rate which is a function of viscosity and density of drug.

There are increasing efforts towards delivering drugs to the brain via the blood stream by overcoming the BBB. One promising strategy is to use focused ultrasound (FUS) to transiently disrupt or breach the BBB by applying a concentrated acoustical energy to a focal spot in the brain. Upon sonication, the induced BBB disruption lasts for several hours, after which the BBB disruption recovers to the baseline [20]. Thus, when a drug along with an ultrasound contrast agent (i.e., microbubble) is administrated through intervascular injection, the drug circulating in the blood stream enters the brain only at the location where the BBB is disrupted by sonication. The clinical need for this technology is expected to be tremendous because the FUS technology enables spatial- and temporal-controlled delivery to the brain while being non-invasive and applicable to a wide spectrum of drugs including DNAs [21], genes [22], small molecules [23], hydrophilic molecules [24], drug-loaded microbeads [25], and macromolecules [26]. Moreover, early studies on BBB disruption using ultrasound demonstrated that no apparent damage to surrounding parenchyma were induced by the technique [27]. In addition to targeting the brain, the FUS technology has been applied for drug delivery to other parts of the body through transdermal, transcorneal, and gastrointestinal routes of administration.

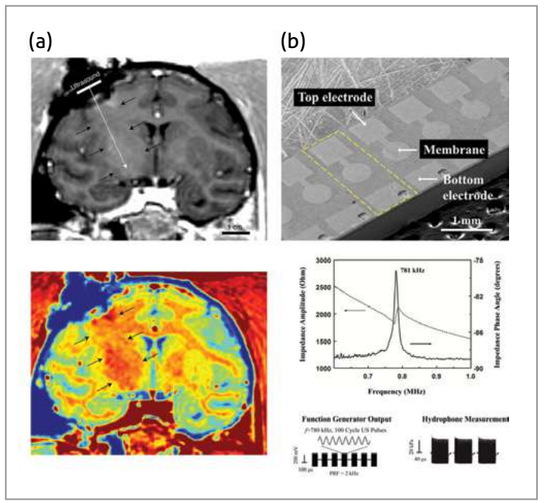

Figure 3 (a) MR image immediately after BBB disruption by pulsed ultrasound using the implanted ultrasound transducer (top) with a contrast-enhanced image (bottom). (b) the 16-element pMUT array with a resonant frequency of 781 kHz developed for *in vitro* neuromodulation. All figures reprinted with permission.

Ocular Drug Delivery

The eye is an interesting yet complex organ for drug delivery; the anterior segment is exposed and thus accessible externally through a thin layer of the cornea while the posterior segment interfaces with the internal vascular network through inner and outer blood-retinal barriers (Figure 1). Possible routes of administration for intraocular drug delivery include topical, systemic, intravitreal, and periocular routes. The topical route using eye drops and ointments is currently the most common for treating ocular diseases in the anterior eye segment. However, because of a continuous turnover of tears, clearance through nasolacrimal ducts, and low permeability of the corneal layer, less than 5% of a dose is absorbed into the eye [28]. Thus, application frequency or drug concentration must be increased to reach the therapeutically effective dosage. As a result, despite the accessibility, targeting the anterior segment is still challenging. It is even harder to target the posterior segment because of the physiological blood-retinal barrier and anatomical inaccessibility. Most ocular diseases that lead to visual impairments occur in this posterior segment making implantable drug delivery systems attractive alternatives for targeting diseases in this segment. Intraocular implants bypass or penetrate the barriers to increase the efficiency of drug delivery and there are a large number of potential implantable sites: vitreous space, pars plana, peribulbar, and intrascleral space. Implantable intraocular drug delivery systems are especially useful for ocular diseases such as cytomegalovirus (CMV) retinitis and proliferative vitreoretinopathy (PVR) which

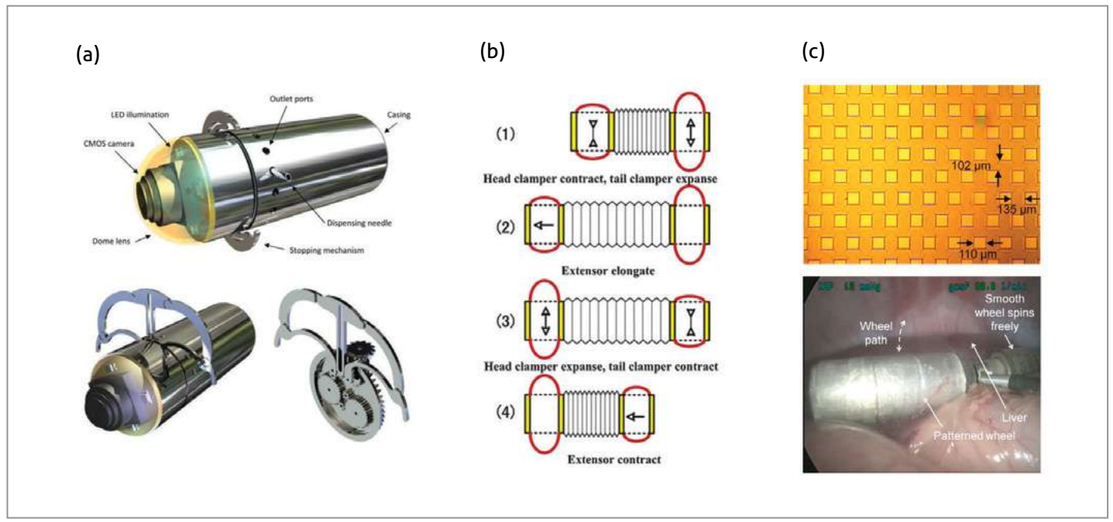

Figure 4 Micromotion and anchoring mechanisms for capsule endoscope: (a) microrobot based on legged mechanism where the bow-shaped legs extend widely and resist peristaltic pressure along the GI tract, (b) schematic of inchworm-like locomotion that enables capsule endoscope to crawl along the GI tract, and (c) wheel-based movement. All figures reprinted with permission.

require repeated drug injections and surgeries. In addition, these systems are suitable for treatments of chronic diseases with no other effective treatments, such as age-related macular degeneration (AMD), macular edema, and retinitis pigmentosa. Lastly, through localized delivery, implantable intraocular drug delivery systems allow administration of a large spectrum of drugs, including potent antiangiogenic agents and biomolecules. For general details on ocular drug delivery, readers are referred to [29]. These implantable systems have been tested with animals in the preclinical stage.

Gastrointestinal Tract Drug Delivery – Capsule Endoscopy

Unlike other parts of the body that require surgery for implantation, drug delivery to a specific location of the gastrointestinal (GI) tract can be achieved non-invasively by oral intake of drugs. However, gastrointestinal absorption along the GI tract depends greatly on many physiological, pathological, and pharmacological factors, such as regions, gastric emptying time, intestinal motility, and drug formulations [30]. Thus, targeted and efficient drug delivery using passive oral medication is challenging. Another possible means to deliver drugs in the GI tract is through the use of traditional endoscopes. However, the endoscope that enters either through the oral cavity or the anus does not provide access to the full GI tract. In addition, the traditional endoscope has low patient compliance. By contrast, the swallowable capsule endoscope is highly patient compliant and provides access to the entire GI tract [31].

Since the first introduction of a commercially available capsule endoscope in 2001, three small bowel capsules and one esophageal capsule have been approved by the U.S. Food and Drug Administration (FDA) while one colonic capsule is now available in Europe and Japan [10]. By integrating the drug delivery function with the capsule endoscope, spatial-, temporal-, and dosage-controlled drug delivery in the GI tract can be achieved. This targeted on-demand drug release not only enables direct treatment of GI diseases but also provides an efficient route of administration by targeting the regions with the highest drug absorption. For example, the small intestine is an attractive site for drug administration because of its high drug absorption ascribed to large surface area. Moreover, drug delivery to different regions of the GI tract is an important field of study for the pharmaceutical industry because understanding the different absorption rates across the GI tract provides useful information in determining the dosage form of a drug for sustained release [32]. Some of the passive devices have been utilized in human studies for colon targeting [33]. Since the intubation process can disturb the normal physiological function of the GI tract, the swallowable capsules can be utilized as an evaluation tool to study absorption characteristics for drug developments. In addition to the capsule endoscope, there is an increasing amount of research on developing GI patches which are completely passive systems that rely on various matrices of polymeric layers to achieve timed release in the GI tract. For details on GI patches, readers are referred to a comprehensive review on this topic [34].

Transdermal Drug Delivery

Although the history of microneedle technology is relatively long compared with that of other novel drug delivery systems, there are still unresolved challenges and desired features that require technological innovations. Transdermal microneedles are designed to penetrate stratum corneum but not deeply enough to reach nerve endings. Thus, secure positioning of the microneedles on the skin is important, especially regarding drug administration over an extended period of time. There has been a continuous effort to optimize the structure of microneedles as regards tip shape, length, and spacing. For instance, Seong, et al. have recently reported a bullet-shape microneedle array with water-swellable tips; upon insertion, the tips swell due to an uptake of biofluid and provide a strong mechanical interlock to the neighboring soft tissues [35]. Completely dissolvable microneedle arrays serve as another important area of interest in transdermal drug delivery, especially for vaccine delivery [36]. With advancements in polymeric fabrication and biotechnology, delivery of a wide range of drug candidates, including proteins, DNAs, and virus-based vaccines, is now also being actively investigated.

During the early stage of development, drugs infused through microneedles were diffusion-limited because of passive drug release. In order to enhance drug penetration and release rates, external forces were applied, such as electric field, ultrasound, and mechanical forces. These external forces can also be used as external stimuli for on-demand drug release [37]. If the stimuli are internally-generated physiological signals, a closed-loop or self-regulated drug delivery can be achieved; activation of drug release is determined by changes in the physiological signals through the use of bioresponsive vesicles [38]. This smart closed-loop approach could be useful

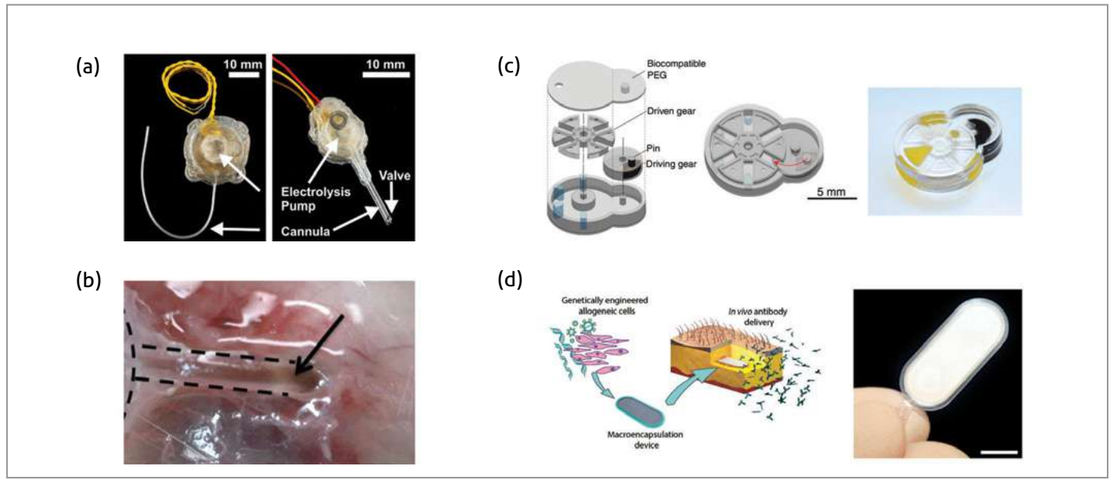

Figure 7 Subcutaneous implantable drug delivery systems: (a) photo of encapsulated electrolysis pump, (b) photo of biological responses to the implanted device over 28 days, (c) MEMS mechanical components such as driving gears and rotors fabricated using soft hydrogel materials, and (d) a biocompatible implant to deliver *in vivo* antibody delivery (scale bar: 750 μm). All figures reprinted with permission.

for diabetes patients as well as patients who require on-demand administration of analgesia over an extended period of time. Possible internal physiological signals include temperature, pH, glucose level, and enzyme concentrations. Design considerations for these systems include response rates of the closed-loop system, sensitivity to physiological signals, resolutions of the detectable signals, on/off ratios, local and systemic side effects due to biocompatibility, and the volume of drugs required to match long-term dosage of specific therapeutics.

Implantable Subcutaneous Drug Delivery

Microfabrication plays an essential role in implementing microdevices for transdermal drug delivery and subcutaneous implants, such as microneedles, micropumps, reservoirs, and encapsulation [39]. While transdermal drug delivery is minimally invasive, self-administrable, inexpensive, and highly patient compliant, subcutaneous implants are invasive with low patient compliance, but they do provide long-term administration in an order of years. Because of the difference in the nature of invasiveness, these two systems face different technological challenges and thus are discussed separately in this review.

Although implantation under the skin is subject to the issue of patients' compliance and acceptance, there is still a need for implantable subcutaneous drug delivery to administer drugs over an extended period of time for therapies such as insulin injection and cancer therapy. Long-term administration reduces the need for frequent needle injections and thus dramatically improves long-term patient comfort. The first report on a multiwell silicon-based drug-release device in 1999 [40] was followed by another diffusion-based system, a leuprolide acetate implant, which was evaluated over a period of 12 months by Alza Corporation [41]. Although small in number, there has been a steady number of reports on subcutaneous drug delivery systems (Figure 7a). For details on the individual components of implantable systems such as micropumps and reservoir designs, readers are referred to [39].

Conclusions

This review provides a comprehensive outlook of the current challenges in novel drug delivery systems that are enabled by microtechnology and presents a summary of recent advances in drug delivery systems that have attempted to overcome these challenges. Since each organ imposes different anatomical and physiological challenges, these challenges and recent advancements have been discussed in terms of

target areas. Through miniaturization, integration of multiple functions, and electromechanical actuation, MEMS technology has emerged as the most promising technology to achieve spatiotemporal- and dosage-controlled drug delivery for a wide range of target areas. Thin microneedles or neural probes have enabled localized drug delivery to various regions of the brain with a high spatial resolution while microneedle arrays have been widely used for intraocular and transdermal drug delivery. Implantable systems that provide on-demand or self-regulated drug delivery are now possible through the use of internal and external stimuli for intraocular, gastrointestinal, and subcutaneous drug delivery. For implantable systems, gaining patients' compliance and comfort through implementation of highly robust systems is the most challenging hurdle. Regardless of the areas targeted, there are common issues associated with the implant devices, such as total volume of drug loaded in a reservoir, frequency of reimplantation, passive or active activation and power transfer. With further technological innovations in each of the drug delivery systems and matching the appropriate techniques with a wide spectrum of novel drug candidates, the prospect for novel drug delivery systems enabled by MEMS or other forms of microtechnology is apparently high for clinical translation.

Note

This article and images are drawn from "MEMS devices for drug delivery" *in Advanced Drug Delivery Review* 2018; Vol.128: pp. 132-147.

References

[1] Hunter AC, Moghimi SM. *Polymer Chemistry* 2017; 8: 41-51.

[2] Mishra B, Patel BB, Tiwari S. *Nanomedicine: Nanotechnology, Biology and Medicine* 2010: 6: 9-24.

[3] Shi J, Votruba AR, Farokhzad OC, Langer R. *Nano Letters* 2010; 10: 3223-3230.

[4] Fernandes R, Gracias DH. *Adv. Drug Delivery Reviews* 2012; 64: 1579-1589.

[5] Shi J, Votruba AR, Farokhzad OC, Langer R. *Nano Letters* 2010; 10: 3223.

[6] Kim YC, Park JH, Prausnitz MR. *Adv. Drug Delivery Reviews* 2012; 64: 1547-1568.

[7] Kook G, Lee SW, Lee HC, Cho IJ, Lee HJ. *Micromachines* 2016; 7: 179.

[8] Chen MC, Chan HA, Ling MH, Su LC. *Journal of Materials Chemistry B* 2017.

[9] Lee HJ, Son Y, Kim J, Lee CJ, Yoon ES, Cho IJ. *Lab on a Chip* 2015; 15: 1590-1597.

[10] Munoz F, Alici G, Li W. *Adv. Drug Delivery Reviews* 2014; 71: 77-85.

[11] Aryal M, Arvanitis CD, Alexander PM, McDannold N. *Adv. Drug Delivery Reviews* 2014; 72: 94-109.

[12] Nisar A, Afzulpurkar N, Mahaisavariya B, Tuantranont A. *Sensors and Actuators B: Chemical* 2008; 130: 917-942.

[13] Yasin MN, Svirskis D, Seyfoddin A, Rupenthal ID. *Journal of Controlled Release* 2014; 196: 208-221.

[14] Li H, Yu Y, Faraji Dana S, Li B, Lee CY, Kang L. *Journal of Drug Targeting* 2013; 21: 611-629.

[15] Pardridge WM. *Journal of Cerebral Blood Flow & Metabolism* 2012; 32: 1959-1972.

[16] Mitragotri S. *Nature Reviews Drug Discovery* 2005; 4: 255-260.

[17] Fang F, Zou D, Wang W, Yin Y, Yin T, Hao S, Wang B, Wang G, Wang Y. *Materials Science and Engineering: C* 2017.

[18] Illum L. *Journal of Pharmacy and Pharmacology* 2004; 56: 3-17.

[19] Pardridge WM. *NeuroRx* 2005; 2: 3-14.

[20] Yang FY, Lin YS, Kang KH, Chao TK. *Journal of Controlled Release* 2011; 150: 111-116.

[21] Negishi Y, Yamane M, Kurihara N, Endo-Takahashi Y, Sashida S, Takagi N, Suzuki R, Maruyama K. *Pharmaceutics* 2015; 7: 344-362.

[22] Wang S, Kugelman T, Buch A, Herman M, Han Y, Karakatsani ME, Hussaini SA, Duff K, Konofagou EE. *Scientific Reports* 2017; 7.

[23] Airan RD, Meyer RA, Ellens NP, Rhodes KR, Farahani K, Pomper MG, Kadam SD, Green JJ. *Nano Letters* 2017;17: 652-659.

[24] Airan RD, Foss CA, Ellens NP, Wang Y, Mease RC, Farahani K, Pomper MG. *Molecular Imaging and Biology* 2017; 19: 24-30.

[25] Jin Z, Choi Y, Ko SY, Park JO, Park S. *Biotechnology and Applied Biochemistry* 2016.

[26] Chau Y, Suen WLL, Tse HY, Wong HS. *European Journal of Pharmaceutical Sciences* 2017; 100: 273-279.

[27] Ballantine H Jr, Bell E, Manlapaz J. *Journal of Neurosurgery* 1960; 17: 858-876.

[28] Yasukawa T, Ogura Y, Sakurai E, Tabata Y, Kimura H. *Adv. Drug Delivery Reviews* 2005; 57: 2033-2046.

[29] Patel A, Cholkar K, Agrahari V, Mitra AK. *World Journal Of Pharmacology* 2013; 2: 47.

[30] Craig CR, Stitzel RE. *Lippincott Williams & Wilkins* 2004.

[31] Mc Caffrey C, Chevalerias O, O'Mathuna C, Twomey K. *IEEE Pervasive Computing* 2008; 7.

[32] Stevens HN, Wilson CG, Welling PG, Bakhshaee M, Binns JS, Perkins AC, Frier M, Blackshaw EP, Frame MW, Nichols DJ. *International Journal of Pharmaceutics* 2002; 236: 27-34.

[33] Hebden JM, Gilchrist PJ, Perkins AC, Wilson CG, Spiller RC. *Pharmaceutical Research* 1999; 16: 1254-1259.

[34] Shawgo RS, Grayson ACR, Li Y, Cima MJ. *Current Opinion in Solid State and Materials Science* 2002; 6: 329-334.

[35] Seong KY, Seo MS, Hwang DY, O'Cearbhaill ED, Sreenan S, Karp JM, Yang SY. *Journal of Controlled Release* 2017.

[37] Alexander A, Dwivedi S, Giri TK, Saraf S, Saraf S, Tripathi DK. *Journal of Controlled Release* 2012; 164: 26-40.

[38] Yu J, Zhang Y, Kahkoska AR, Gu Z. *Current Opinion in Biotechnology* 2017; 48: 28-32.

[39] Stevenson CL, Santini JT, Langer R. *Adv. Drug Delivery Reviews* 2012; 64: 1590-1602.

[40] Santini JT, Cima MJ, Langer R. *Nature* 1999; 397: 335-338.

[41] Wright JC, Leonard ST, Stevenson CL, Beck JC, Chen G, Jao RM, Johnson PA, Leonard J, Skowronski RJ. *Journal of Controlled Release* 2001; 75: 1-10.

Feature Articles

Glycyrrhiza uralensis and Semilicoisoflavone B Reduces Aβ Secretion by Inhibiting BACE1 Expression via Increasing PPARγ and Inhibiting STAT3 Phosphorylation

Hyun Ok YANG
Principal Researcher
Natural Products Research Center
KIST Gangneung Institute of Natural Products

hoyang@kist.re.kr

Introduction

Alzheimer's disease (AD) is the most common cause of dementia. While the cause of AD is not yet fully understood, its effect on the brain is clear. In AD, the information transfer that occurs at synapses begins to fail, the number of synapses declines, and neurons eventually die. The accumulation of amyloid beta (Aβ) is believed to interfere with neuron-to-neuron communication at synapses and contribute to cell death [1]. Aβ is produced from amyloid precursor protein (APP). Full-length APP is a type I transmembrane protein. Mature APP (mAPP) traffic between the plasma membrane and endosomal compartments, in which it is sequentially cleaved by groups of enzymes termed α-, β-, and γ-secretase [2]. In the nonamyloidogenic pathway, APP is cleaved by α-secretase, which is mainly enriched in the plasma membrane, producing secreted amyloid precursor protein-α (sAPPα) and APPα C-terminal fragment (C83). Alternatively, in the amyloidogenic pathways, APP is cleaved by β-secretase-1 (BACE1), which is mainly localized in endosomes, producing secreted amyloid precursor protein-β (sAPPβ) and APPβ C-terminal fragment (C99). C83 and C99 can be further cleaved by γ-secretase to produce P3 or Aβ [3, 4]. One pharmaceutical strategy to reduce the generation of Aβ is to inhibit either β- or γ-secretase activity. However, therapeutically inhibiting γ-secretase is considered to have a potentially severe side effects because of its effect on other substrates. Therefore, inhibiting BACE1 is likely a better target for AD therapeutic drug strategies aimed at preventing the production of Aβ.[5, 6]

Peroxisome proliferator activated receptor γ (PPARγ) is a transcription factor that is involved in the regulation of glucose and lipids metabolism, cellular differentiation, and control of the transcription of a wide range of inflammatory genes [7, 8, 9]. Recently, studies have shown that PPARγ suppresses BACE1 and inhibits Aβ production [10, 11]. In addition, signal transducer and activator of transcription 3 (STAT3) is known to regulate numerous genes, and to significantly affect Aβ generation by controlling BACE1 expression [12, 13].

There is currently no drug treatment that provides a cure for AD. Recently, natural herbals and their phytochemicals showed an advantage in slowing down AD development [14]. *Glycyrrhiza uralensis*, also known as Chinese licorice, is a flowering plant that belongs to the family Leguminosae. It has been widely used in food and confectionery products. Licorice leaves have become a popular herbal tea. Licorice root, also known as sweet root, is used primarily as a sweetener in candies and beverages but is also a popular herbal medicines due to its exceptional pharmacological properties, as recognized by traditional Chinese medicine [15, 16]. It is traditionally used as an antidote, demulcent, expectorant, antioxidant, and remedy for inflammation [15, 17]. The root of *G. uralensis* has also been associated with beneficial effects on the brain, acts as an antidepressant [18], memory enhancing agent [19], and provides protection against ischemic brain damage [20]. There has also been considerable research on the role of specific flavonoid constituents isolated from *G. uralensis* Such as liquirtigenin, isoliquiritigenin, and glabridin, related to antidementia, anti-ischemic [21, 22, 23], and antioxidant effects [24]. In AD, *G. uralensis* extract (GUE) has been shown to improve cognitive deficits in AD mode [19]. However, the underlying mechanism and usefulness of specific components behind this effect have not yet been investigated to date. Because Aβ is one of the major pathological hallmark in AD, the aim of the present study was to investigate whether GUE and its component, semilicoisoflavone B (SB) inhibit Aβ secretion and to determine the mechanism involved in this effect.

Materials and Methods

Chemicals and Reagents

α-Amanitin (A2263-1MG), 4′,6-diamidino-2-phenylindole (DAPI) (D9542-10MG), S3I-201 (SML0330-5MG), pioglitazone (Pig) (CDS021593-50MG), GW9662 (M6191-5MG), and rabbit anti-APP antibodies (A8717) for the C-terminal of APP were obtained from Sigma-Aldrich (St. Louis, MO, USA). Fetal bovine serum (FBS) was obtained from ATCC (Manassas, VA, USA). Dulbecco's Modified Eagle's medium(DMEM), Penicillin/streptomycin, G418, and 0.25% trypsin-EDTA were obtained from GIBCO–BRL (Grand Island, NY, USA). Goat anti-rabbit secondary antibody, Alexa Fluor 488 (A-11008), and Zeocin were obtained from Invitrogen (Eugene, OR, USA). Rabbit anti-p-STAT3 (9145), anti-STAT3 (12640), anti-PPARγ (2443), anti-Glyceraldehyde-3-phosphate dehydrogenase (GAPDH) (2118), anti-lamin B1 (12586), anti-rabbit horseradish peroxidase linked IgG antibodies (7074) and cell lysis buffer (9803) were purchased from Cell Signaling Technology, Inc. (Boston, MA, USA). Anti-BACE1 (ab108394) for western blot, anti-BACE1 (ab2077) for immunofluorescence assay, and anti-APP antibody (ab126732) for mAPP, and immature APP (imAPP) were purchased from Abcam. A β-secretase activity fluorometric assay kit was obtained from Biovision (K360-100) (Milpitas, CA, USA). PPARγ-specific siRNA (sc-29455) and control siRNA (sc-37007) were purchased from Santa Cruz (CA, USA). All other chemicals were of analytical grade.

Plant Material

Commercially available licorice (root of *G. uralensis*) imported from Vietnam was purchased in September 2011 from the Kyungdong market in Seoul, Korea. The voucher specimen (KR0925) was authenticated by Prof. Kiwhan Bae and deposited at the herbarium of the Korea Research Institute of Chemical Technology (KRICT), Korea [25].

Extraction and Isolation

The dried roots of *G. uralensis* (2 kg) were extracted twice in methanol at room temperature for 1 week. The obtained residue (430 g) was then suspended in distilled water and then partitioned using ethyl acetate (EtOAc) and *n*-butanol (BuOH), which yielded a 178 g EtOAc soluble fraction and 184 g BuOH soluble fraction. The EtOAc soluble fraction was subjected to silica column chromatography and eluted with CH_2Cl2-MeOH to yield five fractions (F1, F2, F3, F4, and F5). F2 was isolated using silica column chromatography to produce five fractions (F21 ~ F25). F23 was subsequently purified using a silica column and an RP-18 column chromatography to obtain Semilicoisoflavone (SB) [25].

Cell Culture and Viability

HeLa cells that were stably transfected with the Swedish mutant form of APP (APPsw) were grown in DMEM supplemented with 10% heat-inactivated FBS, 1% penicillin/streptomycin, 260 μg mL^{-1} Zeocin and 400 μg mL^{-1} G418 at 37

°C in a humidified atmosphere of 5% CO_2 and 95% air.

Protein Extraction and Western Blot Analysis

Cells were collected after they were treated with different chemicals for the indicated times. The cells were harvested in PBS (pH 7.2). The pellets were extracted using lysis buffer supplemented with protease inhibitor cocktail according to the manufacturer's instructions. Then, the lysates were centrifuged at 13 000 rpm for 20 min at 4 °C. The nuclear proteins in the cells were isolated using a nuclear extraction kit (NE-PER 78835, Thermo) according to the supplier's instructions. The protein content of the supernatant was used in the subsequent experiments. The protein concentration was determined by the Bradford assay (Bio-Rad Laboratories, Hercules, CA, USA). Protein from each sample was separated by SDS-PAGE and then transferred to polyvinylidene fluoride membranes. The membranes were blocked in 5% nonfat milk for 1 h at room temperature and then incubated with primary antibodies overnight at 4 °C. After the membranes were washed three times, they were incubated with horseradish peroxidase-conjugate anti-rabbit IgG antibodies for 1 hour at room temperature and then washed three times. The bound antibodies were visualized using ECL Advance western blotting detection reagents (34095). All the protein levels were normalized to GAPDH, and all the nuclear protein levels were normalized to lamin B1. Imaging and densitometry analyses were performed using an LAS-4000 Luminescent Image Analyzer (Fujifilm, Tokyo, Japan).

Aβ, sAPPα, and sAPPβ Peptide Assay

The cells were cultured with chemicals or dimethyl sulfoxide (DMSO) in DMEM for 8 h. The medium was harvested and then analyzed. For Aβ secretion detection, $Aβ_{42}$ (KHB3442) and $Aβ_{40}$ (KHB3482) kits (Invitrogen, Carlsbad, CA, USA) were used, and we performed the experiments according to the supplier's instructions. For sAPP detection, sAPPα (27734), wild-type sAPPβ (sAPPβ-wt) (27732), and Swedish mutant sAPPβ (sAPPβ-sw) (27733) ELISA kits (IBL, Fujioka, Japan) were used in this study, and we performed the experiments according to the ELISA supplier's instructions.

RNA Isolation and Reverse Transcription-Polymerase Chain Reactions (RT-PCR)

Cells (6×10^5 cells $well^{-1}$) were seeded in six-well plates and incubated for 24 h. The samples were then treated for 8 h. Total RNA was isolated using TRIzol reagent (Invitrogen). To synthesize cDNA, reverse transcription reactions were performed using a Superscript-III kit (Invitrogen, A10752030) with 5 μg of total RNA and oligo dT according to the manufacturer's instructions. The synthesized cDNA was then used for amplification of target genes using the specific primer set shown in Table 1. Semiquantitative PR-PCR was performed using NobleZyme Tap (Noble Bio) with 30 cycles; each cycle consisted of denaturation, annealing, and extension steps. The PCR products were run on 1.5% agarose gels in Tris borate/EDTA buffer. The gels were then stained with ethidium bromide. The intensities of the amplified bands were compared after visualization on a UV transilluminator. The mRNA bands were quantified using densitometric analysis in Image J software (NIH Image public domain, USA). All the mRNA levels were normalized to GAPDH mRNA.

Table 1 Primer pairs for RT-PCR

Gene	Sequence
BACE1	F: 5′-CATTGGAGGTATCGACCACTCGCT-3′
	R: 5′-CCACAGTCTTCCATGTCCAAGGTG-3′
GAPDH	F: 5′-ACCACAGTCCATGCCATCAC-3′
	R: 5′-TCCACCACCCTGTTGCTGTA-3′

Immunofluorescence Assay

To detect the expression of BACE1 (ab2077), P-STAT3, and PPARγ, cells were seeded on sterile coverslips placed in 24-well culture plates. After the cells were treated with the indicated drugs for 8 h, they were washed with PBS, fixed with 3.8% paraformaldehyde for 15 min, permeabilized with 0.2% Triton X-100 for 30 min, blocked in 5% BSA in PBS for 1 h, incubated with primary antibodies overnight, and then incubated with secondary antibodies labeled with Alexa Fluor 488 (Invitrogen) for 1 h at room temperature in darkness. The cells were then stained with DAPI at 37 °C for 30 min in darkness. The coverslips were prepared for analysis by adding one drop fluorescent Mounting Medium (Dako, S3023), and the coverslips were then sealed to the slides. Images were obtained using a Leica TCS SP5 confocal microscope (Leica, Mannheim, Germany) with exicitation/emission wavelengths of 493 nm 519 nm^{-1} for Alexa Fluor 488 and exicitation/emission wavelengths of 358 nm 461 nm^{-1} for DAPI. The images were analyzed using Image-Pro Plus 6.0 (Bethesda, MD, USA).

β-Secretase Activity Assay

β-Secretase activity was analyzed using a commercially available β-secretase activity kit (Biovision, Cat. K360-100). Protein was extracted from cells using extraction buffer as manufacturer's protocol. GUE and SB were added to the lysate (100 μg protein) to make 50 μL of sample buffer, which was then added to each well in a 96-well plate. Afterward, 50 μL of 2× reaction buffer was added, and preincubated 20 min at 37 °C. This was followed by the addition of 2 μL of substrate and then incubation in the dark at 37 °C for 1 h. Fluorescence was read at excitation/emission wavelengths of 345/500 nm.

siRNA Transient Transfection

Cells were transfected with PPARγ-siRNA using the transfection reagent Lipofectamine RNAiMAX (13778) for 12 h according to the manufacturer's instructions. The transfected cells were treated with GUE or SB for 8 h and then harvested for subsequent experiments.

Transfection and Luciferase Assay

Cells were seeded in a 24-well plate and then transfected with 0.5 μg of BACE1 promotor constructs (kindly provided by Inhee Mook-Jung at Seoul National University, College of Medicine, Seoul, Korea) using Lipofectamine 3000 reagent. pRL-SV40 (E2231) plasmid (5 ng) was cotransfected to normalize the transfection efficiencies according to the manufacturer's protocol. Cells were transfected for 24 h and then treated sample for 8 h. To assay the BACE1 promotor activity, cells were lysed with 1× passive lysis buffer, and luciferase assays were performed according to the Dual Luciferase Assay System protocol (Promega, Madison, WI, USA) using Luminometer (Promega). Luciferase activity was normalized to the Renilla luciferase activity from the Prl-SV40 plasmid.

Statistical Analysis

All data were analyzed in Prism 7.0 software (GraphPad Software, Inc., San Diego, CA, USA) and are expressed as the mean ± SEM. The statistical analyses were performed using one-way analysis of variance (ANOVA) followed by the Tukey multiple comparison test. Statistical significance was set at $p < 0.05$.

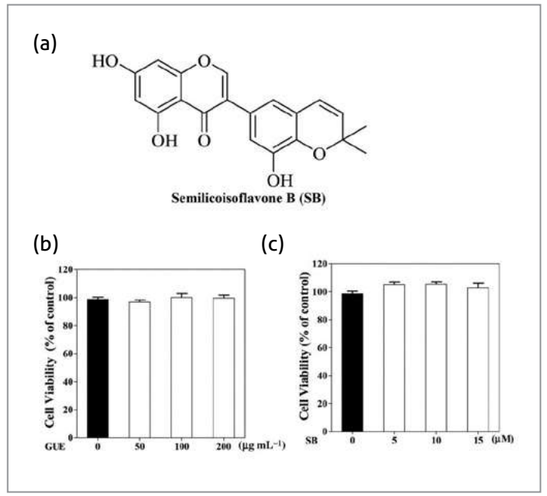

Figure 1 Effect of GUE and SB on cell viability. (a) Chemical structure of SB. Cells were treated with GUE (50, 100, and 200 μg mL^{-1}) and SB (5, 10, and 15 μM) for 8 h. The effect of GUE (b) and SB (c) on cell viability were determined using MTT assays (n = 4).

Results

Effect of GUE and SB on Cell Viability

In the previous study, we scanned 11 compounds extracted from GUE, SB showed the same effect as GUE on Aβ secretion (data not shown). The structure of SB is shown in Figure 1a. To test the effect of GUE and SB on cell viability, cells were treated with GUE (50, 100, and 200 μg mL^{-1}) or SB (5, 10, and 15 μM) for 8 h. Neither GUE nor SB showed cytotoxicity at the applied concentration (Figures 1b and 1c). Therefore, we used these concentrations in this study.

Effect of GUE and SB on Aβ Secretion

To test the effect of GUE and SB on Aβ production, cells were treated with GUE (50, 100, and 200 μg mL^{-1}) or SB (5, 10, and 15 μM) for 8 h. GUE decreased $Aβ_{42}$ levels to 87.2 ± 4.8%, 54.3 ± 6.3% and 29.5 ± 2.8%, respectively, and decreased $Aβ_{40}$ levels to 74.3 ± 3.3%, 43.3 ± 3.5% and 13.5 ± 1.2%, respectively (Figure 2a). SB decreased $Aβ_{42}$ levels to 97.3 ± 7.2%, 78.4 ± 6.2% and 66.8 ± 2.6%, respectively, and

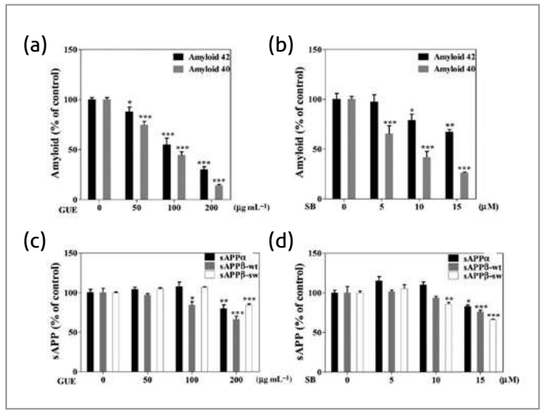

Figure 2 Effect of GUE and SB on Aβ and sAPP secretion. Cells were treated with GUE (50, 100 and 200 μg mL^{-1}) and SB (5, 10 and 15 μM) for 8 h. The effect of GUE (a) and SB (b) on $Aβ_{42}$ and $Aβ_{40}$ secretion; the effect of GUE (c) and SB (d) on sAPPβ and sAPPβ secretion were measured.

decreased $Aβ_{40}$ levels to 65.1 ± 8.5%, 41.6 ± 6.2% and 25.6 ± 1.1%, respectively (Figure 2b). Next, we examined the effect of GUE on sAPPα and sAPPβ secretion. Applying 100 and 200 μg mL^{-1} GUE significantly decreased sAPPβ-wt to 83.9 ± 4.1% and 65.6 ± 3.7%, respectively, and 200 μg mL−1 GUE significantly decreased sAPPβ-sw and sAPPα to 84.3 ± 1.7% and 79.3 ± 5.0%, respectively (Figure 2c). The effect of SB on sAPPα and sAPPβ were also examined. Applying 15 μM SB significantly decreased sAPPβ-wt secretion to 75.8 ± 2.3%, 10 and 15 μM SB decreased sAPPβ-sw secretion to 85.8 ± 2.3% and 66.3 ± 0.5%, respectively. In addition, 15 μM SB also significantly decreased sAPPα production to 82.3 ± 2.0% (Figure 2d). This result shows that GUE and SB decrease both Aβ and sAPP secretion.

Effect of GUE and SB on APP Processing

To determine how GUE and SB affect the APP process, we evaluated the effect of GUE and SB on the expression of APP C-terminal fragments. Applying GUE and SB significantly decreased the expression of C99 and C83 (Figures 3a and 3b), and significantly decreased the sAPPβ expression in cells (Figure 3C and D). Aβ is produced from APP, so we next investigated the effect of GUE and SB on APP expression. GUE and SB significantly increased the levels of both mAPP and imAPP (Figures 3e and 3f). Both GUE and SB inhibited Aβ and sAPPβ secretion but did not reduce the expression of total APP.

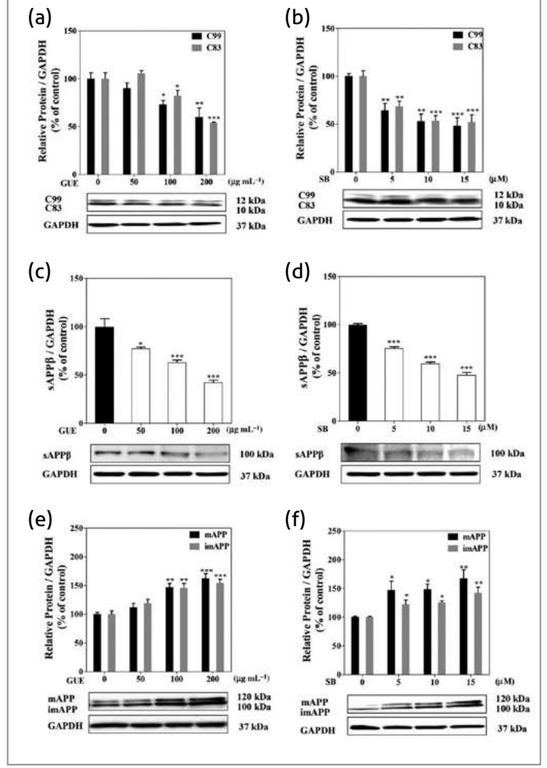

Figure 3 Effect of GUE and SB on APP expression. Cells were treated with GUE (50, 100, and 200 μg mL^{-1}) and SB (5, 10, and 15 μM) for 8 h. The effect of GUE (a) and SB (b) on C83 and C89 expression; The effect of GUE (c) and SB (d) on sAPPβ expression; the effect of GUE (e) and SB (f) on mature APP (mAPP) and immature APP (imAPP) expression were evaluated using western blot analysis (n = 6). $^{*}p < 0.05$, $^{**}p < 0.01$, $^{***}p < 0.001$ compared with the control group.

Effect of GUE and SB on BACE1 Expression and Activity

We therefore tried to determine whether GUE and SB influence BACE1 expression. GUE significantly decreased the expression of BACE1 (Figures 4a and 4b). We next investigated the effect of GUE on BACE1 activity. GUE at 100 and 200 μg mL^{-1} significantly inhibited BACE1 activity to 86.0 and 84.4%, respectively (Figure 4e). SB also significantly decreased the expression of BACE1 (Figures 4c and 4d). Moreover, SB, when applied at 5, 10, and 15 μM significantly inhibited BACE1 activity to 89.3 ± 0.01, 84.7, and 78.6%, respectively (Figure 4f). This result indicates that GUE and SB reduce Aβ secretion by inhibiting BACE1 expression and activity.

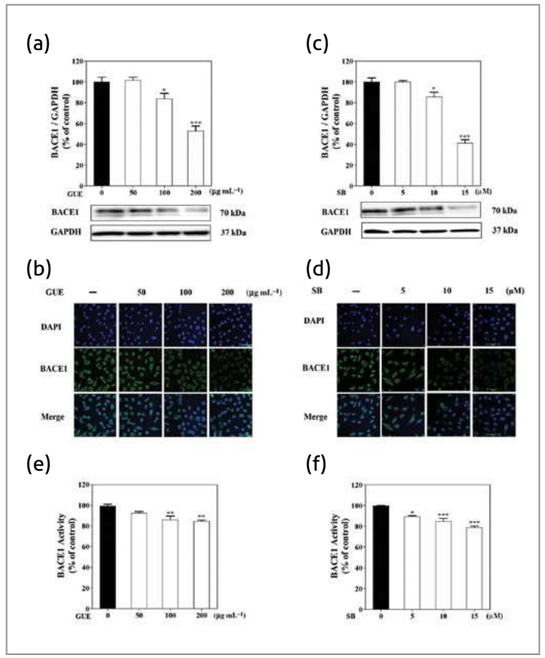

Figure 4 Effect of GUE and SB on BACE1 expression and activity. Cells were treated with GUE (50, 100, and 200 μg mL^{-1}) and SB (5, 10, and 15 μM) for 8 h. The effect of GUE on BACE1 expression were evaluated using western blot analysis (a) and immunofluorescence staining assay (bar = 50 μm) (b). The effect of SB on BACE1 expression were evaluated using western blot analysis (c) and immunofluorescence staining assay (bar = 50 μm) (d). The β-secretase enzyme was extracted from cells. The effect of GUE (e) and SB (f) on BACE1 activity was evaluated using a β-secretase activity assay kit (n = 6). $^{*}p < 0.05$, $^{**}p < 0.01$, $^{***}p < 0.001$ compared with the control group.

Effect of GUE and SB on BACE1 mRNA Expression

To investigate the mechanisms underlying the effect of GUE and SB on BACE1 expression, RT-PCR was performed to determine the mRNA expression of BACE1. Both GUE and SB significantly decreased the mRNA expression level of BACE1 (Figures 5a and 5b). To determine whether GUE and SB decreased BACE1 mRNA expression by inhibiting transcription, we used α-amanitin, a transcription inhibitor. We found that α-amanitin (40 μM) significantly decreased the mRNA expression level of BACE1 similar to the effect of GUE and SB. Moreover, cotreatment with α-amanitin and GUE or SB did not further decrease BACE1 mRNA expression (Figures 5c and 5d). This result indicate that GUE and SB decrease the mRNA expression of BACE1 by inhibiting its transcription.

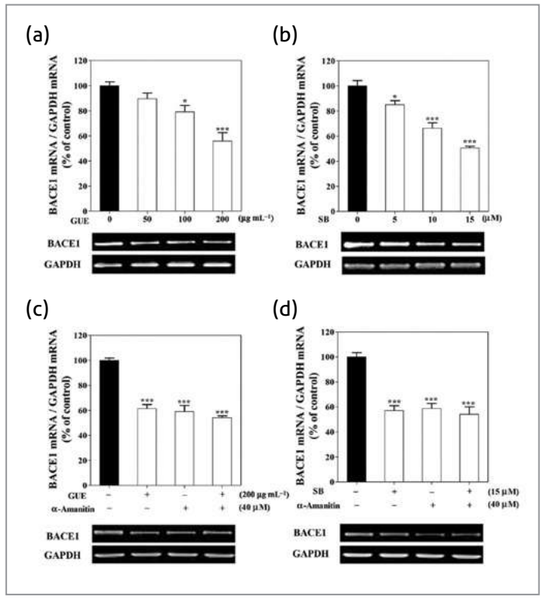

Figure 5 Effect of GUE and SB on BACE1 mRNA expression. Cells were treated with GUE (50, 100, and 200 μg mL^{-1}) and SB (5, 10 and 15 μM) for 8 h. The effect of GUE (a) and SB (b) on BACE1 mRNA expression was then evaluated using RT-PCR. Cells were pretreated with 40 μM α-amanitin for 30 min, then treated with 200 μg mL^{-1} GUE (c) or 15 μM SB (d) and finally incubated for 8 h. The mRNA expression level of BACE1 was then evaluated using RT-PCR (n = 5). $^{*}p < 0.05$, $^{***}p < 0.001$ compared with the control group.

Effect of GUE and SB on BACE1 Transcription Process

BACE1 expression is tightly regulated at the transcriptional level. The sequence upstream of the BACE1 gene contains many putative transcription factor binding sites. STAT3 was previously identified as a potent inducer of BACE1 transcription [26]. Phosphorylated STAT3 dimerizes and translocates into the nucleus27 where it positively regulates the transcription of the BACE1 gene. However, unphosphorylated STAT3 proteins also exist inside the nucleus and have the ability to dimerize and bind other DNA [28]. Therefore, we investigated the effect of GUE and SB on STAT3

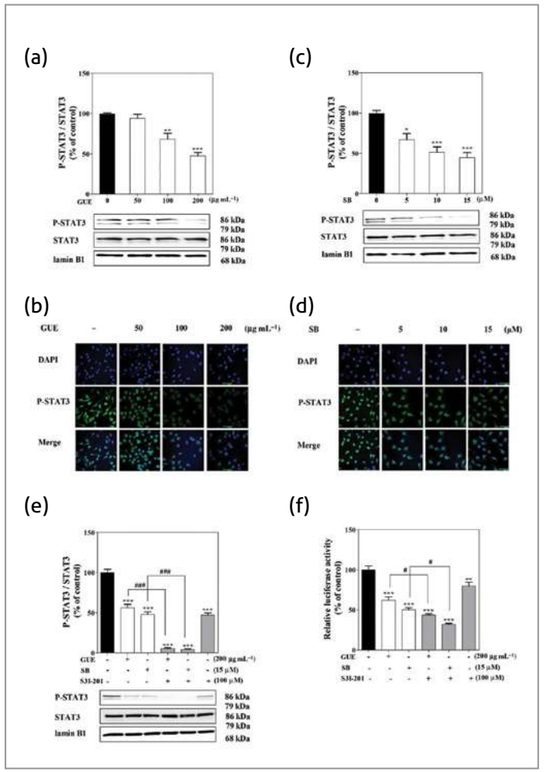

Figure 6 Effect of GUE and SB on STAT3 phosphorylation. Cells were treated with GUE (50, 100, and 200 μg mL^{-1}) and SB (5, 10, and 15 μM) for 8 h, and nuclear proteins were then extracted. The effect of GUE on P-STAT3 expression was evaluated using western blot analysis (a) and immunofluorescence staining assay (bar = 50 μm) (b). The effect of SB on P-STAT3 expression was evaluated using western blot analysis (c) and immunofluorescence staining assay (bar = 50 μm) (d). Cells were pretreated with 100 μM SI-201 for 30 min and then treated with GUE or SB and incubated for 8 h. The effects of GUE and SB on P-STAT3, STAT3 and lamin B1 expression were then evaluated using western blot analysis (e). The effects of GUE and SB on BACE1 promotor activity were then evaluated using a dual luciferase assay (f) (n = 5). $^{*}p < 0.05$, $^{**}p < 0.01$, $^{***}p < 0.001$ compared with the control group, $^{\#}p < 0.05$, $^{\#\#\#}p < 0.001$.

phosphorylation (P-STAT3) in nuclear extracts. GUE and SB significantly decreased the level of P-STAT3 (Figures 6a–d). S3I-201, a STAT3 inhibitor, prevents STAT3 phosphorylation [29]. As shown in Figure 6e, S3I-201 (100 μM) significantly inhibited STAT3 phosphorylation in a manner similar to GUE and SB. Moreover, cotreatment with S3I-201 and GUE or SB inhibited STAT3 phosphorylation much more than treatment with S3I-201 alone. This result indicates that GUE and SB inhibit STAT3 phosphorylation through a different mechanism

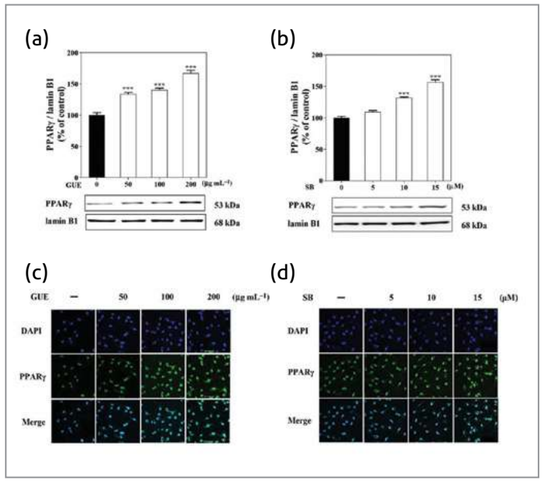

Figure 7 Effect of GUE and SB on PPARγ expression. Cells were treated with GUE (50, 100, and 200 μg mL^{-1}) and SB (5, 10, and 15 μM) for 8 h, and nuclear proteins were then extracted. The effect of GUE on PPARγ expression was evaluated using western blot analysis (n = 4) (a) and immunofluorescence staining assay (bar = 50 μm) (b). The effect of SB on PPARγ expression was evaluated using western blot analysis (n = 6) (c) and immunofluorescence staining assay (bar = 50 μm) (d). $^{***}p < 0.001$ compared with the control group.

with S3I-201. We also evaluated the effect of GUE and SB on BACE1 promotor activity. S3I-201, GUE, and SB inhibited BACE1 promotor activity, and cotreatment of S3I-201 with GUE or SB decreased BACE1 promotor activity much more than treatment with S3I-201 alone (Figure 6f).

Another transcription factor, PPARγ, is a ligand-dependent transcription factors. PPARγ agonists downregulate the generation of Aβ by regulating BACE1 [30]. We therefore investigated the effect of GUE and SB on PPARγ expression in nuclear extracts. GUE and SB significantly increased the expression of PPARγ (Figure 7). To determine whether GUE and SB regulate BACE1 expression mainly by regulating PPARγ, we examined BACE1 expression and $A\beta_{42}$ secretion in cells transfected with PPARγ siRNA. In cells cotreated with control siRNA and either GUE or SB, PPARγ expression was increased, while BACE1 expression was decreased. However, these effects were diminished in the cells transfected with PPARγ siRNA (Figure 8a). Consistent with these results, we also found that GUE and SB decreased $A\beta_{42}$ secretion in cells treated with control siRNA, whereas these effects were diminished in the cells transfected with PPARγ siRNA (Figure 8b). We next used the PPARγ antagonist GW966231 to confirm the role of

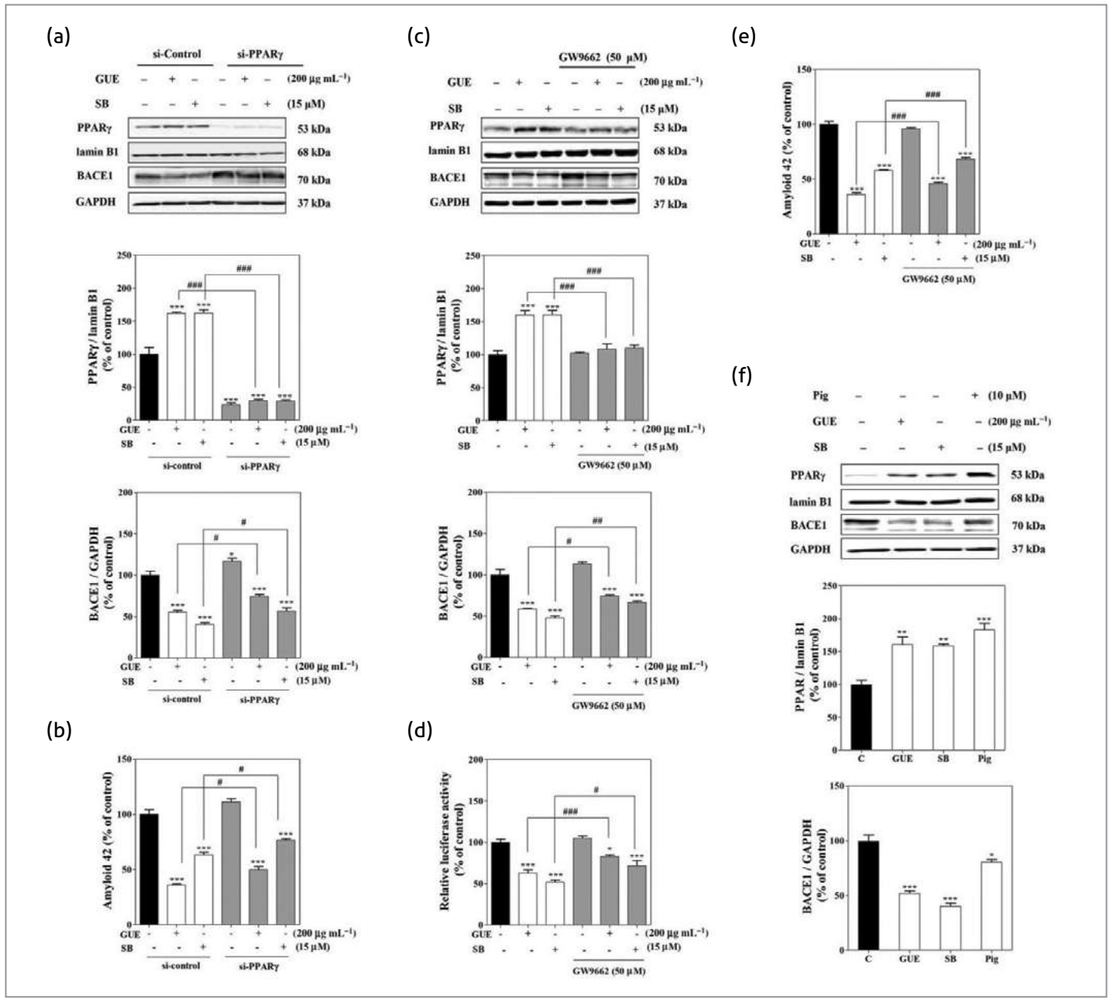

Figure 8 The effect of GUE and SB on Aβ secretion and BACE1 expression is PPARγ-dependent. Cells were treated with control siRNA or PPARγ siRNA for 12 h and then treated with GUE at 200 μg mL^{-1} or SB at 15 μM for 8 h. The expression levels of PPARγ, lamin B1, BACE1, and GAPDH were evaluated using western blot analysis (a). The level of $A\beta_{42}$ was measured using ELISA kit (b). Cells were pretreated with GW9662 at 50 μM for 30 min and then with GUE at 200 μg mL−1 or SB at 15 μM for 8 h. The expression levels of PPARγ, lamin B1, BACE1, and GAPDH were then evaluated using western blot analysis (c). The BACE1 promotor activity was evaluated using dual luciferase assay (d). The level of $A\beta_{42}$ was measured using ELISA kit (e). Cells were treated with GUE, SB, and Pig and incubated for 8 h. The levels of PPARγ, lamin B1, BACE1, and GAPDH were then evaluated using western blot analysis (f) (n = 4). $^{***}p < 0.001$ compared with the control group, $^{\#}p < 0.05$, $^{\#\#}p < 0.01$, $^{\#\#\#}p < 0.001$.

PPARγ in this process. Cells were treated with 50 μM GW9662 for 30 min prior to incubation with GUE or SB. GUE and SB increased PPARγ expression, and this increase was significantly attenuated when cells were cotreated with GW9662. In addition, cotreatment with GW9662 significantly blocked the effects of GUE and SB on BACE1 promotor activity, BACE1 expression, and $A\beta_{42}$ secretion (Figures 8c–e). These results indicated that GUE and SB may act as PPARγ agonists to control BACE1 expression. We also evaluated the effect of PPARγ agonist, Pig32 on BACE1 expression; Pig (10 μM) significantly

increased PPARγ expression, similar to the effect of GUE and SB, but did not reduce BACE1 expression as much as GUE and SB did (Figure 7e). This result indicates that GUE and SB decrease BACE1 expression mainly through increasing PPARγ expression and inhibiting STAT3 phosphorylation.

Discussion

In this study, we first showed that GUE and SB significantly decreased both $A\beta_{42}$ and $A\beta_{40}$ secretion (Figures 2a and 2b). We then confirmed that GUE and SB significantly decreased sAPP secretion (Figures 2c and 2d), sAPPβ expression, and the expression of the C-terminal fragment of APP. However, GUE and SB did not reduce the expression of mAPP and imAPP, but instead increased the expression of both (Figure 3). This finding may be attributed to the inhibition effect of GUE and SB on the proteolysis of APP. These results indicate that GUE and SB decrease Aβ secretion may mainly due to inhibition of BACE1 rather than activation of α-secretase.

As expected, GUE and SB significantly decreased BACE1 expression (Figure 4). BACE1 expression can be regulated at the level of transcription, translation, and protein degradation. We further investigated the mechanism underlying the involvement of GUE and SB in those processes. We confirmed that the mRNA expression of BACE1 was decreased by GUE and SB and that cotreatment with a transcription inhibitor did not further decrease BACE1 expression (Figure 5). These results indicate that GUE and SB downregulate BACE1 expression mainly by inhibiting BACE1 transcription.

GUE and SB did not decrease the expression of all proteins and they appeared to specifically decrease the expression of BACE1. A transcription factor exerts its effect by binding to a specific DNA sequence. A number of transcription factors have been suggested to control BACE1 transcription. These include specificity protein (SP1), Yin Yang (YY1), hypoxia inducible factor 1α, PPARγ, and STAT3 [7, 33, 34]. We therefore evaluated the effect of GUE and SB on STAT3 phosphorylation. As shown in Figure 6, GUE and SB decreased the level of phosphorylated STAT3. Furthermore, we found that GUE and SB target different molecules with S3I-201 to regulate STAT3 phosphorylation. A further study will investigate how GUE and SB regulate STAT3 phosphorylation. However, we cannot rule out the possibility GUE and SB may regulate the activity of other transcription factors that affect BACE1 promoter activity. The nuclear receptor PPARγ is a ligand-dependent transcription factor, and the activation of PPARγ has been shown to regulate inflammation [35]. Recently, many studies have shown that PPARγ agonists modulate the processing of APP by regulating BACE1, and previous results have suggested that PPARγ may be a repressor of BACE1. Therefore, PPARγ has been recognized as a novel therapeutic target for AD treatment. In this study, we found that GUE and SB significantly increased PPARγ expression (Figure 7). We further confirmed the effect of GUE and SB in PPARγ-siRNA–transfected cells and in cells treated with the PPARγ antagonist GW9662, which abolished the effect of GUE and SB on PPARγ expression. Finally, we verified that the effect of GUE and SB on $A\beta_{42}$ secretion and BACE1 expression is PPARγ-dependent. Additionally, a PPARγ agonist, Pig, also induced PPARγ expression while inhibiting BACE1 expression in this study (Figure 8). Because SB shows effect on both PPARγ and STAT3, we can assume that some key protein targeted by SB may exist in upstream of PPARγ and STAT3. It is well known that some kinases can regulate PPARγ and STAT3 activity, and a further study will be carried out to verify this hypothesis.

BACE1 is an aspartyl-protease, which is a stress-induced protease. Oxidative stress, inflammation, calcium homeostasis disturbance, hypoxia, and ischemia activate BACE1 enzymatic activity [36]. Subtle changes in BACE1 activity significantly affect the pathomechanism of AD [37]. Recently, many studies showed that PPARγ agonists also inhibit BACE1 activity [38, 39]. In this study, GUE and SB also inhibited BACE1 activity (Figure 3), and this effect may have contributed to their effect on PPARγ. However, the underlying mechanism requires further study. Based on these results, we propose that GUE and SB target the PPARγ protein to regulate BACE1 transcription and activity.

To date, there is no effective drug to stop or modify the disease course. Therefore, nonpharmacological interventions may be helpful to improve the quality of AD patient's life [40]. Dietary intervention using natural extracts might be a candidate for an adjuvant therapy of AD. In this study, we first showed that GUE and its active compound SB inhibit Aβ secretion by inhibiting the expression and activity of BACE1. Further, our results indicate that GUE and SB inhibit BACE1 expression by inhibiting the phosphorylation of STAT3 and increasing PPARγ expression, which suggest that GUE and SB may function as PPARγ agonists. Altogether, this study supports the idea that GUE and SB might be functional dietary ingredients for the prevention of AD.

Note

This article and images are drawn from "Glycyrrhiza uralensis and Semilicoisoflavone B reduces Aβ secretion by increasing PPARγ Expression and inhibiting STAT3 phosphorylation to inhibit BACE1 expression" *in Molecular Nutrition & Food Research* 2018: 62; 6

References

[1] M. S. Parihar, G. J. Brewer, *J. Alzheimers Dis*. 2010; 22: 741.
[2] H. Zheng, E. H. Koo, *Mol. Neurodegener*. 2006; 1; 5.
[3] F. M. LaFerla, K. N. Green, S. Oddo, *Nat. Rev. Neurosci*. 2007; 8: 499.
[4] C. Zhang, A. Browne, D. Child, R. E. Tanzi, *J. Biol. Chem*. 2010; 285: 28472.
[5] Y. Li, W. Zhou, Y. Tong, G. He, W. Song, *FASEB J*. 2006; 20: 285.
[6] R. Vassar, *Alzheimers Res. Ther*. 2014; 6: 89.
[7] S. Rossner, M. Sastre, K. Bourne, S. F. Lichtenthaler, P*rog. Neurobiol*. 2006; 79: 95.
[8] L.M. Chen, Z. Y. Lin, Y. G. Zhu, N. Lin, J. Zhang, X. D. Pan, X. C. Chen. *Eur. J. Pharmacol*. 2012; 675: 15.
[9] L. Wang, B. Waltenberger, E. M. Pferschy-Wenzig, M. Blunder, X. Liu, C. Malainer, T. Blazevic, S. Schwaiger, J. M. Rollinger, E. H. Heiss, D. Schuster, B. Kopp, R. Bauer, H. Stuppner, V. M. Dirsch, A. G.Atanasov, *Biochem. Pharmacol*. 2014; 92: 73.
[10] N. Lin, L. M. Chen, X. D. Pan, Y. G. Zhu, J. Zhang, Y. Q. Shi, X. C.Chen, *Mol. Neurobiol*. 2016; 53: 6397.
[11] G. Cao, P. Su, S. Zhang, L. Guo, H. Zhang, Y. Liang, C. Qin, W. Zhang, *Eur. J. Pharmacol*. 2016; 793: 101.
[12] P. Jin, J. A. Kim, D. Y. Choi, Y. J. Lee, H. S. Jung, J. T. Hong, *J. Neuroinflammation*. 2013; 10: 2.
[13] T. Chiba, M. Yamada, J. Sasabe, K. Terashita, M. Shimoda, M. Matsuoka, S. Aiso, *Mol. Psychiatry* 2009; 14: 206.
[14] A. Prasansuklab, T. Tencomnao, *Evid. Based Complement. Altern. Med*. 2013; 2013: 413808.
[15] C. Fiore, M. Eisenhut, E. Ragazzi, G. Zanchin, D. Armanini, J. *Ethnopharmacol*. 2005; 99: 317.
[16] R. A. Isbrucker, G. A. Burdock, *Regul. Toxicol. Pharmacol*. 2006; 46: 167.
[17] A. Olukoga, D. Donaldson, *J. R. Soc. Promot. Health* 2000, *120*, 83.
[18] W. Wang, X. Hu, Z. Zhao, P. Liu, Y. Hu, J. Zhou, D. Zhou, Z. Wang, D.Guo, H. Guo, *Prog. Neuropsychopharmacol. Biol. Psychiatry* 2008; 32:1179.
[19] J. Ahn, M. Um, W. Choi, S. Kim, T. Ha, B*iogerontology* 2006, 7, 239.
[20] I. K. Hwang, S. S. Lim, K. H. Choi, K. Y. Yoo, H. K. Shin, E. J. Kim, J. H.Yoon-Park, T. C. Kang, Y. S. Kim, D. Y. Kwon, D. W. Kim, W. K. Moon, M. H. Won, *Acta. Pharmacol. Sin*. 2006; 27: 959.
[21] C. Zhan, J. Yang, *Pharmacol. Res*. 2006, 53, 303.
[22] Y. M. Cui, M. Z. Ao, W. Li, L. J. Yu, *Planta Med*. 2008, 74, 377.
[23] Y. X. Sun, Y. Tang, A. L. Wu, T. Liu, X. L. Dai, Q. S. Zheng, Z. B. Wang, *J. Asian Nat. Prod. Res*. 2010; 12: 1051.
[24] S. Kumar, A. Sharma, B. Madan, V. Singhal, B. Ghosh, *Pharmacology* 2007; 73: 1602.
[25] J. E. Lee, J. Y. Lee, J. Kim, K. Lee, S. U. Choi, S. Y. Ryu, *Arch. Pharm. Res*. 2015; 38: 1299.
[26] Y. Xiang, S. Meng, J. Wang, S. Li, J. Liu, H. Li, T. Li, W. Song, W. Zhou, *Sci. Rep*. 2014; 4: 6864.
[27] L. Liu, R. Martin, G. Kohler, C. Chan, *Exp. Neurol*. 2013, 248, 482.
[28] J. Sgrignani, S. Olsson, D. Ekonomiuk, D. Genini, R. Krause, C. V. Catapano, A. Cavalli, *Biochemistry* 2015; 54: 5489.
[29] K. Siddiquee, S. Zhang, W. C. Guida, M. A. Blaskovich, B. Greedy, H. R. Lawrence, M. L. R. Yip, R. Jove, M. M. McLaughlin, N. J. Lawrence, S. M. Sebti, J. Turkson, *Proc. Natl. Acad. Sci*. USA 2007; 104: 7391.
[30] M. Sastre, I. Dewachter, G. E. Landreth, T. M. Willson, T. Klockgether, F. van Leuven, M. T. Heneka, *J. Neurosci*. 2003; 23: 9796.
[31] X.Wang, Y. Wang, J. P.Hu, S. Yu, B. K. Li, Y. Cui, L. Ren, L. D. Zhang, *Mol. Neurobiol*. 2017; 54: 2939.
[32] S. Suzuki, L. L. Arnold, K. L. Pennington, S. Kakiuchi-Kiyota, M. Wei, H. Wanibuchi, S. M. Cohen, *Toxicol. Sci*. 2010; 113: 349.
[33] X.-F. Chen, Y.-w. Zhang, H. Xu, G. Bu, *Mol. Brain*. 2013, 6, 44.
[34] E. Tamagno, M. Guglielmotto, D. Monteleone, A. Vercelli, M. Tabaton, *IUBMB Life* 2012; 64: 943.
[35] T. Kim, L. D. Wahyudi, F. J. Gonzalez, J. H. Kim, *Biomol. Ther*. 2017; 25: 504.
[36] L. Chami, F. Checler, *Mol. Neurodegener*. 2012, 7, 52.
[37] N. Takasugi, T. Sasaki, K. Suzuki, S. Osawa, H. Isshiki, Y. Hori, N.Shimada, T. Higo, S. Yokoshima, T. Fukuyama, V. M. Lee, J. Q. Trojanowski, T. Tomita, T. Iwatsubo, *J. Neurosci*. 2011; 31: 6850.
[38] F. Liu, Y. Wang, M. Yan, L. Zhang, T. Pang, H. Liao, *Neurosci. Lett*. 2013; 557: 90.
[39] L. Katsouri, C. Parr, N. Bogdanovic, M. Willem, M. Sastre, *J.Alzheimers Dis*. 2011; 25: 151.
[40] G. A. K. Pivi, N. M. d. A. Vieira, J. B. da Ponte, D. S. C. de Moraes, P.H. F. Bertolucci, *Nutrire* 2017; 42: 1.

Decellularized heart ECM hydrogel using supercritical carbon dioxide for improved angiogenesis

February 2018 / *Acta Biomaterialia* / Vol. 67 / pp. 270-281

Young Mee JUNG
Principal Researcher
Center for Biomaterials
Biomedical Research Institute

winnie97@kist.re.kr

Initial angiogenesis within the first 3 days is critical for healing ischemic diseases such as myocardial infarction. Recently, decellularized extracellular matrix (dECM) has been reported to provide tissue-derived ECM components and can be used as a scaffold for cell delivery for angiogenesis in tissue engineering. Decellularization by various detergents such as sodium dodecyl sulfate (SDS) and triton X-100 can remove the cell nuclei in tissue organs. However, this leads to ECM structure denaturation, decreased presence of various ECM proteins and cytokines, and loss of mechanical properties. To overcome these limitations, in this study, we developed a supercritical carbon dioxide and ethanol co-solvent ($scCO_2$-EtOH) decellularization method, which is a detergent-free system that prevents ECM structure disruption and retains various angiogenic proteins in the heart dECM, Testing was performed on rat heart tissues.

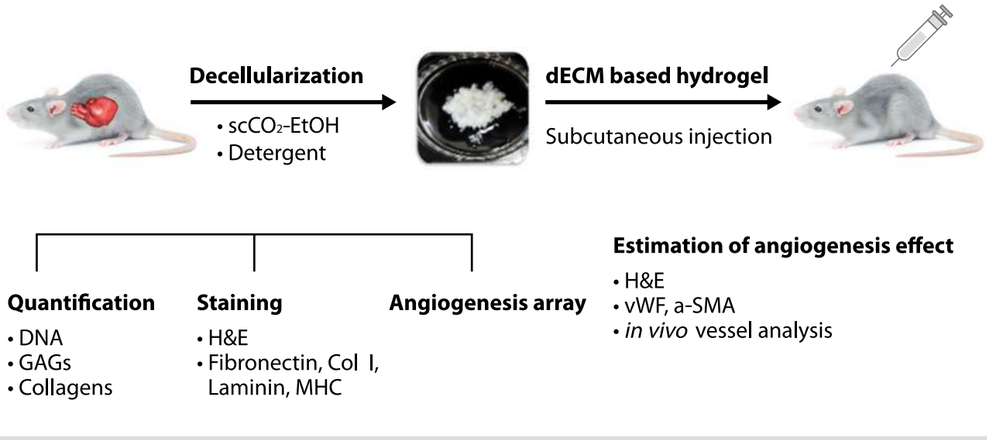

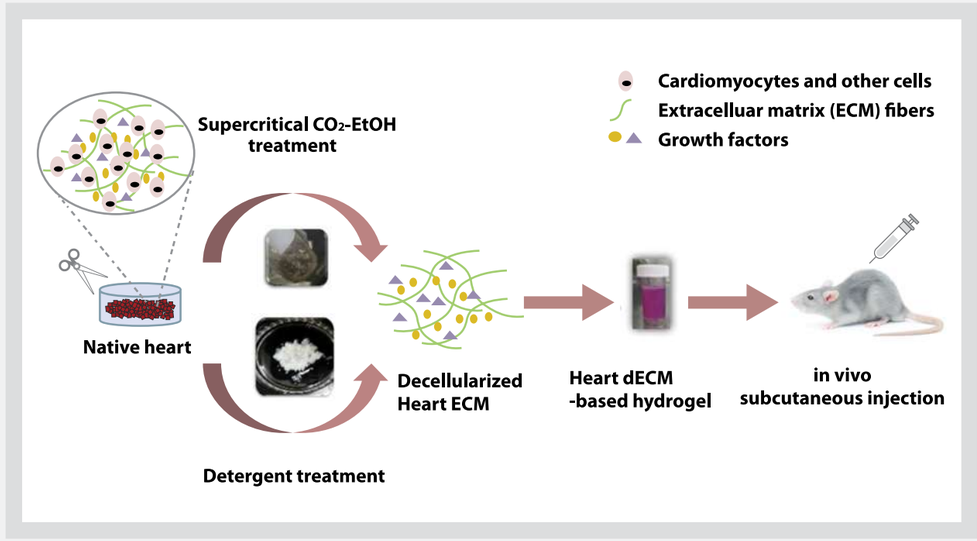

The heart tissue was placed into the $scCO_2$ reactor and decellularized at 37°C and 350 bar. After $scCO_2$-EtOH treatment, the effects were evaluated by DNA, collagen, and glycosaminoglycan (GAG) quantification and hematoxylin and eosin and immunofluorescence staining to determine the absence of nucleic acids and preservation of heart ECM components. Similar to the native group, the $scCO_2$-EtOH group contained more ECM components such as collagen, GAGs, collagen I, laminin, and fibronectin and angiogenic factors including vascular endothelial growth factor, fibroblast growth factor, and platelet-derived growth factor and others in comparison to the detergent group. In addition, to estimate angiogenesis of the dECM hydrogels, the neutralized dECM solution was injected in a rat subcutaneous layer ($n = 6$ in each group: collagen, $scCO_2$-EOH, and detergent group), after which the solution naturally formed gelation in the subcutaneous layer. After 3 days, the gels were harvested and estimated by immunofluorescence staining and the ImageJ program for angiogenesis analysis. Blood vessel formation and density of vWF and α-SMA in the $scCO_2$-EtOH group were significantly greater than that in the collagen group. Here we suggest that heart-derived decellularized extracellular matrix (dECM) with $scCO_2$-EtOH treatment is a highly promising angiogenic material for healing in ischemic disease.

Technical Review

High-Performance and Uniform 1 cm^2 Polymer Solar Cells with D_1-A-D_2-A-Type Random Terpolymers

Hae Jung SON
Principal Researcher
Photo-Elecitronic Hybrids Research Center
National Agenda Research Division

hjson@kist.re.kr

Introduction

Organic photovoltaics (OPVs) have received widespread interest in recent years owing to the possibility of fabricating efficient, light, and flexible devices with low-cost techniques [1-3]. Over the last decade, the performance of polymer solar cells has gradually improved, mainly due to the development of high-performance electron–donor/electron–acceptor (D-A) copolymers with low bandgaps, broad absorption, low-lying highest occupied molecular orbital (HOMO)–lowest unoccupied molecular orbital (LUMO) energy levels, and appropriate charge transport properties [4-8]. Improvements in processing bulk heterojunctions (BHJs) and controlling nanomorphology have also contributed to outstanding enhancements in polymer solar cell efficiencies [9-11]. Power conversion efficiencies (PCEs) exceeding 10% have been achieved for single and multijunction polymer solar cells [12-15]. However, these PCEs have yet to be realized at the module scale in which devices are made with narrow strips in a serial order or with parallel connections. Research efforts to enhance the performance of such minimodules have been performed by IMEC(International Medical Equipment Collaborative) with PCEs of 6.5% (16 cm^2) and Heliatek 7.7% (140 cm^2) [16-17].

Typically, the thickness of the active layers of organic solar cells is limited to ≈100 nm because of the relatively low charge mobilities of photoactive materials. The fill factors (FFs) of high-efficiency BHJ-based solar cells generally degrade significantly for thicknesses >100 nm [4, 18]. This limitation on active layer thickness raises particular issues for the scaling of solution-processed organic solar cells. For example, thin films on rough substrates are susceptible to point defects, which scale with area [19]. Relatively small variations in thin junctions result in large differences in device performance and thus in poor reproducibility [20]. Further, thin junctions (≈100 nm) limit the range of high throughput deposition techniques for manufacturing. Some donor polymers that enable high performance even in thick BHJ films in

solar cell devices have been reported, and most of them show high crystallinity in the solid state [21]. For instance, Yan et al. have reported highly crystalline donor polymers which produce high efficiencies and high FFs even in thick active films with a thickness of 300 nm [12]; P3HT:indene-C_{60} bis-adduct (ICBA) solar cells operate with a relatively high active layer thickness of ≈200 nm, exhibiting a PCE of 7.4–7.5% [22]. However, many high-performance crystalline polymers have a strong tendency to aggregate in solution, which makes film deposition difficult and disrupts the scaling of the solar cell.

An efficient strategy for improving polymer processability is reducing the regularity of polymers by random polymerization using different structural moieties. In particular, the development of random terpolymers has emerged as a popular approach for modulating the morphological properties of D-A copolymers without degrading their electrical and optical properties [23-24]. The incorporation of two donor or acceptor units, which have a similar chemical structure, into the main backbone is expected not only to slightly decrease the regioregularity of the polymer and improve the solubility of polymer but also to enable dense packing in the solid state because its backbone planarity is not perturbed.

In this research, D_1-A-D_2-A-type random terpolymers were synthesized by copolymerizing a 5,5'-bis(trimethylstannyl)-2,2'-bithiophene (2T) and a 4,7-diboromo-5,6-difluoro-4,7-bis(thiophen-2-yl)-2,1,3-benzodithiadiazole (2FBT-2T) so that a certain ratio of the 2FBT-2T compound is replaced with a 5,6-difluoro-2,1,3-benzothiadiazole (FBT) compound. This random polymerization strategy with a small proportion of FBT obviously decreases the over aggregation of the high crystalline D-A copolymer FBT-Th4 but still produces densely packing structure and the appropriate phase separation in the solid states for random copolymers. As a result, the photovoltaic device performance based on copolymer PDT2fBT-BT10, which contains 10 mol% FBT units, achieved up to 10.31%, which is significantly higher than that of the FBT-Th4 polymer. Furthermore, the preparation of uniform BHJ film with a thickness of 250-380 nm was attainable owing to the excellent processability of PDT2fBT-BT10 even over large areas. Hence, a solar cell with a large area of 1 cm^2 based on thick PDT2fBT-BT10 film with a thickness of 351 nm could be fabricated and this device exhibited an impressive power conversion efficiency up to 9.42%, which is one of the highest reported performances for a large-area OPV with thick BHJ film more than 300 nm.

Results and discussion

Synthesis and characterization

The FBT-Th4 polymer and random copolymer derivatives with a difference in molar ratio of 2FBT-2T and FBT were synthesized by Stille coupling reactions in chlorobenzene (CB) solvent with $Pd_2(dba)_3$ and $P(o\text{-}tolyl)_3$ as the catalyst, as shown in Scheme 1. After the polymerization reaction, the polymers were collected by precipitation in methanol and purified by successive Soxhlet extraction with methanol, ethyl acetate, hexane, and dichloromethane to remove the byproducts and oligomers. The molecular weight of the polymers was estimated with gel permeation chromatography at 80°C, and

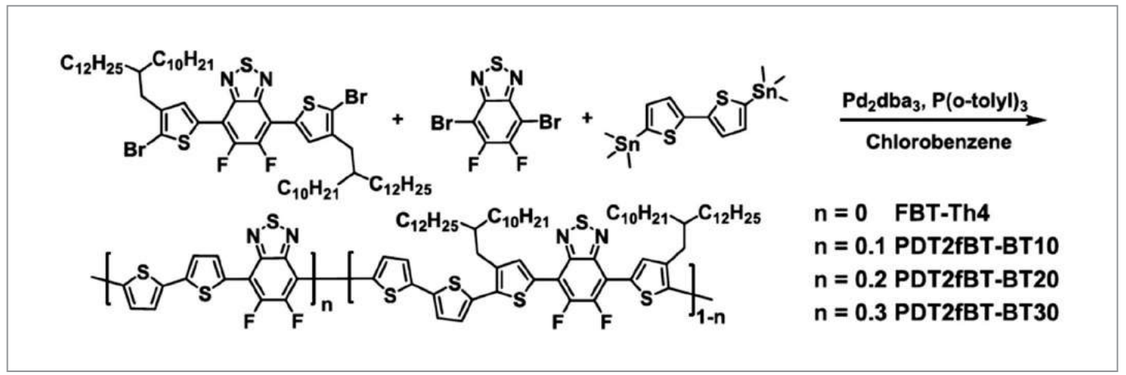

Scheme 1 Synthetic scheme for the polymers.

found to be M_n = 44.1 Kg mol-1 for FBT-Th4, 55.5 Kg mol^{-1} for PDT2fBT-BT10, 46.7 Kg mol^{-1} for PDT2fBT-BT20 and 57.6 Kg mol^{-1} for PDT2fBT-BT30 with polydispersity indices of 1.28, 2.00, 3.22, and 2.07, respectively.

Optical and electrochemical properties

The optical properties of the synthesized polymers were recorded with UV–vis absorption spectroscopy. The absorption spectra of the polymers in chlorobenzene and as thin films are presented in Figure 1, and their absorption properties are summarized in Table 1. Two characteristic absorption peaks were observed within the visible region for all the polymers in solution spectra. Each polymer exhibits similar absorption behaviors in its solution and solid-state spectra at room temperature, i.e., a 0-0 absorption peak at ≈700 nm and two 0–1 and 0–2 shoulder peaks at ≈630 and ≈450 nm, as shown in Figure 1a. The absorption peak at ≈450 nm corresponds to the π–π* transition of the conjugated backbone, whereas the absorption peak in the range 550–800 nm corresponds to the intramolecular charge transfer (ICT) between the electron-donating and electron-accepting units. In solution, the 0–0 absorption peak of the polymers shows different intensities; the 0–0 absorption peak of PDT2fBT-BT10 in solution is the least pronounced, which implies that its polymer chain is randomized. The onset absorptions of the polymers in their solid states (Figure 1b) are redshifted with respect to those of solution states. When the ratio of FBT in the polymer increases further, the redshift decreases remarkably from 21nm for PDT2fBT-BT30 to 9 nm for PDT2fBT-BT20 and 6 nm for PDT2fBT-BT30. Therefore, a small proportion of FBT ensures that the polymer chain adopts random conformation, which means that it is well solubilized and will form a good packing structure in films. The optical bandgaps (E_g) estimated from the onset on absorption are similar: 1.62, 1.62, 1.64, and 1.64 eV for FBT-Th4, PDT2fBT-BT10, PDT2fBT-BT20, and PDT2fBT-BT30, respectively.

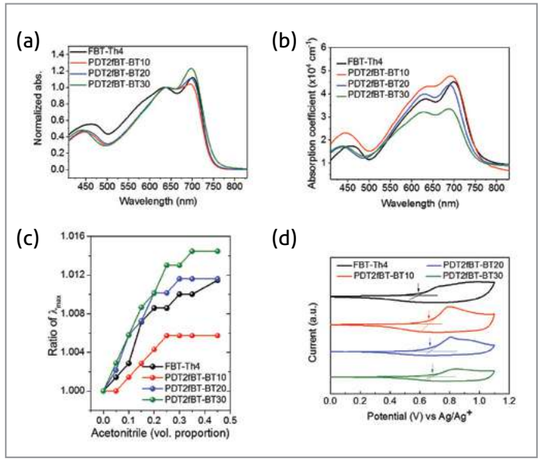

Figure 1 UV–vis absorption spectra of the polymers (a) in solution and (b) in the solid state. (c) Ratios of λ_{max} (= λ_{max} at Vol_{AcCN}/λ_{max} at pure chlorobenzene) as functions of the AcCN volume proportion. (d) Cyclic voltammogram of the polymers.

Interestingly, PDT2fBT-BT10 has the largest absorption coefficient in the film, followed by FBT-Th4 and PDT2fBT-BT20, which have similar absorption coefficients to each other. PDT2fBT-BT30 has the lowest absorption coefficient of the polymers.

The UV-vis absorption spectra were measured for the polymers dissolved in chlorobenzene at a concentration of 1 X 10^{-5} M with various volume ratios of polar solvent acetonitrile (Vol_{AcCN}) in a range of 0-0.5. Figure 1c shows ratios of λ_{max} at Vol_{AcCN} to λ_{max} at pure chlorobenzene as a function of Vol_{AcCN}. The λ_{max} values are redshifted to the longer wavelengths as the volume proportion of $_{AcCN}$ increases, which is ascribed to increases in polymer aggregation resulting from decreases in solubility. Interestingly, this redshift does not continue for PDT2fBT-BT10 once Vol_{AcCN} reaches 0.25; PDT2fBT-BT10 exhibits the same λ_{max} throughout the Vol_{AcCN} range 0.25–0.5.

Table 1 Summary of optical properties of polymers.

Polymer	λ_{max} solution [nm]	λ_{max} film [nm]	$\lambda_{on\ set}$ solution [nm]	$\lambda_{on\ set}$ film [nm]	$\Delta\lambda_{on\ set}$ solution to film [nm]	E_g[a)] [eV]	α_{max} film [x 10^4 cm^{-1}]
FBT-TH4	701	701	752	765	13	1.62	4.52
PDT2fBT-BT10	697	691	746	746	21	1.62	4.77
PDT2fBT-BT20	698	690	747	747	9	1.64	4.39
PDT2fBT-BT30	698	687	751	751	6	1.64	3.33

[a)] Determined from onsets of UV-vis absorption spectra in a film state

In contrast, the λ_{max} values of FBTTh4 and PDT2fBT-BT30 shift continuously with increases in the solvent polarity; the degree of redshift for these polymers when Vol_{AcCN} = 0.5 is much higher than that of PDT2fBT-BT10. This result indicates that the solubility of PDT2fBT-BT10 is much better than that of FBT-Th4. However, further incorporation of FBT units into the polymers does not substantially enhance their solubility. This effect arises because replacement of 2FBT-2T units with FBT reduces the number of solubilizing alkyl-side chains in the polymer chain, which decreases solubility.

The electrochemical properties of the polymers were characterized by cyclic voltammetry (Figure 1d). The HOMO energy levels were determined from the onset oxidation potentials and show a slight decrease as the proportion of FBT in the polymer increases: FBT-Th4 (−5.35 eV) > PDT2fBT-BT10 (−5.42 eV) > PDT2fBT-BT20 (−5.43 eV) > PDT2fBT-BT30 (−5.44 eV). The LUMO energy levels calculated from the HOMO energy levels and E_g are −3.73, −3.80, −3.79, and −3.80 eV for FBTTh4, PDT2fBT-BT10, PDT2fBT-BT20, and PDT2fBT-BT30, respectively.

Photovoltaic properties

The bulk heterojunction solar cells were fabricated with the device structure of ITO/polyethylenimine ethoxylated(PEIE)/polymer: [6,6]-phenyl C_{71} butyric acid methyl ester (PC71BM)/MoO3/Ag. The photoactive layers were deposited by spin-casting solutions of each polymer: $PC_{71}BM$ mixture in a CB/1-chloronaphthalene (97.5:2.5 vol%) co-solvent for FBT-Th4, PDT2fBTBT10, and PDT2fBT-BT20 and CB/1,2-dichlorobenzene (1:1 v/v) with 3 vol% of diphenyl ether for PDT2fBT-BT30. The optimized polymer $PC_{71}BM$ ratios that provided the best solar cell performance were 1:1.5, 1:2, 1:1.5, and 1:1.5 for FBT-Th4, PDT2fBTBT10, PDT2fBT-BT20, and PDT2fBT-BT30, respectively. Photovoltaic performance was studied under simulated AM 1.5G 1 sun illumination (100 mW cm^{-2}). The current density–voltage (*J–V*) curves for the solar cell devices are shown in Figure 2a, and the solar cell parameters are summarized in Table 2. The PDT2fBT-BT10 device shows the highest performance, with a PCE value of 10.31%, a short-circuit current density (J_{sc}) of 18.92 mA cm^{-2}, a FF of 73.45%, and an open-circuit voltage (V_{oc}) of 0.742 V. This efficiency is higher than that of the FBT-Th4 device with enhancements of PCE attributed mainly to the improved J_{sc} and FF. The device based on the random copolymer PDT2fBT-BT20 also exhibits better J_{sc} and FF values than the FBT-Th4 device, which results in an improved PCE of 9.28%. However, when the proportion of FBT is increased further, i.e., PDT2fBT-BT20 is replaced

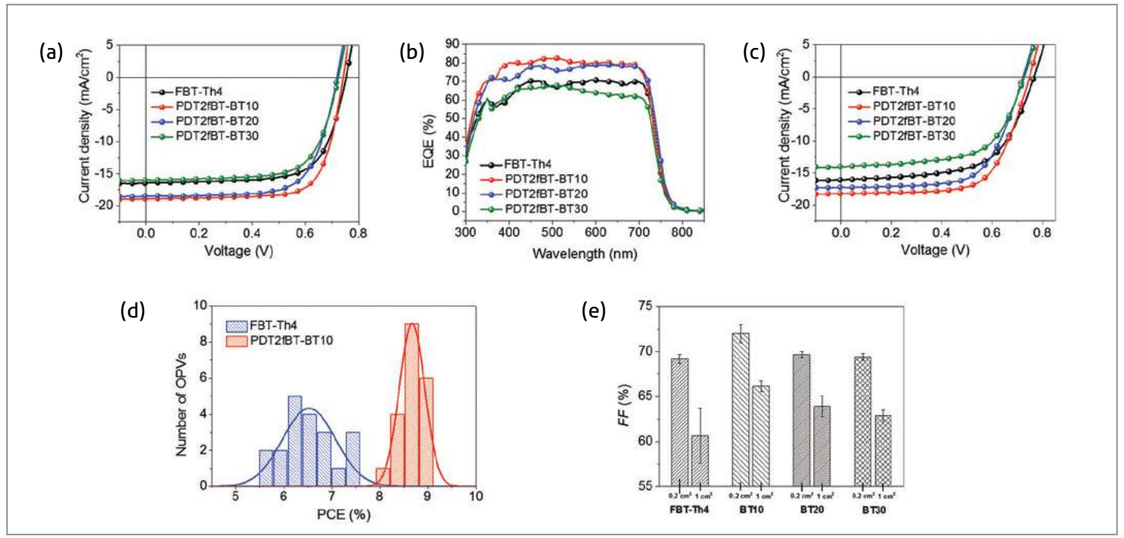

Figure 2 (a) *J–V* curves and (b) EQE spectra of the solar cells (active area = 0.2 cm^2). (c) *J–V* curves of the devices (active area = 1 cm^2). (d) Histogram of the PCE deviations obtained from 20 solar cells (active area = 1 cm^2). (e) The average FF values of the solar cells with active areas of 0.2 and 1 cm^2.

Table 2 Photovoltaic performance of the BHJ solar cells.

Polymer	V_{SC} [V]	J_{SC} [mA cm^{-2}]	FF [%]	PCE_{max} [%]	PCE_{avg} [%]	Active area [cm^{-2}]
FBT-Th4	0.753	16.48(16.06)[a]	69.52	8.62	8.51 ± 0.08	0.20
PDT2fBT-BT10	0.740	18.82(18.53)[a]	73.45	10.31	10.07 ± 0.17	0.20
PDT2fBT-BT20	0.719	18.46(18.15)[a]	69.73	9.28	9.09 ± 0.16	0.20
PDT2fBT-BT30	0.724	16.00(14.98)[a]	69.21	8.02	7.75 ± 0.17	0.20
FBT-Th4	0.762	15.80	61.04	7.35	6.53 ± 0.54	1.00
PDT2fBT-BT10	0.748	18.23	66.23	9.03	8.67 ± 0.26	1.00
PDT2fBT-BT20	0.723	17.24	64.84	8.10	7.71 ± 0.26	1.00
PDT2fBT-BT30	0.728	14.01	62.21	6.35	6.13 ± 0.35	1.00

[a] Determined from onsets of UV-vis absorption spectra in a film state

with PDT2fBT-BT30, the performance of the resulting device is inferior to that of the FBT-Th4 device with a PCE of 8.02%. Thus, the synthesis of a random copolymer with a small proportion of FBT provides enhanced solar cell properties, in particular J_{sc} and FF, compared to those of the polymer device.

Figure 2b illustrates the external quantum efficiency (EQE) spectra of the solar cells. PDT2fBT-BT10 exhibits larger EQE values than the others, as high as 75-80% along a wavelength range of 350–750 nm, which is 10–20% higher than those of FBT-Th4. This result is solidly consistent with the result of the highest J_{sc} of the PDT2fBT-BT10-based solar cell. The onset wavelength of the PDT2fBT-BT30 is slightly blueshifted with respect to those of the other in the EQE spectra, which arises because the energy bandgap of PDT2fBT-BT30 is higher than those of the other polymers, as is in agreement with its absorption properties. The $J_{sc,EQE}$ values calculated from integrating the EQE spectra are close to the J_{sc} values obtained from the *J-V* curves, which suggests that the *J-V* measurements are highly reliable.

Large area solar cells with an active area of 1 cm^2 were fabricated with same device structure and preparation conditions as small area devices. The *J-V* curves and solar cell characteristics of large area devices are shown in Figure 2c and Table 2. The performance of the polymers decreases as the active area increases, but their performance ranking is maintained. When the active area is increased, V_{oc} is relatively well preserved while the efficiency drop is mostly due to decreases in the J_{sc} and FF values. The histograms of the PCE deviations of the 20 solar cell devices with an active area of 1 cm^2 are displayed in Figure 2d. The average PCEs are 6.53±0.54% and 8.67±0.26% for FBT-Th4 and PDT2fBT-BT10, respectively. Interestingly, the PCE distribution of the PDT2fBT-BT10-based OPVs is narrow, which indicates much-improved device reproducibility. Figure 2e shows the average FF values of the polymers for active areas of 0.2 and 1 cm^2. Upon increasing the active area from 0.2 to 1 cm^2, the reduction in FF is smallest for PDT2fBT-BT10 and PDT2fBT-BT20, only 8%, and largest for FBT-Th4, 13%. The primary reason for this performance drop is the sheet resistance of the ITO film [25-26]. In addition, the large FF change that arises when the active area is increased in the FBT-Th4 OPV is due to the unoptimized morphology of the large-area BHJ film, which contains defects and heterogeneities. The atomic force microscopy (AFM) measurements (Figures 3a-b) demonstrate that the PDT2fBT-BT10:PC BM blend film has a smooth surface (a root-mean-square (RMS) roughness of 2.37 mm) and continuous phase separation domains, whereas the FBT-T4 blend film has a higher surface roughness (RMS = 3.42 nm) and low film homogeneity with some several hundred nanometer spots, which are thought to be active material aggregates. These heterogeneities in the FBT-Th4 active layer are most likely to cause local variations of the photo-generated current in the associated solar cells, as well as a reduced FF. When applied in a large-area device, this unoptimized film morphology probably leads to a large efficiency decrement and low-performance reproducibility.

We measured the variation with position in the efficiency of a solar cell based on PDT2fBT-BT10 with an active area of 1 cm^2 by using a 0.2 cm^2 shadow mask. Importantly, the average efficiency of 9 measurements for different positions is 9.70% for PDT2fBT-BT10, which is very close to that obtained for the device with an active area of 0.2 cm^2, and there are only small variations in the measured efficiency values, as shown in

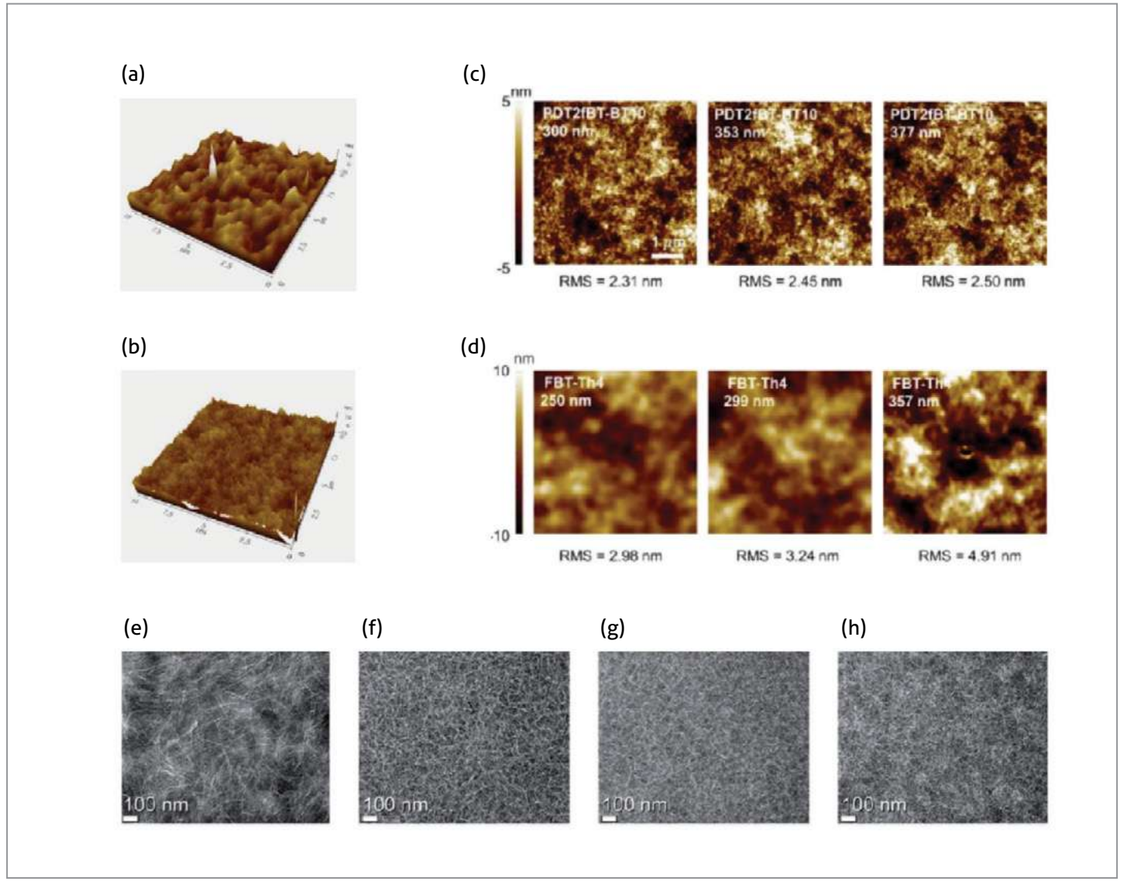

Figure 3 AFM images of the BHJ films for (a) FBT-Th4 and (b) PDT2fBT-BT10. AFM images of (c) the FBT-Th4 and (d) PDT2fBT-BT10 BHJ blend films with different film thicknesses. TEM images of (e) FBT-Th4, (f) PDT2fBT-BT10, (g) PDT2fBT-BT20, and h) PDT2fBT-BT30.

Figure 4a. This result indicates that the PDT2fBT-BT10 BHJ film has high homogeneity. When compared to the optimized devices with 0.2 cm^2 active areas, the 1 cm^2 OPVs exhibit no additional current loss other than charge carrier reduction due to the sheet resistance of the ITO film. On the contrary, there is a large variation in the PCE depending on the specific position in the measurements for the FBT-Th4-based solar cells with a 0.2 cm^2 shadow mask, shown in Figure 4a (average efficiency for nine positions: 7.87%). This demonstrates that the heterogeneity of the BHJ film results in variation in the efficiency; for example, if the region of the BHJ film exposed by the aperture in the shadow mask includes large aggregates, this region is likely to exhibit an efficiency that is inferior to those of other positions in the 1 cm^2 OPV.

Figures 4b–d display the variations of BHJ thickness in the solar cell parameters of the 1 cm^2 FBT-Th4 and PDT2fBT-BT10 devices. In the case of PDT2fBT-BT10, there is only a weak dependence of the PCE on thicknesses up to 380 nm, whereas the PCEs of FBT-Th4 drop rapidly in devices with BHJ films thicker than 300 nm. Therefore, it is expected that PDT2fBT-BT10 forms the optimal morphology for charge

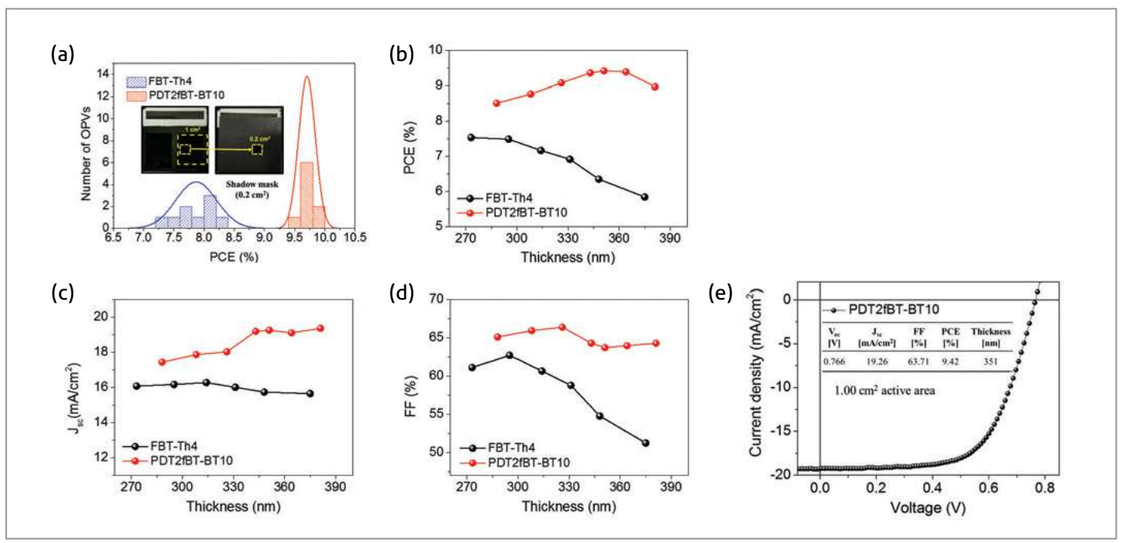

Figure 4 (a) PCE histogram of 1 cm^2 solar cells obtained from nine positions using a 0.2 cm^2 shadow mask. Evolution of solar cell parameters with the active layer thickness, (b) PCE, (c) J_{sc}, and (d) FF. (e) *J–V* curve of PDT2fBT-BT10 solar cell (active area = 1 cm^2, thickness of active layer = 351 nm).

generation and transport even in BHJ films thicker than 350 nm, whereas the low solubility and strong tendency to aggregate of FBT-Th4 might induce inhomogeneous large-area FBT-Th4 BHJ films with severe aggregation. The AFM of the FBTTh4 and PDT2fBT-BT10 BHJ films were measured in varying thicknesses from 250 to 380 nm; the resulting images are shown in Figures 3c-d. Interestingly, the PDT2fBT-BT10 BHJ films do not show any obvious change in morphology since the roughness values remain in the 2.3-2.5 nm range as film thickness is increased. In contrast, higher film roughness was observed for the thicker FBT-Th4 BHJ film; i.e., the RMS value increased from 2.98 nm for 250 nm thickness to 4.91 nm for 357 nm thickness. This illustrates the reason why the FBT-Th4 solar cell shows a decreased PCE when the BHJ film thickness is increased. Consequently, solar cells based on PDT2fBT-BT10 achieved a PCE up to 9.42% on a 351 nm thick and 1 cm^2 active layer as shown in Figure 4e. This performance is among the highest for OPVs with 1 cm^2 active areas and BHJ films with thicknesses >300 nm.

Grazing incidence wide- and small-angle X-ray scattering studies

To investigate the molecular orientations of the polymers and their crystallographic properties in the blend films, grazing incidence wide-angle X-ray diffraction (GI-WAXD) measurements were performed, and results are shown in Figure 5. Figure 5a displays the 2D GI-WAXD patterns for the FBT-Th4, PDT2fBT-BT10, PDT2fBT-BT20, and PDT2fBTBT30 blend films. FBT-Th4 and PDT2fBT-BT10 produce (100) and (200) diffraction patterns in the in-plane and out-of-plane directions, which means mixtures of face-on and edge-on orientations. In contrast, PDT2fBT-BT20 and PDT2fBT-BT30 produce more intense (100) and (200) diffraction peaks in the out-of-plane direction, which indicates that most of the crystallites of PDT2fBT-BT20 and PDT2fBT-BT30 have an edge-on orientation in their blend films.

The q_{xy} and q_z profiles were extracted from the 2D GI-WAXD patterns and are presented in Figures 5b-c. All the polymers produce multiple reflections in the form of (n00) and (010) diffraction peaks along the in-plane and out-of-plane directions and diffused diffraction peaks are evident at q_{xy} or q_z = 0.7 and 1.32 $Å^{-1}$, which are attributed to the aggregation of $PC_{71}BM$ [27]. In the in-plane profile of the FBT-Th4 blend film, there are multiple reflection peaks correlated to the (100), (200), (300), and (400) diffractions and corresponding lamellar distance ($d_{(100)} = 2\pi/q_{(100)}$*) is calculated to be 24.6 Å. The (010)

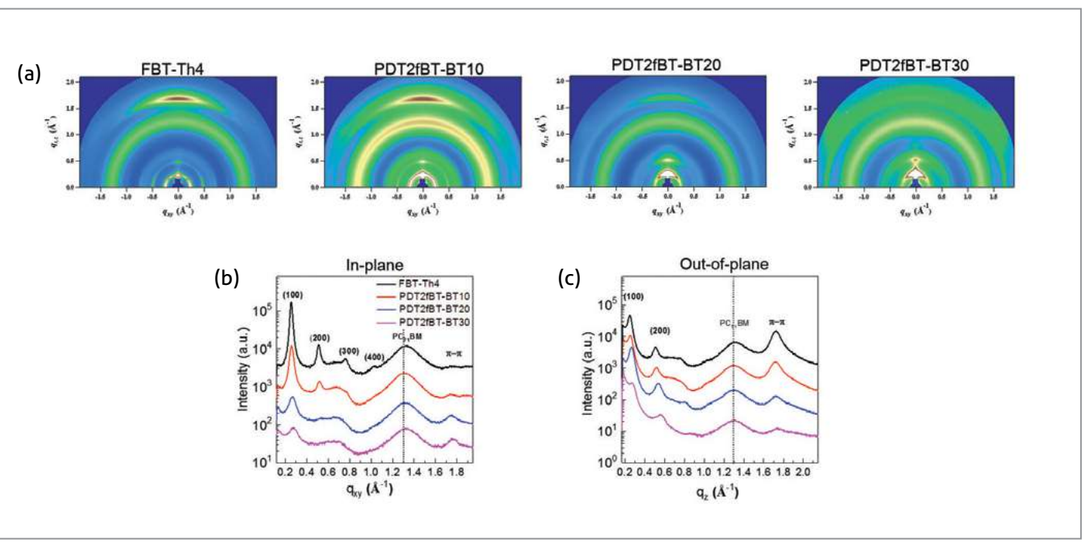

Figure 5 (a) GI-WAXD images of the BHJ films. Line-cut profiles (b) in-plane and (c) out-of-plane.

peak at q_z = 1.745 $Å^{-1}$ of the FBT-Th4 pattern in the out-of-plane direction is associated with a π- π stacking distance of 3.6 Å, which is a typical feature of a face-on arrangement of the polymer with respect to the substrate. The other random copolymers produce (100) and (010) diffraction peaks at similar positions. From the full width at half-maximum of each (100) diffraction peak, the coherence length ($Lc_{(100)}$) was calculated using a simple Scherrer equation. The $Lc_{(100)}$ values for FBTTh4, PDT2fBT-BT10, PDT2fBT-BT20, and PDT2fBT-BT30 along the in-plane direction (i.e., at q_{xy}) were estimated to be 224.3, 143.7, 87.9, and 77.8 Å, respectively. These results indicate that the FBT-Th4 blend film contains the largest crystallites. The $Lc_{(100)}$ of the polymers decreases with increases in the FBT content of the random copolymer backbone, which is related to a decrease in the crystallinity. Larger crystallites enhance charge transport; however, the crystal size of FBT-Th4 is a little larger than the exciton diffusion length of 10–20 nm in the bulk heterojunction film, which causes a reduction in charge carrier generation at the polymer/$PC_{71}BM$ interface. The crystal size of PDT2fBT-BT10 is the most appropriate for charge generation and transport. The tendency in the coherence lengths of the polymers is significantly consistent with the TEM results, as shown in Figures 3e–h. The TEM image of the FBT-Th4 blend film in Figure 3e shows clear fibril structures with widths of 30–40 nm due to polymer aggregation. As FBT units are more incorporated in the random copolymers, the copolymer films contain finer and more well-dispersed fibrous structures with widths on the 10 nm scale.

Studies of charge generation, charge transport, and charge recombination properties of the solar cells

The charge carrier mobilities of the polymer pristine and BHJ films were estimated using a space charge limited current model by fitting the J1/2–V curves. The hole mobilities in the blend films are slightly decreased from the corresponding values in the polymer pristine films. The PDT2fBTBT10 blend film has the highest hole mobility, 8.45 × 10^{-3} cm^2 V^{-1} s^{-1}, and PDT2fBT-BT20 (5.39 × 10^{-3} cm^2 V^{-1} s^{-1}) and FBTTh4 (5.17 × 10^{-3} cm^2 V^{-1} s^{-1}) have similar hole mobilities to each other. The high hole mobility of PDT2fBTBT10 is more likely due to the fact that its BHJ film contains relatively large crystallites with a face-on orientation and the appropriate phase separation and network structure for efficient charge transport. The electron mobility is highest for the PDT2fBT-BT10 blend film, with

a value of 4.55×10^{-3} cm^2 V^{-1} s^{-1}, and the FBT-Th4 blend film (3.48×10^{-3} cm^2 V^{-1} s^{-1}) has a similar electron mobility to the PDT2fBT-BT20 blend film, 3.02×10^{-3} cm^2 V^{-1} s^{-1}. PDT2fBTBT30 has the lowest electron mobility, 1.07×10^{-3} cm^2 V^{-1} s^{-1}.

In order to investigate the carrier recombination in the active layers, J_{sc} was measured as a function of incident light intensity (P_{light}) and the data were fitted to the power law $J_{sc} \propto P_{light}\alpha$, as shown in Figure 6a [28-29]. The exponent α for the PDT2fBT-BT10-based cells is the highest of those of the polymers, α = 0.94, while α = 0.93 for PDT2fBT-BT20, which is higher than those of FBT-Th4 (α = 0.92) and PDT2fBTBT30 (α = 0.91). From this result, it is proved that bimolecular recombination is the lowest in the PDT2fBT-BT10-based solar cell device under short-circuit conditions. This result is in good agreement with the results for the charge mobilities, which decrease in the order PDT2fBT-BT10 > PDT2fBT-BT20 ≥ FBTTh4 > PDT2fBT-BT30. The high FF value of the PDT2fBT-BT10 device is responsible for its excellent charge transport and its decreased charge recombination. To explore charge generation, dissociation, and extraction properties of the solar cells, the photocurrent density (J_{ph}) was measured as a function of the effective voltage (V_{eff}). Note that ($J_{ph} = J_L – J_D$, where J_L and J_D are the current densities under illumination at 100 mW cm^{-2} and in dark conditions, respectively, and that $V_{eff} = V_0 – V_a$, where V0 is the voltage when $J_{ph} = 0$ and V_a is the applied bias [28-29]. The exciton dissociation probability (P(E,T)) under short-circuit conditions was calculated for each device using the equation $J_{ph} = J_{sat}$·P(E,T), where J_{sat} is the saturation photocurrent density (Figure 6b). The PDT2fBT-BT10-based device shows the highest P(E,T) value of 97.9%, which implies its superior charge generation capability, followed by PDT2fBT-BT20 (P(E,T) = 95.5%) and PDT2fBT-BT30 (P(E,T) = 95.3%). The FBT-Th4-based device exhibits the lowest P(E,T) value, 92.5%, which is most likely due to the large-scale donor–acceptor phase separation and aggregation in its BHJ film.

From the results of charge generation and recombination studies, it is concluded that the PDT2fBT-BT10-based solar cell exhibits superior J_{sc} and FF values to those of the FBT-Th4 device because of the following advantages: 1) random terpolymerization with a small proportion of FBT maintains the advantage of physical properties of the D-A copolymer, including its preference of face-on orientation with high crystallinity; (2) the sizes of the polymer crystallites in the BHJ film are appropriate to both charge generation and transport; and (3) the improved morphology and suitable phase

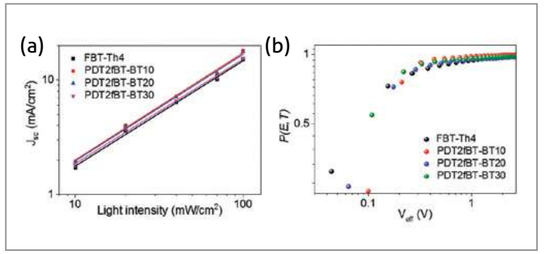

Figure 6 (a) Variations in J_{sc} with light intensity and (b) extracted exciton dissociation probability [*P(E,T)*] versus effective voltage (V_{eff}) plots.

separation effectively reduce charge recombination and enhance the photocurrent. In addition, the improved solubility and processability of the polymer facilitate highly reproducible and scalable BHJ film formation with the optimal morphology. The D_1-A-D_2-A-type random terpolymerization of a small proportion of the D_2 unit increases the solubility and processability of this high crystalline polymer and preserves its advantageous electrical properties. This approach not only enhances the solar cell's efficiency but also makes it possible to reproduce its high performance in a solar cell device with a large active area.

Conclusions

We developed random terpolymers by copolymerizing 2T with various proportions of 2FBT-2T and FBT. The introduction of a small proportion of FBT effectively increases the solubility and processability of polymers and reduces the over aggregation of high crystalline polymers. When compared to the copolymer FBT-Th4, PDT2fBT-BT10 shows comparable high crystalline packing features with a dominant face-on orientation in its polymer:$PC_{71}BM$ blend film and also much improved BHJ morphology with the appropriate phase separation. Consequently, the PDT2fBTBT10- based solar cell exhibits a much-enhanced efficiency of 10.31% compared to that of the FBT-Th4 (8.62%). In addition, the excellent processability of PDT2fBT-BT10 enables the optimal BHJ nanomorphology to be reproduced over a large area without any significant defect formation or aggregation. As a result, OPVs with a 1 cm^2 active area and a 351 nm thick BHJ film were found to produce a high photovoltaic performance of 9.42% with great reproducibility, while OPVs based on the copolymer FBT-Th4 with an active area of the same size exhibit

rapid reductions in PCE for thicknesses above 300 nm. This performance is among the highest for OPVs with 1 cm^2 active areas and BHJ films with thicknesses >300 nm. This research also provides new insights for designing donor polymers that can enable formation of thick film and scaled-up BHJ junctions with high photovoltaic performance. These results also contribute to the further commercial development of organic solar cells by enabling the manufacture of large-area and highly-reproducible thick BHJ films.

Note

This article and images are drawn from "High-Performance and Uniform 1 cm^2 Polymer Solar Cells with D_1-A-D_2-A-Type Random Terpolymers" in *Advanced Energy Materials* 2018; 8: 1701405.

References

[1] Hong S et al. *Nat. Commun*. 2016; 7: 10279.
[2] Huang J et al. *Adv. Energy Mater*. 2015; 5: 1500406.
[3] Søndergaard R et al. *Mater. Today* 2012; 15: 36-49.
[4] Chen HY et al. *Nat. Photonics* 2009; 3: 649-653.
[5] Son HJ et al. *J. Am. Chem. Soc*. 2011; 133: 1885-1894.
[6] Lu L et al. *Chem. Rev*. 2015; 115: 12666-12731.
[7] Li W et al. *J. Am. Chem. Soc*. 2014; 136: 15566- 15576.
[8] Zhang M et al. *Adv. Mater*. 2014; 26: 1118-1123.
[9] Jhuo HJ et al. *Adv. Funct. Mater*. 2016; 26: 3094-3104.
[10] Ma W et al. *Adv. Energy Mater*. 2015; 5: 1501400.
[11] van Franeker J et al. *Adv. Energy Mater*. 2015; 5: 1500464.
[12] Liu Y et al. *Nat. Commun*. 2014; 5: 5293.
[13] Nam S et al. *Nat. Commun*. 2015; 6: 8929.
[14] Nielsen CB et al. *Acc. Chem. Res*. 2015; 48: 2803-2812.
[15] You J et al. *Nat. Commun*. 2013; 4: 1446.
[16] Gehlhaar R et al. Presentation at SPIE Organic Photonics+Electronics, San Diego, August 2013.
[17] Pfeiffer M. Presentation at MRS Fall Meeting, Boston, MA, December 2013.
[18] Small CE et al. *Adv. Energy Mater*. 2013; 3: 909.
[19] Duan C et al. *Polym. Chem*. 2015; 6: 8081.
[20] Armin A et al. *Laser Photonics Rev*. 2014; 8: 924-932.
[21] Duan C et al. *Polym. Chem*. 2015; 6: 8081-8098.
[22] Guo X et al. *Energy Environ. Sci*. 2012; 5: 7943-7949.
[23] Duan C et al. *J. Am. Chem. Soc*. 2016; 138: 10782-10785.
[24] Jo JW et al. *Adv. Energy Mater*. 2017; 7: 1601365.
[25] Dkhil SB et al. *Adv. Energy Mater*. 2016; 6: 1600290.
[26] Jin H et al. *Phys. Status Solidi. A*. 2015; 212: 2246-2254.
[27] Bartelt JA et al. *Adv. Energy Mater*. 2013; 3: 364.
[28] Zhang Q et al. *Nat. Photonics* 2015; 9: 35-41.
[29] Zhang L et al. *Sci. Rep*. 2014; 4: 5071.

Feature Articles

Ultrastretchable Conductor Made With Hydrogel-Elastomer Hybrid Materials

Jae Min HONG
Director-General
KIST Jeonbuk Institute of
Advanced Composite Materials

jmhong@kist.re.kr

Introduction

Stretchable electronics are widely used in epidermal and wearable devices, soft robotics, and implants owing to their good attachment to curved surfaces like cloth, organs, and skin [1]. The majority of stretchable devices are comprised of two parts: an active (conductive) layer and a substrate. Various conductive components of stretchable electronic devices have been developed. Their substrates mostly consist of silicon rubber, polyethylene naphthalate, polyurethane polymers, or fluorinated rubber with a sub-hundreds kilo-Pascal or mega-Pascal range of modulus [2, 3]. The wearing comfort of skin-attached stretchable devices can be increased by lowering the elastic moduli of their substrates. Many attempts have been made recently to integrate organic-based stretchable conductors (such as poly(3,4-ethylenedioxythiophene)-polystyrenesulfonate) (PEDOT:PSS) [4] and carbon-based materials [5]) with hydrogels or printing methods; nevertheless, metals still remain superior to organic conductors in terms of conductivity [6].

The fabrication of stretchable electrodes composed of metallic materials can be realized using various approaches, including patterning metallic microstructures using micro- and nanomesh, and serpentine structures [7]. It has also been reported that the use of wavy [8] or porous structures [9] help to release strain. Several groups have suggested promising methods for producing stretchable conductors. Kirihara and co-workers demonstrated stretchability up to 600% with 2.4 Ω cm using Ag flake–polyurethane ink on polyurethane substrate [10]. Kotov and co-workers reported on a highly stretchable polyurethane–Au nanoparticle conductor that could make a conductive path by reorganized nanoparticles when stretched and which showed a conductivity of 35 S cm^{-1} at 485% strain [11]. In addition, Someya and co-workers described printable conductors with a high conductivity of 935 S cm^{-1} at 400% strain through *in situ* formation of silver nanoparticles from Ag flakes in a fluorinated rubber [12]. Recent research activity related to stretchable electrodes is summarized in Table 1.

Table 1 Comparison of electrical conductivity and stretchability results from recent research with stretchable conductors.

Work	Materials		Properties		Remarks
	Conductive filter	Matrix	Stretchability	Electrical property	
Nature. Mater (T.Someya)	SWNT	Fluorinated -copolymer	134% 38%	6 S cm^{-1} 57 S cm^{-1}	Stretchable
Adv. Mater	Ag/AgCl PEDOT	Ecoflex	200% 600%	30 Ω 52 kΩ	All-printed device
Adv. Healthcare Mater (M. Nishizawa)	REDOT	PU-Hydrogel	100%	127 S cm^{-1}	PEDOT-PU hybrid on hydrogel
IEEE Electron Device Lett. (O. Kirihara)	Ag flakes	PU	600%	2.8 x 10^{-4}Ω cm	Ag flake percolation
Nature (N. A. Kotov)	Au nanoparticles	PU	486% (VAF) 115% (LBL)	48 S cm^{-1} 2300 S cm^{-1}	Au nanoparticle self-organization
Nature. Mater (T. Someya)	Ag flakes	Fluorinated polymer	400%	935 S cm^{-1}	*in-situ* formation of Ag nanoparticle
J. Mater Chem. C. (J.-M. Hong)	Ag flakes	Ecoflex	**500**%	190 Ω	Photo-sintering for percolation
This work (J.-M. Hong)	Ag flakes	Ecoflex	**1780**%	501 Ω	Hydrogel-ecoflex hybrid substrate

Herein, we report a highly stretchable elastic conductor on a low-modulus hybrid substrate, exhibiting an elongation up to a break of 1780%. The fabricated hybrid film is composed of two layers: thin film Ecoflex and tough hydrogel. It has superior stretchability, with the above elastomer film playing a crucial role in binding the elastic conductor with the tough hydrogel, thus realizing ultrastretchability for the conductor. The technological applicability of the fabricated electrode was tested by employing it in the stretchable wiring of a light-emitting diode (LED) and as a component of a skin patch containing a pressure sensor.

Fabrication and analysis

A highly stretchable and printable elastic conductor fabricated from an ink containing a stretchable elastomer (Ecoflex) and Ag flakes was laminated on a hybrid substrate containing tough hydrogel and thin film Ecoflex (Figure 1a). The tough hydrogel, composed of a double-network water-containing polymer, has an elastic modulus similar to that of human skin and stretchability of over 2000% strain [13], thus making it an appropriate material for skin-like electronics. For interfacial compatibility with elastic Ag conductor, the tough hydrogel was coated with Ecoflex via benzophenone. The utilized silicon rubber (Ecoflex) in the ink exhibits high stretchability up to 700% as well as good compatibility with the methyl isobutyl ketone (MIBK) component of the ink system. Composition of the inks are shown in Figures 1b-c. Scanning electron microscopy (SEM) analysis shows an average Ag flake size of 1.9 μm. The initial state of the conductor transferred on the hybrid substrate is shown in Figure 1d. A very thin Ecoflex film with a thickness of 30 μm was coated onto the hydrogel surface (Figures 1e-f). After attaching these stretchable systems together, a highly stretchable conductor with excellent stretchability as high as 1780% was obtained (Figure 1g).

Figures 2a-c show a schematic representation of the fabrication of highly stretchable conductors by a simple transfer method. The fabrication process consisted of the following steps. First, a thin Ecoflex film was formed on a polyethylene terephthalate (PET) sheet via spin coating followed by surface treatment with benzophenone. After that, hydrogel solution was dropped on thin rubber film with a rectangular shape followed by ultraviolet curing to cross-link both the hydrogel and rubber layers (Figure 2a). Typically, screen-printed ink is sintered by

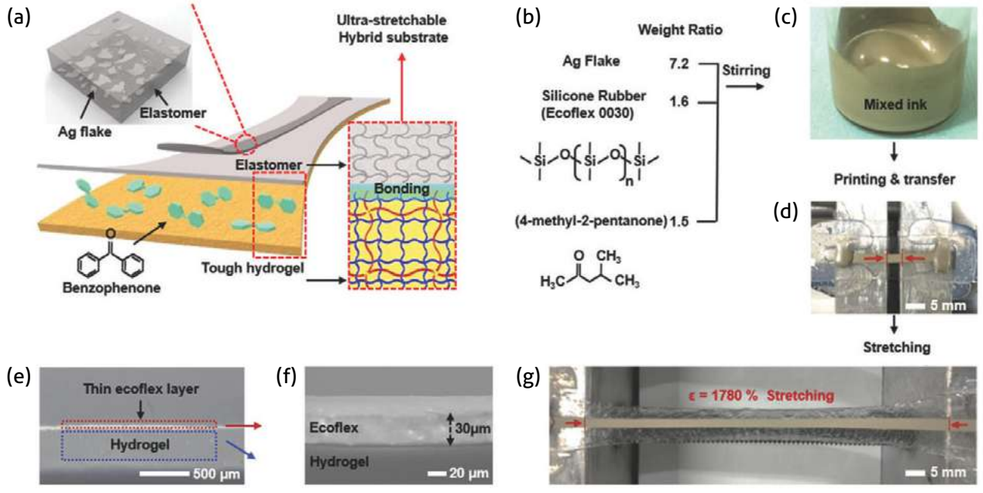

Figure 1 Fabrication of the stretchable conductor containing a hybrid substrate and conductive ink layer. (a) Schematic illustration of the conductor composition. The thin elastomer film is strongly bonded to the tough hydrogel layer by benzophenone. (b) Chemical structure of the ink component. Photographs of (c) the mixed ink and (d) the conductor transferred onto the substrate. The determined length of the conducting layer is indicated by the red arrows. (e) A hybrid substrate composed of a thin Ecoflex film (denoted by the red dashed box) and tough hydrogel layer (denoted by the blue dashed box). (f) A side-view SEM image of the hybrid film. (g) A stretchable conductor elongated up to 1780% strain.

thermal annealing or intense pulsed light [14]. However, both these methods result in the drying of the produced hybrid film, thus decreasing its stretchability since it is made of a water-containing hydrogel. Instead, a transfer method using water-soluble 3M tape can be used to attach printed Ag ink to the hybrid substrate conformally if adhesion of the tape to the conductor layer is stronger than that of the ink to the original substrate. Thus, the viscous ink in this work was first screen-printed on a Teflon layer and then sintered via thermal annealing before detaching it from the substrate (Figure 2b). Since the Teflon sheet possesses a hydrophobic surface, the printed ink often spread along one edge of the formed pattern, which decreased its resolution (this problem can be solved by varying the viscosity of the ink). After applying the detached ink onto the hybrid substrate conformally, deionized water was dropped on the film surface for fast dissolution of the tape (within several minutes) (Figure 2c). The degree of stretchability of the hybrid film was very close to that of pure Ecoflex and hydrogel films up to 400% (Figure 2d). However, these materials exhibit different elastic moduli and breakup points (their corresponding stress–strain curves are plotted in Figure 2e). The tensile modulus of the hydrogel layer was almost identical to that of the hybrid film since the rubber layer coated on the hydrogel surface was very thin. However, the tensile modulus of the Ecoflex layer was 170 times higher than that of the other two films. The lower elastic modulus of the substrate ensure its conformal contact with the curved surface of the skin and a higher degree of skin comfort during movement. In addition, a reliable conductor usually possesses good recovery properties. In this study, the hysteresis of the substrate was determined by stretching it to an elongation of 300% followed by a slow release. As a result, the recovery properties of the hybrid and hydrogel layers were found to be good compared to those of the Ecoflex film (Figure 2f). The elastic Ag conductor exhibited hydrophobic characteristics since it contained hydrophobic components such as Ag flakes and silicon rubber species, while the wet surface of the hydrogel remained hydrophilic. The thin Ecoflex film plays a very important role in the fabricated ultrastretchable conductor (Figures 2g-h). Normally, silicon rubber is highly compatible with the utilized hydrophobic conductor, which is

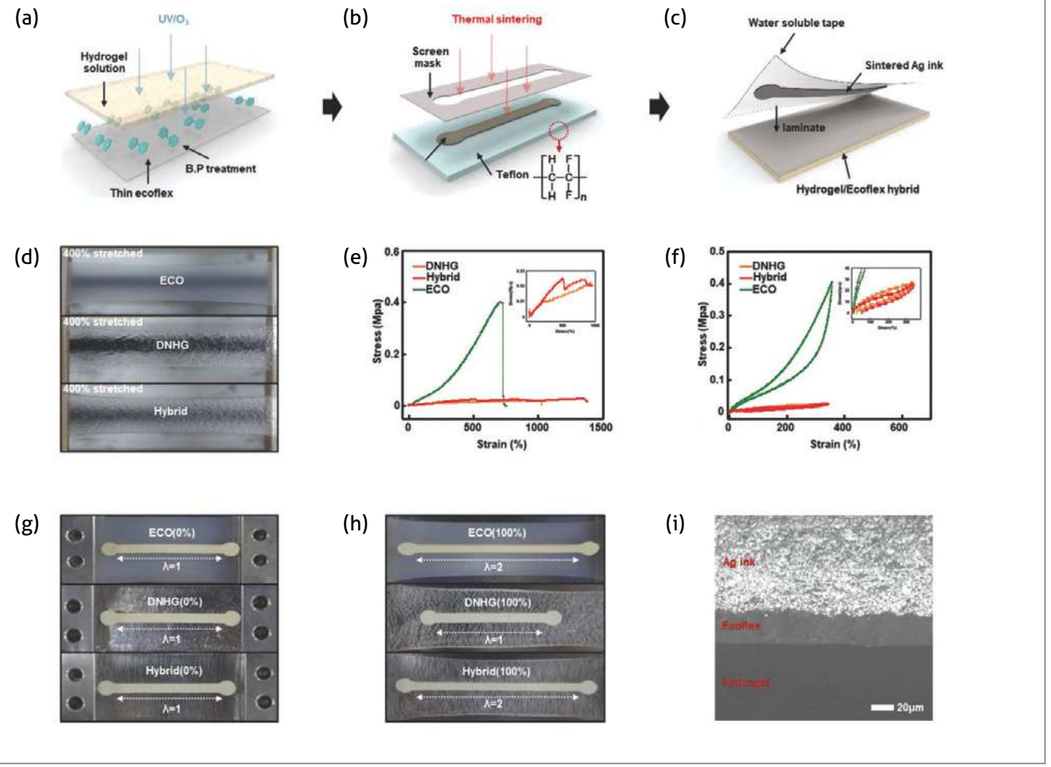

Figure 2 Fabrication method and substrate characterization. (a) The precured solution of the tough hydrogel is poured onto benzophenone (B.P.)-treated thin Ecoflex film followed by UV curing with ozone. (b) The conductive ink is screen-printed onto the Teflon substrate and thermally sintered inside the oven. (c) Transferring the sintered conductor from the Teflon to the hybrid substrate using water-soluble tape. (d) Stretching the Ecoflex (ECO), double-network tough hydrogel (DNHG), and hybrid films. (e) Strain–stress curves recorded for the three films. A comparison of the elastic moduli of the hybrid and DNHG films is shown in the inset. (f) A comparison of the hysteresis properties of the three films. (g,h) Stretching the conducting layers of the studied films. The thin Ecoflex film coated on the DNHG surface improves the slip resistance of the conductor. (i) A side SEM image of the stretchable conductor. The Ag ink layer is strongly attached to the hybrid film surface

stretched proportionally to the elongation of the substrate (see the upper parts of Figures 2g-h). After its attachment to the hydrogel substrate, the conductor exhibited no elongation during stretching owing to the slip motion on the substrate surface (see the middle parts of Figures 2g-h). This confirms that the thin Ecoflex film coated onto the hydrogel layer enhanced the slip resistance of the conducting layer (see the lower parts of Figures 2g-h). The cross-sectional SEM image of the conductor containing all three components is depicted in Figure 2i. It shows that the thin Ecoflex film located between the Ag conductor and the tough hydrogel had good contact with both layers. Three different types of the fabricated conductors were subjected to a stretching test: a conductor formed directly on the Ecoflex substrate via screen printing (ECO-P); a conductor transferred to the Ecoflex substrate (ECO-T), and a conductor transferred to the Ecoflex hydrogel hybrid substrate (Hybrid).

Application

To demonstrate feasible applications of the studied

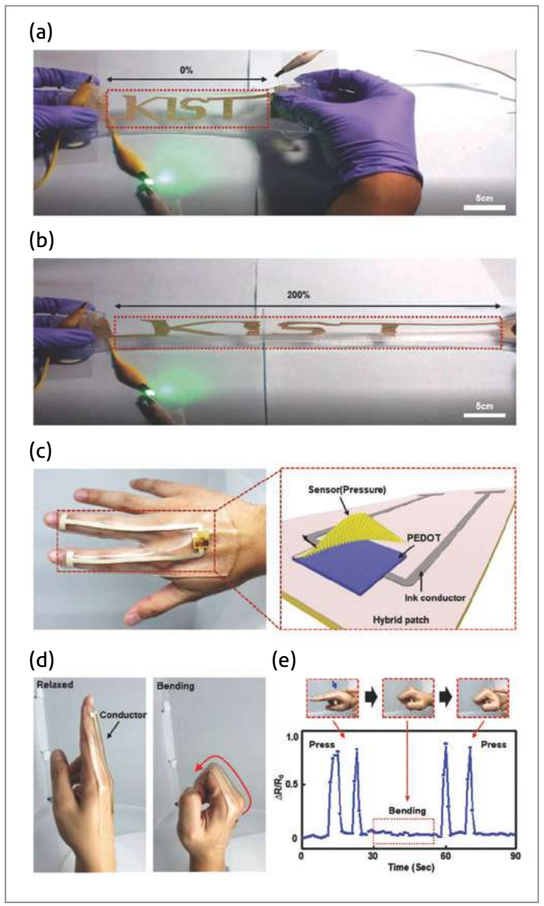

Figure 3 Application of the fabricated stretchable electrodes for LED wiring and smart skin patches. (a) The KIST-patterned ink transferred onto the hybrid film is connected to a commercial green LED. (b) The LED brightness remains almost the same during electrode stretching. (c) An image of the smart skin patch and schematic illustration of the pressure sensor structure. The sensor is composed of the microstructured Au thin film and PEDOT ink film connected to the Ag ink conductor wire on the hybrid film surface. (d) Relaxed and bending states of the smart skin patch attached to a human hand. The Ag ink conductor deforms during bending. (e) Performance of the pressure sensor on the smart skin patch during finger movements. The blue arrow indicates the pressure sensor.

conductor, we used it to fabricate the wiring line of an LED with a "KIST" pattern shape (Figure 3a). The green-colored LED emitted bright light after the patterned conductor was stretched at a strain of 200% (Figure 3b). In addition, an elastic conductor was deposited on a biocompatible skin-like patch containing a simple pressure sensor. This structure, consisting of a micro-structured gold electrode [15] and ink-based PEDOT electrode transferred on the hybrid substrate, is shown in Figure 3c. In the demonstration, we applied it to the fingers which bend the farthest. The conductor was fully stretched when the bent fingers adopted a circular form (Figure 3d); significantly, in this position, the pressure sensor remained fully operational. These results show that the produced sensor can be placed easily and comfortably on human skin due to the relatively low elastic modulus of the patch platform. As shown in Figure 3e, force was applied to the patch before and after movement of the fingers, indicating good reliability of the stretchable device in real time.

Conclusions

In this study, the superior stretchability of an Ag ink conductor on a hybrid low-modulus substrate consisting of a thin elastomer and hydrogel layers was demonstrated. The elastic conductor containing Ag flakes and the silicon-based rubber film could be stretched to a high elongation of 1780%, while the corresponding relative change in resistance amounted to 154. Hence, the highly stretchable Ag conductor was successfully integrated to the low-modulus hydrogel substrate through the coated thin elastomer film. This hybrid substrate could also be attached to human skin to ensure comfortable movement of the produced patch. We expect that the stretchable conductor on the hybrid substrate developed in this work can be used in various areas requiring low-modulus platforms, such as skin patch sensor networks and implantable bio-medical devices.

Note

This article and images are drawn from "Ultrastretchable Conductor Fabricated on Skin-Like Hydrogel-Elastomer Hybrid Substrates for Skin Electronics" in *Adv. Mater*. 2018; 30: 1800109.

References

[1] Kim DH, Lu N, Ma R, Kim YS, Kim RH, Wang S, Wu J, Won SM, Tao H, Islam A, Yu KJ, Kim TI, Chowdhury R, Ying M, Xu L, Li M, Chung HJ, Keum H, McCormick M, Liu P, Zhang YW, Omenetto FG, Huang Y, Coleman T, Rogers JA. *Science* 2011; 333: 838.

[2] Kaltenbrunner M, Sekitani T, Reeder J, Yokota T, Kuribara K, Tokuhara T, Drack M, Schwödiauer R, Graz I, Bauer-Gogonea S, Bauer S, Someya T. *Nature* 2013; 499: 458.

[3] Yu B, Kang SY, Akthakul A, Ramadurai N, Pilkenton M, Patel A, Nashat A, Anderson DG, Sakamoto FH, Gilchrest BA, Anderson RR, Langer R. *Nat. Mater*. 2016; 15: 911.

[4] Bandodkar AJ, Nuñez-Flores R, Jia W, Wang J. *Adv. Mater*. 2015; 27: 3060.

[5] Lee H, Choi TK, Lee YB, Cho HR, Ghaffari R, Wang L, Choi HJ, Chung TD, Lu N, Hyeon T, Choi SH, Kim DH. *Nat. Nanotechnol*. 2016; 11: 566.

[6] Bihar E, Roberts T, Saadaoui M, Hervé T, Graaf JBD, Malliaras GG. *Adv. Healthcare Mater*. 2017; 6: 1601167.

[7] Huang X, Liu Y, Cheng H, Shin WJ, Fan JA, Liu Z, Lu CJ, Kong GW, Chen K, Patnaik D, Lee SH, Ali SH, Hwang Y, Rogers JA. *Adv. Funct. Mater*. 2014; 24: 3846.

[8] Hammock ML, Chortos A, Tee BCK, Tok JBH, Bao Z. *Adv. Mater*. 2013; 25: 5997.

[9] Pan L, Chortos A, Yu G, Wang Y, Isaacson S, Allen R, Shi Y, Dauskardt R, Bao Z. *Nat. Commun*. 2014; 5: 3982.

[10] Araki T, Nogi M, Suganuma K, Kogure M, Kirihara O. *IEEE Electron Device Lett*. 2011; 32: 1424.

[11] Kim Y, Zhu J, Yeom B, Prima MD, Kim JG, Yoo SJ, Uher C, Kotov NA. *Nature* 2013; 500: 59.

[12] Matsuhisa N, Inoue D, Zalar P, Jin H, Matsuba Y, Itoh A, Yokoda T, Hashizume D, Someya T. *Nat. Mater*. 2017; 16: 834.

[13] Sun JY, Zhao X, Illeperuma WRK, Chaudhuri O, Oh KH, Mooney DJ, Vlassak JJ, Suo Z. *Nature* 2012; 489: 133.

[14] Perelaer J, Abbel R, Wünscher S, Jani R, Lammeren T, Schubert US. *Adv. Mater*. 2012; 24: 2620.

[15] Mannsfeld SCB, Tee BCK, Stoltenberg RM, Chen CVHH, Barman S, Muir BVO, Sokolov AN, Reese C, Bao Z. *Nat. Mater*. 2010; 9: 859.

Eun Joo SONG
Principal Researcher
Molecular Recognition
Research Center
Materials and Life Science
Research Division

ejsong@kist.re.kr

USP35 regulates mitotic progression by modulating the stability of Aurora B

February 2018 / *Nature Communications* / Vol. 9 / 688

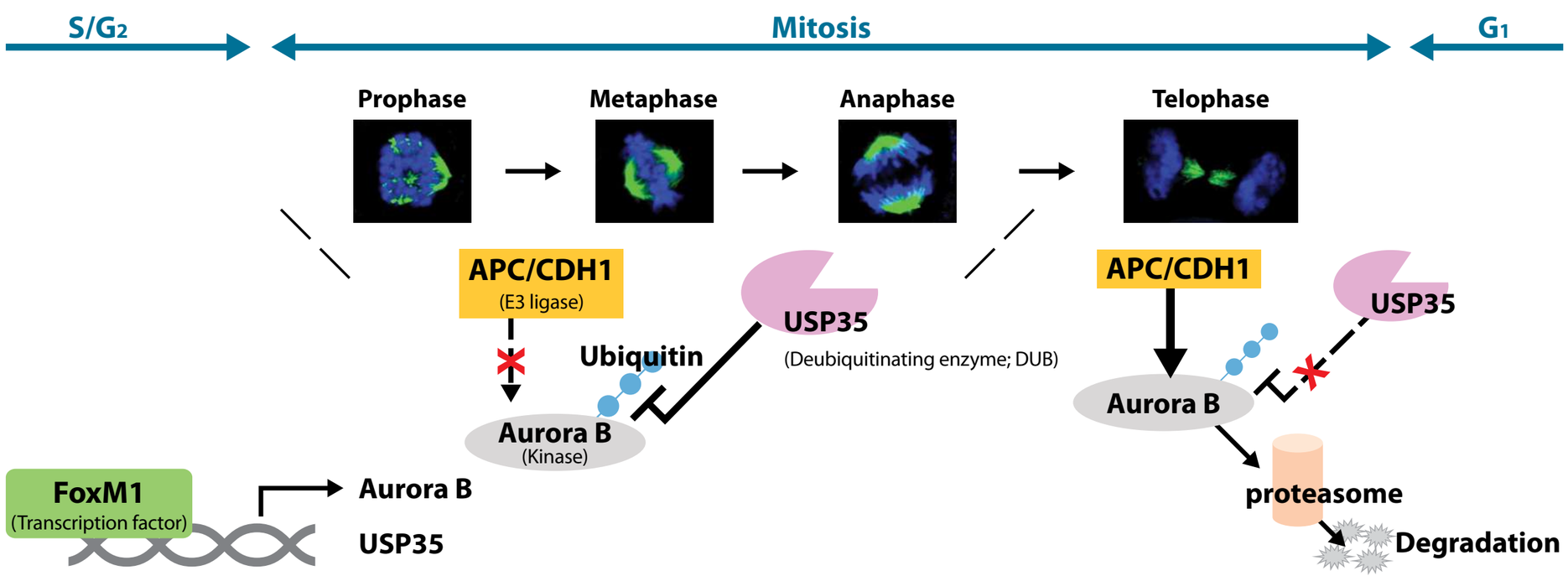

Although approximately 100 deubiquitinating enzymes (DUBs) are encoded in the human genome, very little is known about the DUBs that function in mitosis. Here, we demonstrate that DUB USP35 functions as a mitotic regulator by controlling the protein levels and downstream signaling of Aurora B and the depletion of USP35 eventually leads to several mitotic defects including cytokinesis failures. USP35 binds to and deubiquitinates Aurora B, and inhibits the APCCDH1-mediated proteasomal degradation of Aurora B, thus maintaining its steady-state levels during mitosis. In addition, the loss of USP35 decreases the phosphorylation of histone H3-Ser10, an Aurora B substrate. Finally, the transcription factor FoxM1 promotes the expression of USP35 as well as that of Aurora B during the cell cycle. Our findings suggest that USP35 regulates the stability and function of Aurora B by blocking APCCDH1-induced proteasomal degradation, thereby controlling mitotic progression

Technical Review

Ga-In Eutectic Liquid Metal-Air Batteries

Joong Kee LEE
Principal Researcher
Center for Energy Storage Research
Green City Technology Institute

leejk@kist.re.kr

Introduction

The rapidly expanding markets for wearable electronics and soft robots are prompting the development of soft, flexible and elastic energy devices. Unfortunately, neither the flexibility nor the stretchability characteristics of current energy devices satisfy actual demand at this point, mainly because the materials used for electrodes are hard [1, 2]. Meanwhile, softness is becoming a new and important property in next-generation energy devices, but research into soft energy devices is still in its infancy.

Compared to liquid phase materials, the solid state of current electrode materials limits the development of completely flexible and stretchable energy devices. However, currently available liquid metal batteries require high temperatures, such as Li//Sb–Pb liquid metal batteries (which operate at a temperature of 450°C) [3] and Mg//Sb liquid metal batteries (which work at 700°C) [4], making them unsuitable for use as energy devices for wearable electronic devices or soft robots at room temperature.

By using Ga-In alloy with a mass ratio of 9:1 as a flexible and elastic anode material (Figure 1), we have been able to create a soft, flexible, elastic and room-temperature liquid metal-air battery due to the liquid state of Ga-In alloy at room temperature.

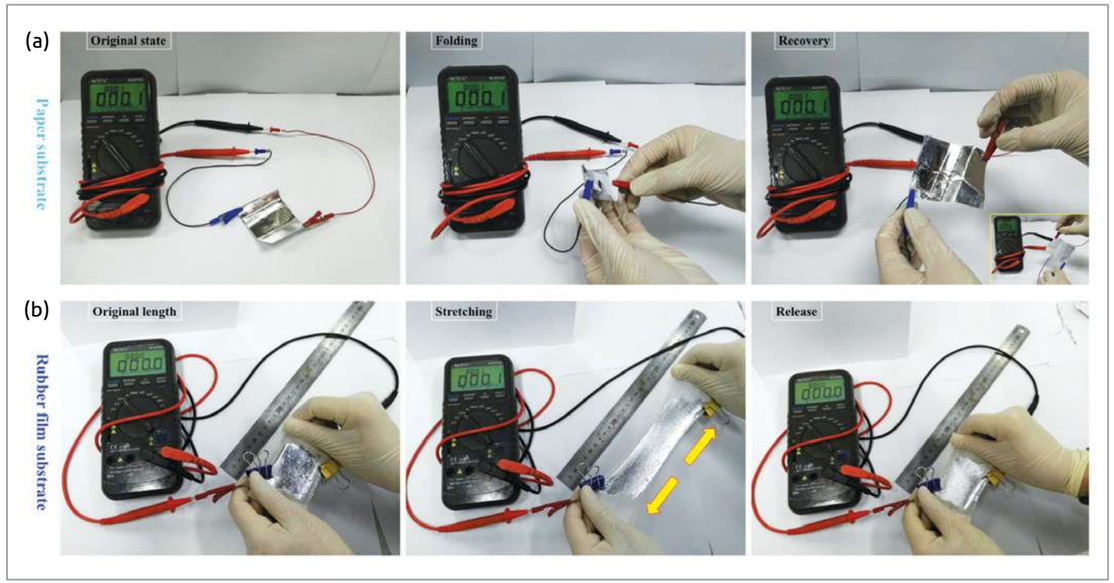

Figure 1 Good conductivities of the (a) paper- and (b) rubber film-supported liquid metal at various bending and stretching states, respectively.

Results and discussion

Fabrication

As exhibited in Figure 2, the assembly process for large-scale production of a liquid metal–air battery is simple. In our demonstration, a piece of nylon stocking material was immersed in a mixed solution consisting of PA-based polymer precursor solution and a polymerization initiator to realize a stocking-supported gel electrolyte film. The resulting stocking-supported gel film was coiled into a cavity. Then a carbon fiber-based cathode was wrapped around the surface of the cannular cavity. Finally, a cable-shaped battery was obtained after injecting the liquid metal inside the battery cavity via a syringe and binding the two ends of the battery body with cotton threads to seal it.

Working mechanism of the Ga-based battery

As shown in Figure 3, the discharge current density of the liquid metal–air battery was slightly lower than that of the Ga–air battery, and the indium–air battery performed with almost no discharge. This reveals that the liquid metal–air battery is very similar to a Ga-air battery. Using only carbon fiber as the cathode, the liquid metal-air battery shows a power density as high as 0.265 mW cm−2 at 1.5 V, which is higher than a cable-type Zn-air battery [5, 6] and is comparable to a cable-type Al-air battery [7]. The excellent discharge performance demonstrates that the liquid metal-air battery is a new and promising metal–air battery at room temperature.

The effective discharge reactions in the liquid metal-air battery are, as exhibited in Figure 4, the electrochemical reactions of $Ga - 3e^- \rightarrow Ga^{3+}$ and $In - 3e^- + 3OH^- \rightarrow In(OH)_3$ in the anode, and the classically cathodic reaction of $O_2 + 2H_2O + 4e^- \rightarrow 4OH^-$. The adverse side reaction can be attributed to the corrosion of Ga in KOH solution ($2Ga + 6\ H_2O - 6e^- \rightarrow 2Ga^{3+} + 3H_2$). To overcome this phenomenon, the In component plays several important roles, not only in maintaining the liquid state of the anode, but also in inhibiting the corrosion of Ga with a high KOH concentration in the electrolyte due to its high hydrogen evolution over-potential. Before forming In(OH)3, the In in the liquid metal first changes to In^{3+} ions which can inhibit the corrosion of Ga via the displacement reaction: $Ga + In^{3+} \rightarrow Ga^{3+} + In$.

Unique properties of the liquid metal-air battery

In addition to its high discharge performance (power density of 0.265 mW cm^{-2} at 1.5 V at room temperature and

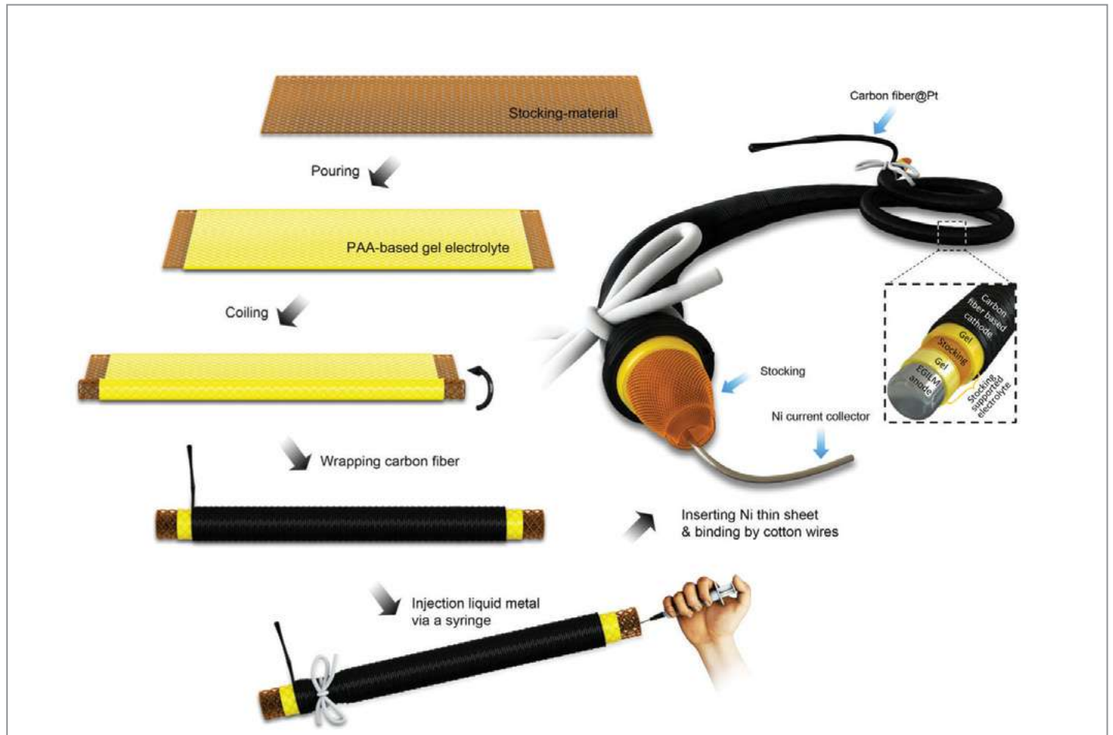

Figure 2 Maneuverable preparation process and internal structure of the cable-shaped eutectic gallium-indium liquid metal-air battery.

ambient atmosphere), four unique properties of the liquid metal-air battery were demonstrated. First, because it is in a liquid phase, the anode material can be injected with a syringe into the battery cavity, leading to its easy renewal. The discharge current can thus be controlled by the amount of injected liquid metal (Figure 5a) or by finger pressure (pressure-responsive discharge currents, Figure 5b). At the same time, this cable-shaped liquid metal-air battery is a novel soft battery, possessing high flexibility with complete recoverability and excellent elasticity. Figure 5c shows that bending and recovery operations on this battery within a curvature radius range of 1 dm to 1 mm have almost no influence on the discharge current curve. Moreover, with the help of the elastic gel electrolyte film and stocking material, this battery exhibits high elasticity, including both high stretchability and excellent recoverability without discharge performance loss; the battery can be stretched by 100% yet easily recovers to its initial length (Figure 5d).

More importantly, this battery possesses excellent battery shape restorability after all of the pressing, bending, and stretching operations, owing to its soft form. It also exhibits excellent performance retention rates of 100.65% and 98.87% while stretched (by 100%) and after recovery, respectively, which are the highest retention rates reported thus far.

Clearly, both the elasticity and degree of deformation of this battery are limited by the substrate and gel electrolyte, rather than by the anode. Therefore, we propose that even more elastic and randomly deformable batteries based on liquid metal anodes, one example being a vent ball-type battery (Figure 6),

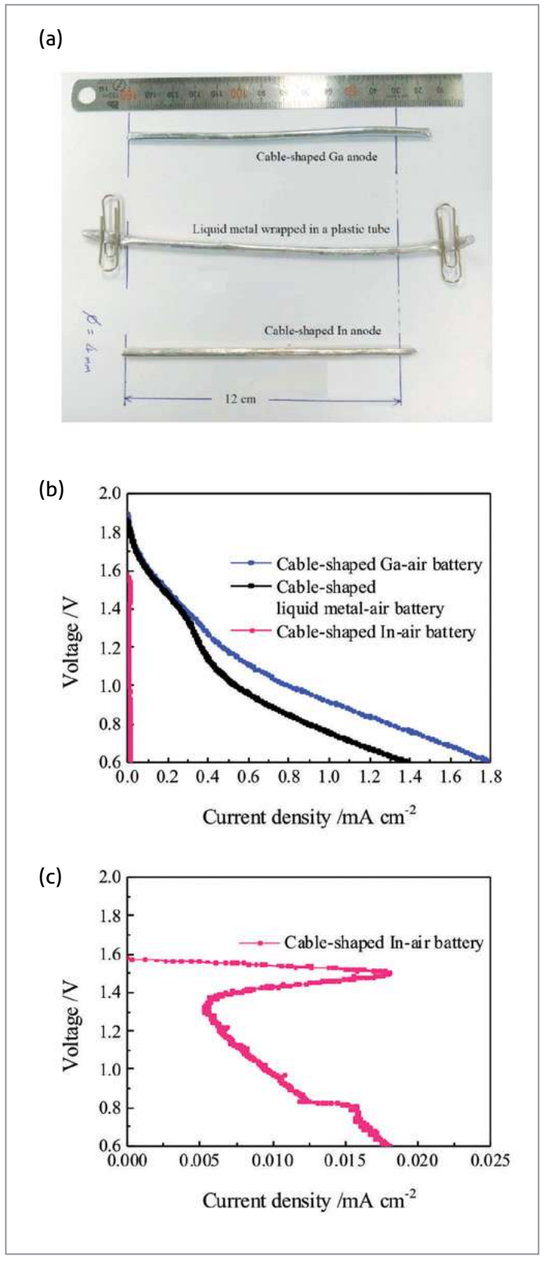

Figure 3 (a) Photos of the cable-shaped Ga, liquid metal, and In. (b, c) Polarization curves of the cable-shaped Ga-, liquid metal-, and In-air batteries.

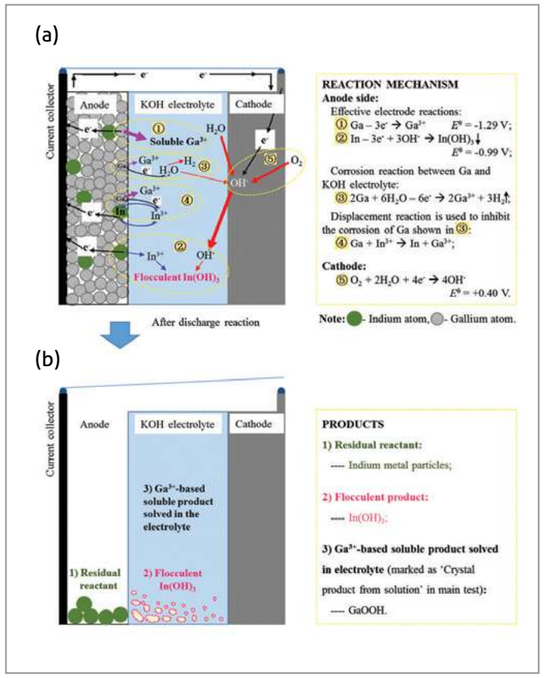

Figure 4 Sketch of (a) working mechanism and (b) products of the liquid metal-air battery.

can be achieved after further research to identify more suitable substrates and electrolytes.

Conclusions

In this study, a cable-shaped, soft, highly elastic liquid metal-air battery (with 9:1 of Ga-In mass ratio) with high performance (0.265 mW cm^{-2} at 1.5 V) at room temperature was designed with the effective anode reactions of $Ga - 3e^- \rightarrow Ga^{3+}$ (main reaction) and $In - 3e^- \rightarrow In^{3+}$, and $O_2 + 2H_2O + 4e^- \rightarrow 4OH^-$ in the cathode. Meanwhile, the In in the liquid metal anode served not only to form a liquid electrode with Ga at room temperature but also to prevent the corrosion of Ga in the KOH electrolyte as an inhibitor. Owing to the liquid anode, the anode can be easily renewed, and the discharge performance is

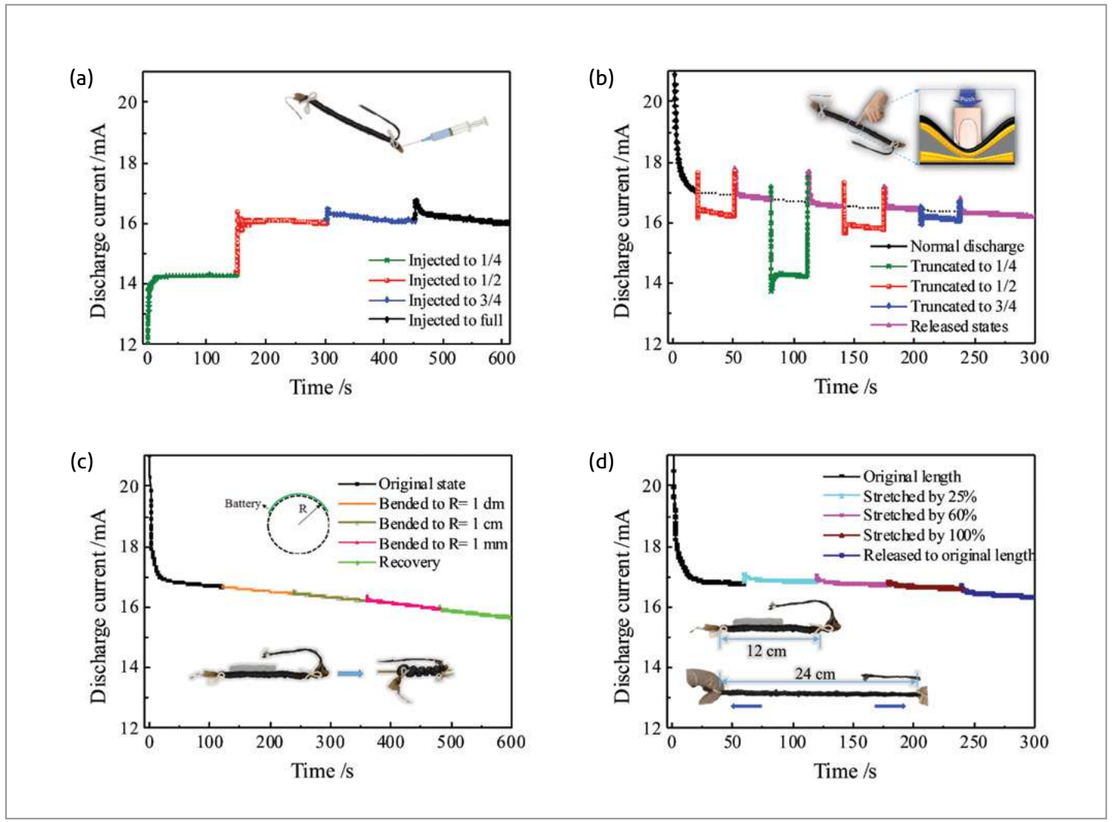

Figure 5 Unique functions of electrochemical performance of the eutectic Ga-In liquid metal-air battery. Discharge currents of the cable-shaped liquid metal-air battery with 12 cm of length and 8 mm of diameter at 1.2 V under different operations: (a) injecting liquid metal and (b) truncating the liquid metal anode to some scheduled lengths, (c) bending battery with a curvature radius from 1 dm to 1 mm, and (d) stretching battery from original length by 100%.

controllable by injecting different amounts of liquid metal or by truncating via a finger-squeeze. Moreover, the battery is highly flexible (bending radius <1 mm) and highly elastic (stretching by 100%) and recovers easily with negligible electrochemical performance impairment. Due to the liquid anode, the battery body exhibits a uniquely soft form and can change its shape with light pressure (for example, a finger). Our findings provide a new research direction in the field of wearable, soft energy devices: the development of deformable batteries based on the use of liquid metal materials.

Note

This article and images are drawn from "Soft, Highly Elastic, and Discharge-Current-Controllable Eutectic Gallium–Indium Liquid Metal–Air Battery Operated at Room Temperature" in *Advanced Energy Materials* 2018; 8: 1703652.

References

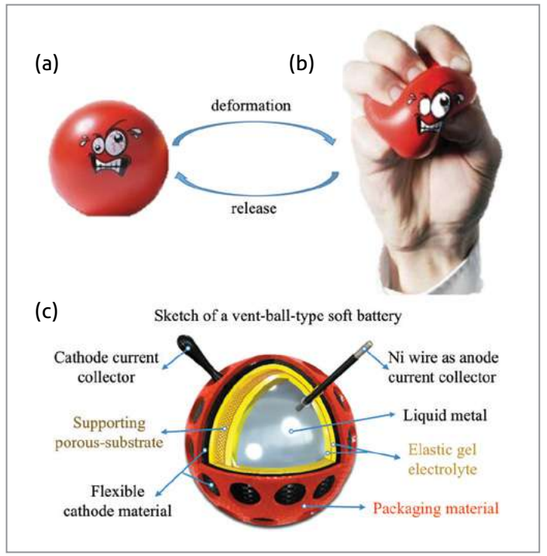

Figure 6 Schematic illustration of an ideal deformable battery based on a liquid metal anode (here as an example, a vent ball type). (a) and (b) photos of a vent ball-type battery before and after deformation; (c) sketch of a vent ball-type liquid metal-based soft battery.

[1] Liu G, Wang M, Wang H, Ardhi REA, Yu H, Zou D, Lee JK. *Nano Energy* 2018; 49: 95.
[2] Liu G, Gao X, Wang H, Kim AY, Zhao Z, Lee JK, Zou D. *J. Mater. Chem*. A 2016; 4: 5925.
[3] Wang K, Jiang K, Chung B, Ouchi T, Burke PJ, Boysen DA, Bradwell DJ, Kim H, Muecke U, Sadoway DR. *Nature* 2014; 514: 348.
[4] Bradwell DJ, Kim H, Sirk AHC, Sadoway DR. *J. Am. Chem*. Soc. 2012; 134: 1895.
[5] Park J, Park M, Nam G, Lee JS, Cho J. *Adv. Mater*. 2015; 27: 1396.
[6] Xu Y, Zhang Y, Guo Z, Ren J, Wang Y, Peng H. *Angew. Chem*., Int. Ed. 2015; 54: 15390.
[7] Xu Y, Zhao Y, Zhang Y, Ren J, Peng H. *Angew. Chem*., Int. Ed. 2016; 55: 7979.

Feature Articles

Biocompatible Silica Nanoparticles Conjugated with Azidocoumarin for Trace Level Detection and Visualization of Endogenous H_2S in PC3 cells

Kang Bong LEE
Principal Researcher
Green City Technology Institute
leekb@kist.re.kr

Yun Sik NAM
Principal Specialist
Advanced Analysis Center
ysnam@kist.re.kr

Introduction

H_2S (hydrogen sulfide) performs a number of biological signaling functions and is produced in small amounts by some cells in the mammalian body [1]. Since H_2S is a weak acid under normal physiological conditions, ~80% of it exists as mono anionic HS^-; the complex redox behavior of sulfur makes H_2S a highly reactive molecule in biological systems [2]. The biological concentrations of H_2S in the central nervous system and in blood plasma are in the range of 50–160 μM and 10–100 μM, respectively [3]. Abnormal H_2S levels are related to various diseases such as Down syndrome, diabetes, Alzheimer's, and liver cirrhosis [4-6].

Nowadays, H_2S fluorescent probes are receiving considerable attention owing to their high order of selectivity towards H_2S in the presence of other bio thiols and atmospheric molecules. As a result, biocompatible and more sensitive fluorescent probes for H_2S detection in live cells are in great demand. Similarly, silica nanoparticle-based probes have been extensively studied for use in drug delivery and bio-medical applications due to the unique surface-tailoring properties of these nanoparticles [7]. This article discusses a nanoprobe we developed which expresses turn-on fluorescence response based on the H_2S-mediated reduction of azide to amine. The lowest limit of detection (LOD) was 6 nM, even in the presence of a 1000-fold higher concentration of other biothiols. The nanoprobe was also applied for the detection of intracellular H_2S in PC3 (human prostate cancer) cells and could be applied by means of paper-type strips coated with the nanoprobe solution for H_2S detection. To our knowledge, this is the first report on the immobilization of the 7-azidocoumarin-4-aetci acid ($Cy\text{-}N_3$) moiety on silica nanoparticles (SiO_2NPs) for H_2S detection.

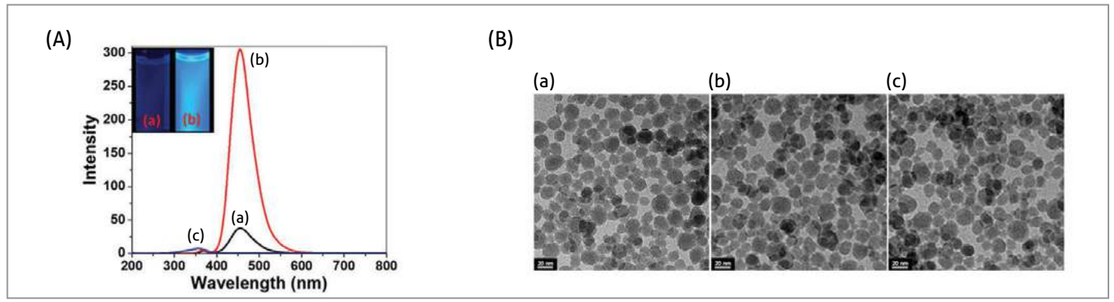

Figure 1 (A) Emission spectra and fluorescent photographic images under UV lamp obtained for (a) silica nanoprobe (λmax=456 nm), (b) after addition of 0.6 μM of H_2S with silica nanoprobe and its corresponding excitation (λmax=367 nm) in PBS (10 mM, pH 7.4). (B) TEM images obtained for (a) SiO_2NPs, (b) SiO_2NPs@$Cy\text{-}N_3$ and (c) SiO_2NPs@$Cy\text{-}N_3$ in the presence of H_2S.

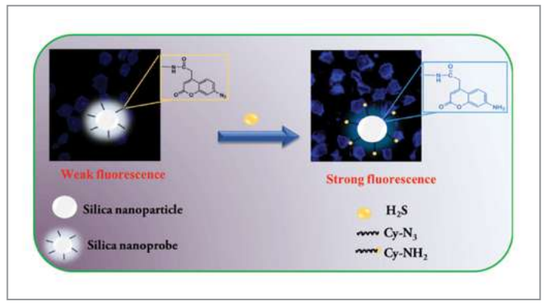

Scheme 1 Schematic illustration of H_2S detection using a silica nanoprobe conjugated with azidocoumarin.

Results

Preparation of the nanoprobe functionalized with $Cy\text{-}N_3$ and response to H_2S

The acid $Cy\text{-}N_3$ was synthesized by diazotization and successive sodium azide displacement reaction on $Cy\text{-}NH_2$ as described in an earlier report [8]. The SiO_2NPs were tailored with $Cy\text{-}N_3$ by a simple coupling reaction between the amine on SiO_2NPs and $Cy\text{-}N_3$. The ability of the silica nanoprobe conjugated with an azidocourmarin (SiO_2NPs@$Cy\text{-}N_3$) probe to detect H_2S was studied in PBS (10 mM, pH 7.4), (Figure 1A). The SiO_2NPs@$Cy\text{-}N_3$ probe expressed an emission peak at 456 nm with corresponding excitation at 367 nm. The emission peak intensity of the probe increased significantly upon H_2S addition due to the electron-withdrawing azide in the weakly fluorescent SiO_2NPs@$Cy\text{-}N_3$ (quantum yield, Φ=1.6%) to highly fluorescent amine (Φ=69%). H_2S is likely to be in the form of HS^- under physiological conditions, and HS^-, due to its high nucleophilicity, is one of the required active species for the reduction of azide into amine. The azide in SiO_2NPs@$Cy\text{-}N_3$ is the specific fluorogenic marker for H_2S, since the weak fluorophore, SiO_2NPs@$Cy\text{-}N_3$, is changed to a strong light blue one owing to the formation of highly fluorescent SiO_2NPs@$Cy\text{-}NH_2$ in the presence of H_2S (Scheme 1). The distinct fluorescent color change makes it easier to visualize the presence of H_2S (Inset in Figure 1A).

The size and morphology of the SiO_2NPs, SiO_2NPs@$Cy\text{-}N_3$, and SiO_2NPs@$Cy\text{-}N_3$ in the presence of H_2S (SiO_2NPs@$Cy\text{-}NH_2$) were examined with TEM (Figure 1B). TEM images revealed that both SiO_2NPs and SiO_2NPs@$Cy\text{-}N_3$ had a similar morphology averaging ~17 nm in size and were well dispersed (Figure 1B). Since a monolayer of $Cy\text{-}N_3$ was attached covalently through an amide NH on the surface of SiO_2NPs, the sizes of the SiO_2NPs and SiO_2NPs@$Cy\text{-}N_3$ were nearly the same (Figure 1B(a) and 1B(b)). The TEM image of SiO_2NPs@$Cy\text{-}NH_2$ formed after reaction with H_2S also showed a similar structure (Figure 1B(c)) The increase in fluorescent intensity upon addition of H_2S to SiO_2NPs@$Cy\text{-}N_3$ was reasonably attributed to the unique H_2S-mediated reduction of azide into amine (Scheme 1), and the formed SiO_2NPs@$Cy\text{-}NH_2$ did not show any agglomerated structure. Figure 2 shows ^1H NMR spectra for SiO_2NPs@$Cy\text{-}N_3$ upon addition of 0, 1, 3 and 5 equivalents of H_2S dissolved in DMSO-d_6. ^1H NMR chemical shifts for the benzene ring protons of SiO_2NPs@$Cy\text{-}N_3$ were assigned to δ 7.13, 7.16, and 7.78 ppm, and 2-pyrone protons of $Cy\text{-}N_3$ resonated at δ 6.34 ppm (Figure 2a). After addition

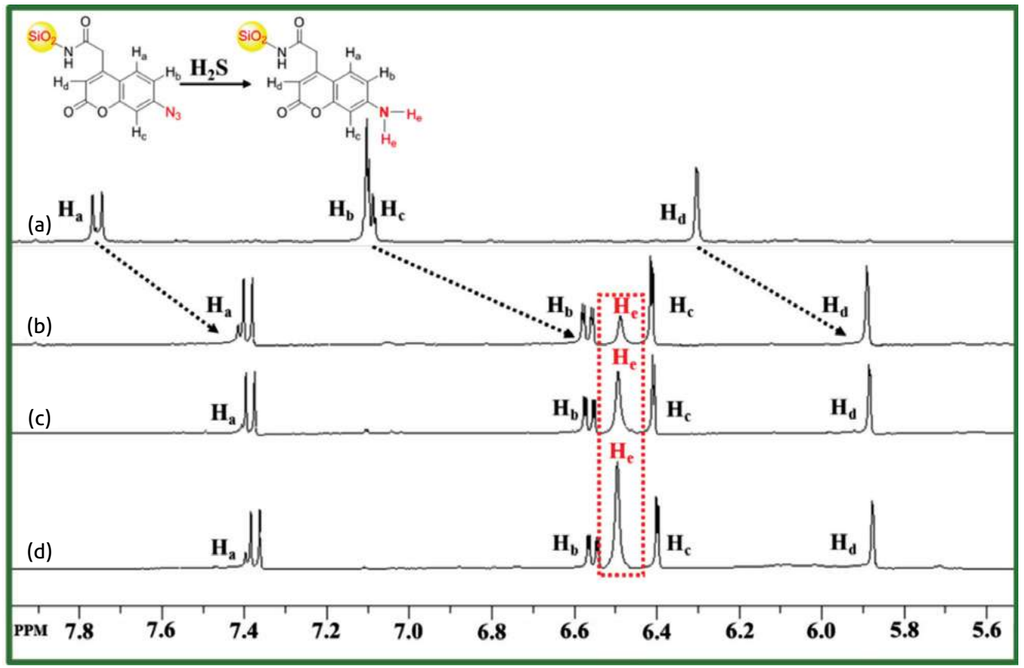

Figure 2 400 MHz ^{1}H NMR spectra of silica nanoprobe in the presence of (a) 0 equiv. H_2S, (b) 1 equiv. H_2S, (c) 3 equiv. H_2S, and (d) 5 equiv. H_2S in DMSO-d_6.

of 1.0 equivalent of H_2S to SiO_2NPs@Cy-N_3, the typical NH_2 peak appeared newly as a broad singlet at δ 6.52 ppm and the benzene ring proton peaks showed an upfield shift to δ 6.48, 6.61, and 7.33 ppm. Moreover, 2-pyrone peaks also shifted upfield at δ 5.82 (Figure 2b). Furthermore, the intensity of the amine peak increased gradually upon H_2S addition to the nanoprobe (Figures 2c and 2d).

Sensitive, selective, and interference-free H_2S detection

To examine the sensitivity of the nanoprobe for H_2S detection, fluorescence emission intensity was monitored for SiO_2NPs@Cy-N_3 upon addition of various H_2S concentrations (0–1.4 μM) in PBS at pH 7.4. The fluorescent intensities increased linearly with an increase in H_2S concentration in the range of 0–1.4 μM. The linearity and the LOD were 0.9970 (inset of Figure 3) and 6 nM, respectively. Furthermore, the selectivity

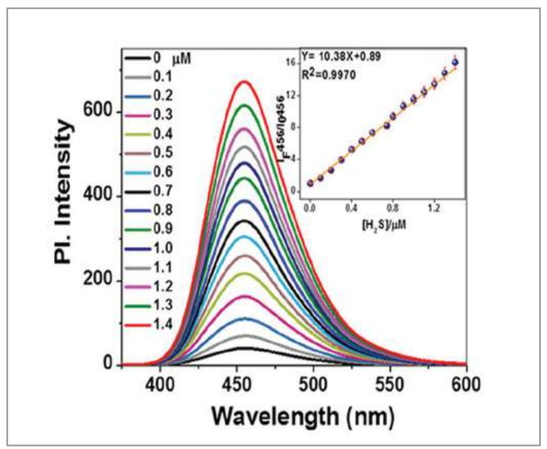

Figure 3 Fluorescence response of silica nanoprobe in PBS (10 mM, pH 7.4) with gradual increase in H_2S concentration (0–1.4 μM). Inset: plot of fluorescent intensity vs. H_2S concentrations.

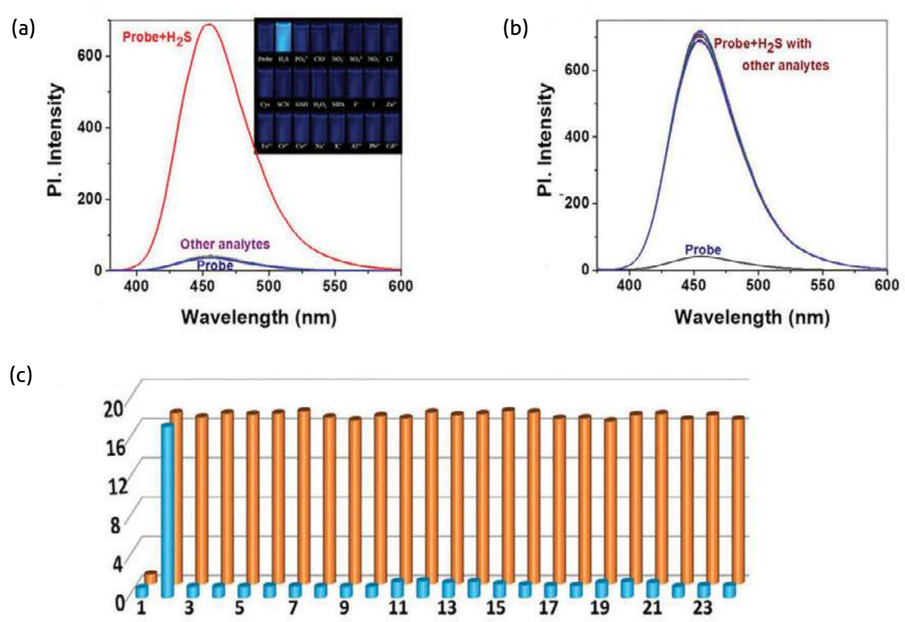

Figure 4 (a) Fluorescence responses of SiO_2NPs@Cy-N_3 in PBS (10 mM, pH 7.4) upon addition of (1) none (2) 1 μM H_2S, 1 mM each of (3) PO_4^{3-}, (4) ClO^-, (5) NO_2^-, (6) SO_4^{2-}, (7) NO_3^-, (8) Cl^-, (9) Cys, (10) SCN^-, (11) GSH, (12) Hcy, (13) MPA, (14) F^-, (15) I^-, (16) H_2O_2, (17) Fe^{3+}, (18) Cr^{3+}, (19) Cu^{2+}, (20) Na^+, (21) K^+, (22) Al^{3+}, (23) Pb^{2+} and (24) Cd^{2+}. (b) With addition of H_2S (1 μM) along with the above interfering ions. (c) Bar chart representation of selectivity (blue) and interference (yellow) effect of H_2S with the above analytes (1~ 24).

and interfering effect over various biothiols, metal cations, and anions for H_2S detection using the nanoprobe were tested. The fluorescence spectra of the nanoprobe upon addition of 1 μM H_2S and 1 mM of other biothiols (or ions) were taken for these tests. Only H_2S was found to induce a dramatic increase in the fluorescence intensity in comparison to those induced by other biothiols (Figure 4a). Moreover, H_2S detection was not affected even in the presence of a 1000-fold excess of other biological thiols, metal ions and anions (Figure 4b). Therefore, it was concluded that the nanoprobe detects H_2S even in the presence of a 1000-fold excess of other ions without interference in a highly sensitive manner (Figure 4c).

H_2S detection in cell lines

Our nanoprobe showed excellent sensitivity of nanomolar levels for H_2S detection, which is well below endogenous H_2S levels. Thus, it is definitely possible to trace H_2S in cell lines using our nanoprobe. The MTT assay also revealed that this nanoprobe has low cytotoxicity, and that it can behave as an excellent bioimaging reagent. In contrast to the fluorescent images of PC3 cells in the absence of the probe (Figure 5a), the images of PC3 cells with the probe showed a weak blue fluorescence (Figure 5b). However, a strong blue fluorescent signal was observed for PC3 cells pretreated with H_2S and stained with the probe (Figure 5c). The confocal images showed a distinct fluorescent signal change in the absence and presence of H_2S. This result indicated that our current probe can be applied for use as an intracellular imaging agent for H_2S in living cells.

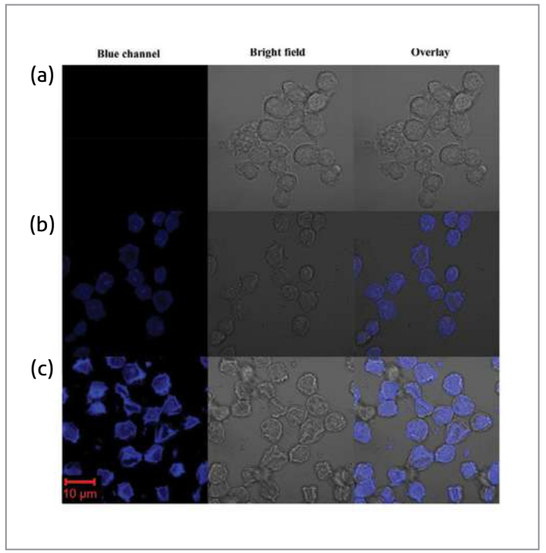

Figure 5 Confocal fluorescence microscopy images of PC3 cells: (a) PC3 cells only, (b) PC3 cells incubated with probe and (c) PC3 cells incubated with 5 μM of H_2S and probe. Scale bar = 10 μm (blue channel of 'c').

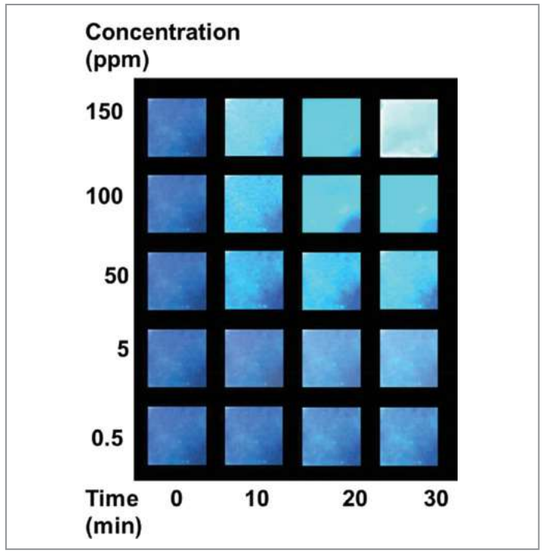

Figure 6 Visual detection of gaseous H_2S at various concentrations (0.5–150 ppm) from bottom to top. The fluorescence images were taken at 10, 20, and 30 min after exposure to H_2S gas under UV lamp with excitation at 365 nm.

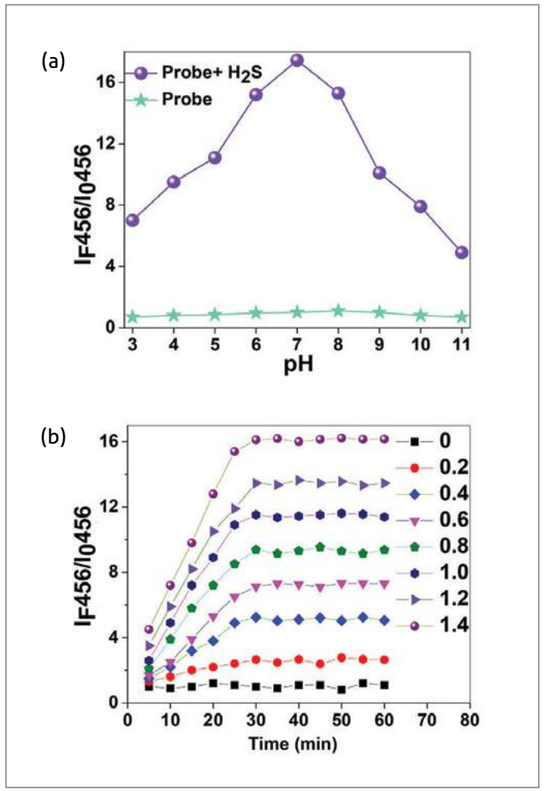

Figure 7 (a) Fluorescence response of the silica nanoprobe at different pH values (3–11) in PBS (10 mM, pH 7.4) and after addition of 1.5 μM of H_2S. (b) The increment in fluorescence intensity ratio against reaction time (0–60 min) after addition of different H_2S concentrations (0–1.4 μM). (λexcit=367, λemis=456).

Portable paper strip sensor for H_2S gas detection

H_2S gas is quickly converted to SH− under ambient conditions, and gaseous H_2S species can be monitored in such environments. To test gaseous H_2S detection, a Whatman sensing paper was coated with the nanoprobe solution. These indicator paper strips were then exposed to various concentrations of H_2S gas (0.02, 0.2, 2, 4 and 6 mM) for 0, 10, 20, and 30 min and were illuminated using a UV lamp. Their fluorescent images are shown in Figure 6. The collective images showed our nanoprobe successfully detected H_2S gas (Figure 6), and 5 ppm seemed to be the lowest detection level for the nanoprobe. This response of the nanoprobe implied its usability for environmental applications.

Optimum conditions for the nanoprobe

The fluorescent behavior and sensitivity of the nanoprobe were examined as a function of pH for H_2S detection. The fluorescence emission intensities at 456 nm for the nanoprobe under various pH conditions (3–11) did not show any significant changes in the absence of H_2S (Figure 7a). After the probe was reacted with 1 μM of H_2S, the fluorescent intensity was enhanced, and the maximum signal was attained at pH 7. Hence, the physiological pH of 7.4 was selected for further sensing and bioimaging purposes. In addition, the life span stability of the nanoprobe at pH 7.4 was examined; this stability test is needed as a pre-step verification for long-term imaging applications. The current probe expressed high stability over 60 min under physiological conditions (Figure 7b). The dose-dependent fluorescent kinetics were also monitored at various H_2S concentrations for the nanoprobe in PBS at pH 7.4 (Figure 7b), and the fluorescent intensity at 456 nm increased with increasing time and H_2S concentration. The intensity increased steeply at the beginning and then showed the highest plateau after 25 min. Thus, a 30 min incubation time of H_2S with the probe was selected as optimum for conducting experiments.

Conclusions

A novel SiO_2NPs@Cy-N_3 probe was developed for sensitive H_2S detection. This probe was also shown to have no heavy metal toxicity, but had environmental and biological applicability and high stability. The sensing strategy was found to involve H_2S-mediated reduction of azide into amine, which was confirmed by ^{1}H NMR studies. The nanoprobe gave selective turn-on response for only H_2S even in the presence of a 1000-fold excess of other biological thiols (Cys, Hcy, GSH, and SCN), metal ions, and anions. The nanoprobe also successfully detected H_2S in the gaseous form, which was indicated by fluorescent color change in Whatman paper. Since our nanoprobe showed the lowest LOD of 6 nM (6 nM is well below endogenous H_2S levels) and low cytotoxicity, we then successfully utilized it to trace H_2S in PC3 cell lines. The excellent selectivity, sensitivity, low cytotoxicity, and simple synthesis route of our developed silica nanoprobe make it extremely useful in H_2S-sensing studies.

Note

This article and images are drawn from "Biocompatible silica nanoparticles conjugated with azidocoumarin for trace level detection and visualization of endogenous H_2S in PC3 cells" in *Sensors and Actuators B*, 2018; Vol. 259: 307-315.

References

[1] Szabo C. *Nat. Rev. Drug Discov*. 2007; 6(11): 917–35.
[2] Henthorn HA, Pluth MD. *J. Am. Chem. Soc*. 2015; 137(48): 15330–6.
[3] Papapetropoulos A, Pyriochou A, Altaany Z, Yang G, Marazioti A, Zhou Z, Jeschke MG, Branski LK, Herndon DN, Wang R, Szabo C. *Proc. Nat. Acad. Sci. U.S.A*. 2009; 106(51): 21972–7.
[4] Han Y, Qin J, Chang X, Yang Z, Du J. *Cell. Mol. Neurobiol*. 2006; 26(1) 101–7.
[5] Kamoun P, Belardinelli MC, Chabli A, Lallouchi K, Vekemans BC. *Am. J. Med. Genet. A* 2002; 116A(3): 310–1.
[6] Eto K, Asada T, Arima K, Makifuchi T, Kimura H. *Biochem. Biophys. Res. Commun*. 2002; 293(5): 1485–8.
[7] Yang Y, Wan J, Niu Y, Gu Z, Zhang J, Yu M, Yu C. *Chem. Mater*. 2016; 28(24): 9008–16.
[8] Yan Y, Yu H, Zhang Y, Zhang K, Zhu H, Yu T, Jiang H, Wang S. *ACS Appl. Mater. Interfaces* 2015; 7(6): 3547–53.

Jong Hyun JANG
Principal Researcher
Fuel Cell Research Center
National Agenda Research Division

jhjang@kist.re.kr

Electrodeposited IrO_2/Ti electrodes as durable and cost-effective anodes in high-temperature polymer-membrane-electrolyte water electrolyzers

June 2018 / *Applied Catalysis B: Environmental* / Vol. 226 / pp. 289-294

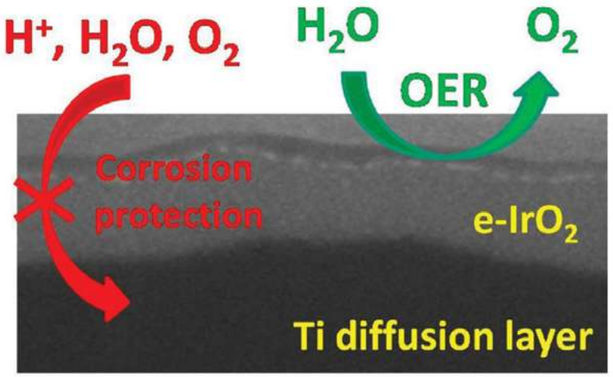

In this study, IrO_2-coated Ti mesh (e-IrO_2/Ti) is proposed to be an efficient and durable oxygen electrode for high-temperature polymer-membrane-electrolyte water electrolyzers (HT-PEMWEs). A thin IrO_2 film of submicron thickness was uniformly coated onto a porous Ti mesh substrate by anodic electrodeposition.

The electrodeposited IrO_2 film plays a dual role of a catalyst layer for the oxygen evolution reaction (OER) and a corrosion-protection layer that prevents oxidation of the inner Ti. The e-IrO_2/Ti exhibited high performance (0.97 A cm^{-2} at 1.6 V) despite a low IrO_2 loading (0.4 mg cm^{-2}) in single-cell tests conducted at 120°C, which is comparable to that of conventional electrodes with greater catalyst loadings (0.8–5 mg cm^{-2}).

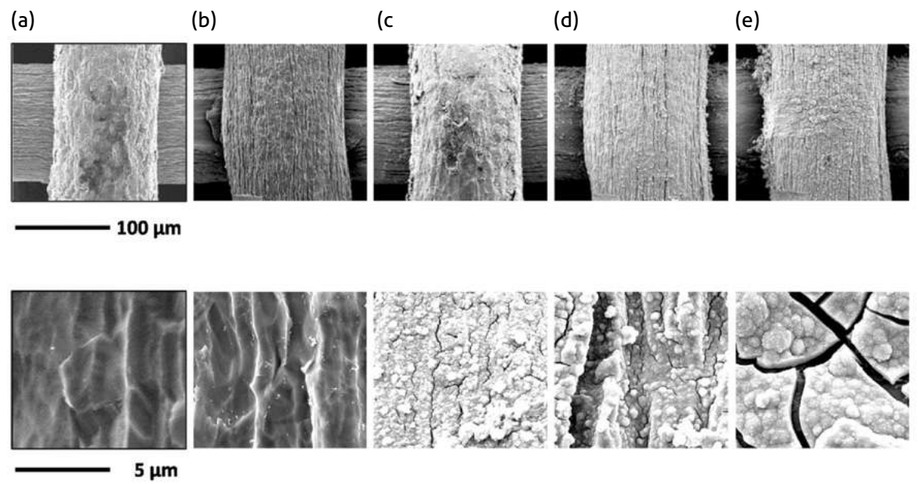

Time evolution of e-IrO_2/Ti morphology. Electrodes were prepared by controlling time to: (a) 1, (b) 3, (c) 5, (d) 10, and (e) 20 min at a fixed E_{dep} of 0.7 V_{SCE}.

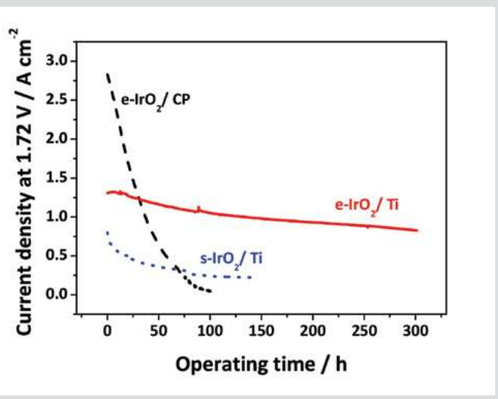

Furthermore, corrosion polarization tests reveal that the IrO_2 coating physically blocks exposure of the Ti diffusion layer, thereby reducing Ti corrosion by 82% in 0.5 M H_2SO_4 at 25°C. The low degradation rate (1.5 mA cm^{-2} h^{-1} (0.11% h^{-1})) obtained in aging experiments at 120°C and 1.72 V (voltage efficiency of 85%) confirms the excellent stability of this electrode.

Thrombin-activatable fluorescent peptide incorporated gold nanoparticles for dual optical/computed tomography thrombus imaging

January 2018 / Biomaterials / Vol. 150 / 125-136

Sung Pil KWON, Sang Min JEON, Sung Hoon LEE, Hong Yeol YOON, Ju Hee RYU, Da Yil CHOI, Jeong Yeon KIM, Ji Won KIM, Jae Hyung PARK, Dong Eog KIM, Ick Chan KWON, Kwang Meyung KIM, Cheol Hee AHN

kim@kist.re.kr

Thrombosis is an important pathophysiologic phenomenon in various cardiovascular diseases, which can lead to oxygen deprivation and infarction of tissues by generation of a thrombus. Thus, direct thrombus imaging is beneficial for the diagnosis and therapy of thrombosis. Herein, we developed thrombin-activatable fluorescent peptide (TAP) incorporated silica-coated gold nanoparticles (TAP-SiO_2@AuNPs) for direct imaging of thrombus by dual near-infrared fluorescence (NIRF) and micro-computed tomography (micro-CT) imaging, wherein TAP molecules were used as targeted thrombin-activatable peptide probes for thrombin-specific NIRF imaging. The freshly prepared TAP-SiO_2@AuNPs had an average diameter of 39.8 ± 2.55 nm and showed a quenched NIRF signal in aqueous conditions due to the excellent quenching effect of TAP molecules on the silica-gold nanoparticle surface. However, a 30.31-fold higher NIRF intensity was rapidly recovered in the presence of thrombin *in vitro*, due to the thrombin-specific cleavage of quenched TAP molecules on the gold particle surface. Furthermore, TAP-SiO_2@AuNPs were successfully accumulated in thrombus by their particle size-dependent capturing property, and they presented a potential X-ray absorption property in a dose-dependent manner. Finally, thrombotic lesion was clearly distinguished from peripheral tissues by dual NIRF/micro-CT imaging after intravenous injection of TAP-SiO_2@AuNPs in an *in situ* thrombotic mouse model, simultaneously. This study showed that thrombin-activatable fluorescent peptide incorporated silica-coated gold nanoparticles can potentially be used as a dual imaging probe for direct thrombus imaging and therapy in clinical applications.

Schaffer collateral inputs to CA1 excitatory and inhibitory neurons follow different connectivity rules

May 2018 / Journal of Neuroscience / Vol.38 / 5140-5152

O Sung KWON, Linqing Feng, Shaul Druckmann, Jin Hyun KIM

oskwon@kist.re.kr

Neural circuits, governed by a complex interplay between excitatory and inhibitory neurons, are the substrate for information processing, and the organization of synaptic connectivity in neural network is an important determinant of circuit function. Here, we analyzed the fine structure of connectivity in hippocampal CA1 excitatory and inhibitory neurons innervated by Schaffer collaterals (SCs) using mGRASP in male mice. Our previous study revealed spatially structured synaptic connectivity between CA3-CA1 pyramidal cells (PCs). Surprisingly, parvalbumin-positive interneurons (PVs) showed a significantly more random pattern spatial structure. Notably, application of Peters' Rule for synapse prediction by random overlap between axons and dendrites enhanced structured connectivity in PCs, but by contrast, made the connectivity pattern in PVs more random. In addition, PCs in a deep sublayer of striatum pyramidale appeared more highly structured than PCs in superficial layers, and little or no sublayer specificity was found in PVs. Our results show that CA1 excitatory PCs and inhibitory PVs innervated by the same SC inputs follow different connectivity rules. The different organizations of fine-scale structured connectivity in hippocampal excitatory and inhibitory neurons provide important insights into the development and functions of neural networks.

Understanding how neural circuits generate behavior is one of the central goals of neuroscience. An important component of this endeavor is the mapping of fine-scale connection patterns that underlie, and help us infer, signal processing in the brain. Here, using our recently developed synapse detection technology (mGRASP and neuTube), we provide detailed profiles of synaptic connectivity in excitatory (CA1 pyramidal) and inhibitory (CA1 parvalbumin-positive) neurons innervated by the same presynaptic inputs (CA3 Schaffer collaterals). Our results reveal that these two types of CA1 neurons follow different connectivity patterns. Our new evidence for differently structured connectivity at a fine scale in hippocampal excitatory and inhibitory neurons provides a better understanding of hippocampal networks and will guide future theoretical and experimental studies.

Ultrastrong Graphene–Copper Core–Shell Wires for High-Performance Electrical Cables

March 2018 / ACS Nano / Vol. 12 / 2803-2808

Sang Jin KIM, Dong Heon SHIN, Yong Seok CHOI, Ho Kyun Rho, Min PARK, Byung Joon MOON, Young Soo KIM, Seuoung-Ki LEE, Dong Su LEE, Tae Wook KIM, Sang Hyun LEE, Keun Soo KIM, Byung Hee HONG , Su Kang BAE

sbae@kist.re.kr

Recent advancements in mobile electronic devices and electric vehicles depend on electrical wires having reduced weight as well as enhanced stability. In addition, since electric energy is generated primarily at power plants located far from where the energy is consumed, there is a strong demand for mechanically stronger and higher-capacity electric power transmission cables. Unfortunately, these improvements have been held back because there have been no alternative materials developed that can practically replace copper materials. Here, we report a method to prepare ultrastrong graphene fibers (GFs)–Cu core–shell wires with significantly enhanced electrical and mechanical properties. The core GFs are synthesized by chemical vapor deposition, followed by electroplating of Cu shells, where the large surface area of GFs in contact with Cu maximizes the mechanical toughness of the core–shell wires. At the same time, the unique electrical and thermal characteristics of graphene allow a ~10 times higher current density limit, providing more efficient and reliable delivery of electrical energies through the GFs–Cu wires. We believe that our results suggest a way to improve electrical wires and cables, making them more useful for lightweight, energy-saving, and high-power applications.

Highly Secure Plasmonic Encryption Keys Combined with Upconversion Luminescence Nanocrystals

April 2018 / Advanced Functional Materials / Vol. 28

Ki Sun PARK, Min Ji PARK, Ho Seong JANG, Ji Hun PARK, Jae Kyun KIM, Young Hak CHO, Il Ki HAN, Dong Jin BYUN, Hyung Duk KO

kohd94@kist.re.kr

This study proposes a novel and highly secure encryption technology based on plasmonic-enhanced upconversion luminescence (UCL). The technology can be realized by a disordered plasmonic nanostructure composed of a transferred metal nanoparticle–UC nanocrystal (UCNC)–metal (tMUM) film using a graphene transfer process in which the metal nanoparticles that form on the graphene layer are transferred using Scotch tape. The plasmonic tMUM film strongly enhances the UCL by a factor of 200 mainly because of the excitation of the gap plasmon polaritons. Meanwhile, the UCNCs in direct contact with the metal film result in luminescence quenching caused by a nonradiative process. Herein, a highly secure anti-counterfeit film is developed, which is very hard to duplicate and cannot be reused, using two conflicting features (i.e., emission enhancement and quenching phenomena). The UCL is strongly amplified only when the first (i.e., a random metal nanoparticle array) and second (i.e., UCNCs on a Ag film) codes are very precisely overlapped as designed, thereby generating the originally designed final code. Therefore, our novel high-level security device is expected to be easily applied to protect and identify genuine products.

Aqueous-phase synthesis of metal hydroxide nanoplates and platinum/nickel hydroxide hybrid nanostructures and their enhanced electrocatalytic properties

June 2018 / Applied Catalysis B: Enviornmental / Vol. 225 / 238-242

Eui Young JUNG, Hee Young PARK, Ah Young CHO, Jong Hyun JANG, Hyun S PARK, Tae Kyung YU

hspark@kist.re.kr

We successfully synthesized metal hydroxide ($Ni(OH)_2$ and $Co(OH)_2$) nanoplates and platinum/nickel hydroxide hybrid nanostructures ($Pt/Ni(OH)_2$) in an aqueous solution. Transmission electron microscopy studies of the $Pt/Ni(OH)_2$hybrid nanostructures revealed that a number of 3 nm-sized Pt nanoparticles were well dispersed on the surface of each $Ni(OH)_2$ nanoplate. The $Pt/Ni(OH)_2$ hybrid nanostructures exhibited enhanced electrocatalytic properties due to the synergetic effect of $Ni(OH)_2$ and Pt.

Washable antimicrobial polyester/aluminum air filter with a high capture efficiency and low pressure drop

June 2018 / Journal of Hazardous Materials / Vol. 351 / 29-37

Dong Yun CHOI, Ki Joon HEO, Ju Hee KANG, Eun Jeong AN, Soo Ho JUNG, Byung Uk LEE, Hye Moon LEE, Jae Hee JUNG

jaehee@kist.re.kr

Here, we introduce a reusable bifunctional polyester/aluminum (PET/Al) air filter for the high efficiency simultaneous capture and inactivation of airborne microorganisms. Both bacteria of Escherichia coli and Staphylococcus epidermidis were collected on the PET/Al filter with a high efficiency rate (~99.99%) via the electrostatic interactions between the charged bacteria and fibers without sacrificing pressure drop. The PET/Al filter experienced a pressure drop approximately 10 times lower per thickness compared with a commercial high-efficiency particulate air filter. As the Al nanograins grew on the fibers, the antimicrobial activity against airborne E. coli and S. epidermidis improved to ~94.8% and ~96.9%, respectively, due to the reinforced hydrophobicity and surface roughness of the filter. Moreover, the capture and antimicrobial performances were stably maintained during a cyclic washing test of the PET/Al filter, indicative of its reusability. The PET/Al filter shows great potential for use in energy-efficient bioaerosol control systems suitable for indoor environments.

Quinoline derivatives for inhibiting histone methyltransferases and use thereof

US 15403404(2018.06.18.) KR 1020160179166(2016.12.26.)

Hyun Ah CHOO, Hoon RYU, Yoon Kyoung KIM, Yong Seo CHO, Ju Hyeon KIM

hchoo@kist.re.kr

Disclosed are quinoline derivatives which inhibit the activity of histone methyltransferases (ESET/SETDB1) specific for trimethylated H3K9 (H3K9Me3) or a pharmaceutically acceptable salt. Xenazine is the only drug for intractable neurodegenerative brain disease, Huntington's disease, and an inhibitor of VMAT2 which reduces dopamine in neurons. Xenazine can alleviate Chorea, but it cannot cure the causes of the disease. ESET (SETDB1) is over-expressed in patients with Huntington's disease, resulting in increase of H3K9 trimethylation, and ESET (SETDB1) is one of the novel targets for disease modifying therapy. A validated inhibitor of ESET (SETDB1) can reduce trimethylated H3K9 and ESET (SETDB1) inhibitors, quinoline derivatives, are potential drug candidates for Huntington's disease.

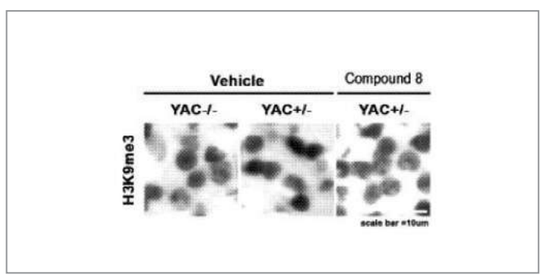

Apparatus and method for measuring electrocardiogram using wireless communication

US 9901272B2(2018.02.27) KR 101651537B1(2016.08.26)

In Chan YOUN, Kui Won CHOI, Jung Hwan KIM

iyoun@kist.re.kr

Disclosed is an apparatus for measuring electrocardiogram (ECG) using wireless communication, including a first measuring device and a second measuring device connected to each other using wireless communication, wherein the first measuring device includes a first electrode configured to measure a first signal generated by a heartbeat, and a slave signal generation unit configured to generate a slave signal based on the first signal and a wireless virtual ground signal received from the second measuring device, and the second measuring device includes a second electrode configured to measure a second signal generated by a heartbeat, a ground electrode configured to measure a ground signal, a wireless virtual ground unit configured to generate the wireless virtual ground signal based on the ground signal, and an ECG measuring unit configured to measure ECG based on the slave signal, the second signal, and the wireless virtual ground signal.

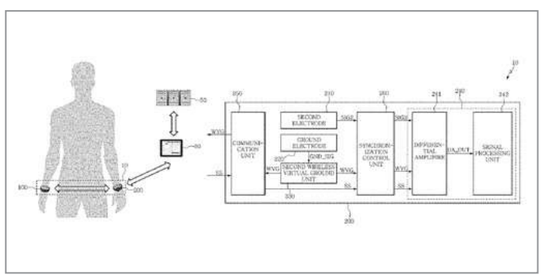

Drug carrier having L-DNA nanocage structure

US 9919001B2(2018.03.20.) KR 101494773B1(2015.02.23)

Dae Ro AHN

drahn@kist.re.kr

The present invention relates to a drug carrier having L-DNA nanocage structure prepared by using L-DNA, the mirror form of natural DNA, as a backbone. The drug carrier of the present invention has very superior cellular uptake efficiency and serum stability, so that it can be applied to deliver various drugs into cells effectively.

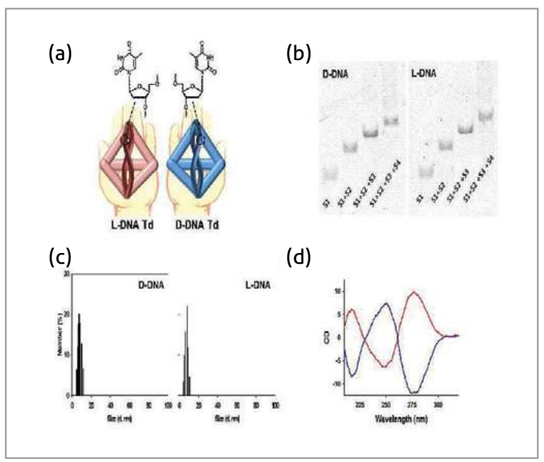

Apparatus and method providing augmented reality contents based on web information structure

US 9904664B2(2018.02.27) KR 101380854B1(2014.04.04)

Sang Chul AHN, Hee Dong Ko

asc@kist.re.kr

Herein is provided augmented reality content providing an apparatus based on a web information structure including: an HTML document that includes a URI setting unit setting a uniform resource identifier (URI) corresponding to a point of interest (POI); a POI processing unit collecting attribute information from a target terminal and identifying the POI by using the collected attribute information; a virtual object processing unit that matches a virtual object associated with the URI to the identified POI; and a 3D browser engine used for setting coordinates on the 3D physical space such that the POI and the virtual object are displayed in a 3D virtual space through a web browser of the target terminal, analyzing video information of the POI and the virtual object based on the set coordinates, and providing the target terminal the analyzed video information.

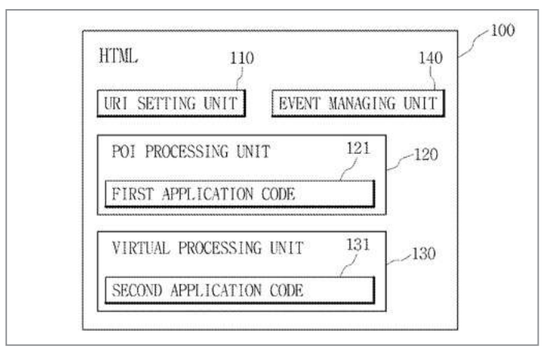

Wearable electromyogram sensor system

US 9999391B2(2018.06.19) KR 101501661B1(2015.03.12)

Kee Hoon KIM, Min Kyu KIM

khk@kist.re.kr

A wearable electromyogram sensor system is provided. The wearable electromyogram sensor system includes: an elastic band having a plurality of electrodes; an electromyogram sensor including an electrode connected to an electrode of the band so as to receive a bio-signal related to contraction of a muscle, and configured to sense change-of-motion information through the bio-signal or previously sense the change of the motion information before the motion information is changed; and a fixing unit fixing the electromyogram sensor to the band. The electrode of the electromyogram sensor is connected to an electrode at an arbitrary position of the band.

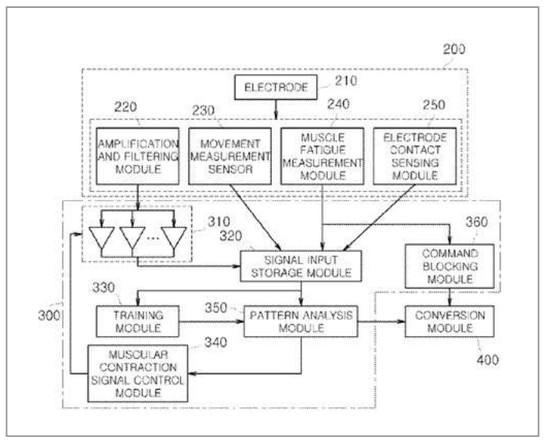

Carbon nanofibers with sharp tip ends and a carbon nanofibers growth method using a palladium catalyst

US 9970130B2(2018.05.15) KR 101626936B1(2018.06.02)

Myung Jong KIM, Dong Su LEE

myung@kist.re.kr

The present invention relates to a carbon nanofibers growth method including (S1) depositing an alumina layer on a silicon substrate, (S2) depositing palladium on the alumina layer to form a palladium catalyst layer, and (S3) growing carbon nanofibers on the palladium catalyst layer by a chemical vapor deposition (CVD) method, and carbon nanofibers vertically grown on an alumina layer-deposited silicon substrate, the carbon nanofibers having tip ends with a radius of curvature less than or equal to 5 nm, a diameter less than or equal to 50 nm, a length more than or equal to 1 mm, and a length-diameter aspect ratio more than or equal to 50,000.

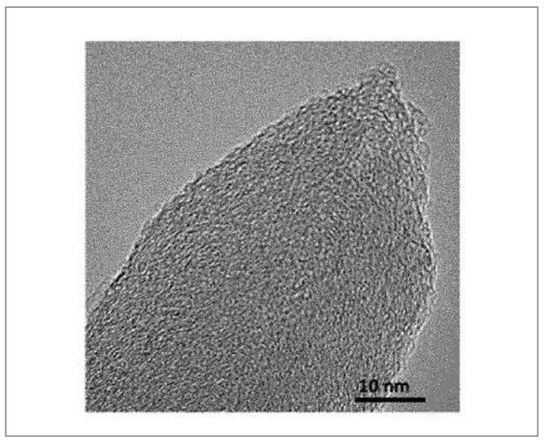

Science News

Planning for Inter-Korean S&T Cooperation

Ever since the inter-Korean and US-North Korean summit meetings, expectations have been rising for cooperation between the two Koreas. The South Korean government has designated information and communications technology (ICT) and science and technology (S&T) as the areas in which immediate economic benefits could best be achieved for both countries, believing that sustainable growth in North Korea will require a development and cooperation plan that covers all aspects of ICT, including technologies, industrial infrastructure, and support systems.

Based on a recent analysis of North Korea's ICT industry, the South Korean government intends to define and prioritize potential areas of cooperation, determine the scope of potential projects, and establish appropriate strategies for moving forward. The work will be a prelude to the establishment of an overall roadmap for ICT development, and South Korean S&T organizations are already involved in these efforts. The National Research Council of Science and Technology (NST) is reviewing proposals submitted by 25 government-funded institutions and is considering the establishment of an inter-Korean S&T cooperation center in which state-funded S&T institutions could participate.

Individual institutions are pushing ahead with plans for joint research projects. Transportation and social overhead capital are important areas for research, representing the first step in developing a new economic map for the Korean Peninsula. And since this map is expected to integrate the Northern railway system, the Korea Railroad Research Institute is busy conducting a policy research project known as the Northeast Asian Railway Community Initiative.

Research to assess the developmental needs of North Korea's deteriorated social infrastructure is gaining momentum as well. The Korea Institute of Civil Engineering and Building Technology has opened its Unification and Northern Research Center to analyze methods of building up North Korea's infrastructure. It also initiated research into technology for restoring and managing the Han and Imjin rivers in preparation for unification. This work ties into the development project for the Han River estuary located at the DMZ, a project stemming from the Inter-Korean declaration made on October 4, 2007.

ICT research exchanges and cooperation will begin in earnest during the second half of this year. Researchers cite Germany as the benchmark for building an inter-Korean communications network, and a special committee will be established to discuss issues related to communications frequencies, such as spillover, frequency technology, and standardization.

For its part, KIST is actively engaged in identifying initiatives on which the two Koreas can cooperate in preparation for unification. Confident that S&T can be used to help improve foreign relations, ensure national security, and encourage balanced regional development, KIST President Byung Gwon LEE stated, "Now that the two Koreas are embarking on collaborative projects, researchers in the field of S&T must also seek out ways to increase exchanges."

One of the natural plants on the Korean Peninsula, *Lycoris chejuensis*

KIST is particularly focused on joint research projects related to the approximately 1,000 natural products grown on the Korean Peninsula as a part of Korean tradition—products such as ginseng and Korean lacquer. Such projects can help improve the lives of North Koreans, especially in times of serious food shortages brought about by natural disasters (i.e. floods, droughts, etc.) or economic sanctions. According to Hak Cheol KWON, director of KIST's Natural Constituents Research Center, "Although North Korea was designated by the UN FAO as a food-shortage nation, it has sufficient demand and a favorable enough environment for medicinal farming. North Korea currently depends on China to source natural products, and China is marketing its Mt. Paektu ginseng to compete with the ginseng from Korea. If the two Koreas can cooperate in producing natural industrial products, the mutual benefits will be great." In hopes of conducting joint research on Mt. Paektu's natural products, KIST is planning to increase its collaborative research by signing a multilateral agreement with natural product/forestry/agriculture research centers in China and the two Koreas, and it is also considering establishing a joint survey center.

Although the two Koreas possess vastly different levels of technological expertise, goods, and resources, North Korea does have some comparative advantages when it comes to ICT. Therefore, continued cooperation will likely result in a North Korean S&T research center similar to KIST, an ICT research center similar to ETRI, and an industrialization support center through which both countries can exchange knowledge while co-developing cutting-edge technologies and advanced industries.

KIST News

KIST and Korea Yakult agree to cooperate on probiotic research

On April 4, KIST and Korea Yakult Co., Ltd. signed an agreement to establish a technology license and cooperate on research related to the role of Korea Yakult's lactobacillus "L casei HY2782" in fighting negative health effects associated with particulate matter pollution.

A KIST research team, using Korea Yakult's lactobacillus flora, found that the lactobacillus provided protection against the harmful effects of particulate matter. The new discovery was made by Dr. Kyung Su KANG's research team at the Systems Biotechnology Research Center at KIST Gangneung. The team announced its results after studying the toxicity of various harmful substances using the soil nematode C. elegans (*Environmental Toxicology*, 2017; Vol. 6). The growth and reproductive functions of the nematodes declined when injected with particulate matter, but the symptoms were significantly mitigated when the nematodes were fed with lactobacillus casei HY2782 flora. This finding raises hopes for creating a new market in the fermented dairy product industry.

Particulate matter has become a major health concern. When inhaled, it can cause various respiratory and cardiovascular diseases, and the World Health Organization has categorized it as a class one carcinogen. Particulate matter is also known to increase death rates. Identifying and restricting its underlying sources, using health-protecting items such as dust masks, and eating a balanced diet to strengthen the immune system are all helpful in addressing particulate matter pollution. Now KIST research offers an additional response to the problem.

KIST Gangneung Holds Smart Farm Technology Exhibition

On June 4, the KIST Gangneung Institute of Natural Products held an exhibition of core smart farm technologies developed by its Convergence Research Center for Smart Farm Solution.

The exhibition was accompanied by a technology demonstration, and attendees included Dr. Lee Jin-gyu, 1st vice minister of the Ministry of Science and ICT; Dr. Won Kwang-yeon, chairman of the National Research Council of Science and Technology; Dr. Byung Gwon LEE, president of the Korea Institute of Science and Technology (KIST); Dr. Yi Sung-il, president of the Korea Institute of Industrial Technology (KITECH); Dr. Kwak Byung-Sung, president of the Korea Institute of Energy Research (KIER); and Dr. Park Dong June, president of the Korea Food Research Institute (KFRI).

The Convergence Research Center for Smart Farm Solution, which is headquartered at KIST, was launched in October 2015 with funding from the Ministry of Science and ICT and the National Research Council of Science and Technology. The center exists thanks to the contributions of five government-funded research institutes; namely, KIST, the Electronics and Telecommunications Research Institute (ETRI), KITECH, KIER, and KFRI.

In addition, nine companies—including CultiLabs, a company based around KIST technology—participated in the event, adding to its impact.

The eight core technologies (which resulted in 18 more specified technologies) exhibited were: 1) new crop development measurement/analysis techniques, 2) smart irrigation based on complex physiological/environmental measurements, 3) circular sterilization/treatment of a nutrient solution for improved water conservation, 4) smart complex environmental controls, 5) smart greenhouse work controls, 6) optimal energy control, 7) smart farm information utilization, 8) and improved cultivation of functional crops used as food and drug-sources. These technologies are predicted to substantially enhance Korean agriculture and industry.

The Convergence Research Center for Smart Farm Solution transferred technologies worth a total of 1.2 billion KRW to six different companies, and it is establishing a hectare (ha; 10,000㎡)-sized smart farm in Dangjin to utilize waste heat from a nearby power station. Also, the center established and is currently operating smart farm testbeds in the cities of Pohang and Sejong, in an attempt to develop technologies that are immediately applicable to agricultural sites.

According to KIST President Byung Gwon LEE, "Technologies developed by the Center will be applied to domestic and foreign farms through Korea's smart farm companies, thus taking Korea's smart farm industry to a new level." Dr. Chu Won NHO, head of the Convergence Research Center, also noted, "We will work closely with the Ministry of Science and ICT, the Ministry of Agriculture, Food and Rural Affairs, and the Rural Development Administration through a smart farm cooperative R&D platform to develop technologies widely adopted by farms."

KOICA and KIST hold open workshop on VKIST Support Program

On September 6, KIST and the Korea International Cooperation Agency (KOICA), an agency dedicated to providing grants, hosted an open workshop on the Vietnam-Korea Institute of Science and Technology (VKIST) Support Program. The Support Program marks the largest S&T-related overseas development aid in Korean history. The event, funded by the Korean Federation of Science & Technology Societies, was organized as a briefing session bringing together relevant public agencies, research centers, and academia to review the success of the VKIST Support Program and discuss ways to ensure the sustained operation of VKIST.

At the workshop, KOICA President Mi Kyung LEE

emphasized that VKIST's success going forward should be based on a strategy of training researchers, building a platform for practical research, cooperating with industry and universities to utilize research outcomes, and attracting private sector funding.

In his congratulatory address, KIST President Byung Gwon LEE stated, "We will use KIST's know-how and technology built on Korea's economic development over the last 50 years to provide full support for the program." He added, "By successfully establishing VKIST with a vision toward inclusive growth, KIST will contribute to boosting Korea's national status."

The workshop consisted of three sessions. In session 1, Professor Soo Young CHANG of Pohang University of Science and Technology presented the current status and future vision of Korea's S&T overseas development aid program. In session 2, KIST's Seok Jin YOON, vice president and head of the VKIST Support Program, reviewed VKIST's progress and plans for its continued support, while VKIST President Dong Wha KUM outlined VKIST's phased expansion plans and operations roadmap. In session 3, experts in the fields of S&T, industry cooperation, and overseas development activities gathered to have an in-depth discussion on what VKIST's independent operation should look like after 2020 when the Support Program comes to an end.

The Support Program was initiated following an official request from the Vietnamese government to set up a research center modeled on KIST. Under the program, which lasts from 2014 to 2020 with a budget of USD 35 million, KIST and KOICA will cooperate with Vietnam's Ministry of Science and Technology to build the VKIST research complex, install research equipment, provide operational consulting, conduct joint research, train researchers, and provide operational support. The Vietnamese government is responsible for providing land for the research complex plus utilities, electricity, and telecommunications. VKIST is expected not only to advance Vietnam's economic development and competitiveness, but also to help increase technology transfers and business cooperation between Vietnamese and Korean companies.

The Hongneung area of Seoul to become a center of biomedical innovation

On May 29, KIST and member institutions of the Hongneung Forum gathered at KIST Seoul to launch the Hongneung Clustering Project Group whose purpose is to turn Hongneung into a center of biomedical innovation. Among the 50 attendees at the event were National Assembly member Seung Hee YOU, 1st Vice Minister Jin Gyu LEE of the Ministry of Science and ICT, and Hongneung Forum Chairman Myung Ja KIM, as well as the heads of member institutions.

The Hongneung Clustering Project Group comes from the Hongneung Forum, which was formed six years ago. At the time, five of Hongneung's public institutions were relocated, leading to concerns over the area hollowing out. Heads of institutions in Hongneung gathered and created a forum to discuss ways to utilize the empty space.

The Forum holds presentations and panel discussions on new topics related to Hongneung, such as "Hongneung's Role in the Fourth Industrial Revolution" and "The Cluster and Traffic Network". Around 200 participants join this biannual event.

Since its launch in 2012, the Forum has worked to develop the Hongneung Research Complex and identify appropriate areas for future national efforts in support of the biomedical industry. In 2017, the Forum announced a biomedical innovation cluster as Hongneung's future vision. To this end, KIST and the other member institutions will suggest ways for the various agencies involved in regional development policy, including the Ministry of Science and ICT, the Ministry of Land, Infrastructure and Transport, and the Seoul Metropolitan Government, to work together to unite Hongneung's 5,500 Ph.Ds into an integrated research community.

The Forum's Project Group is developing a new business-creating model that commercializes clinical research on a fast track by facilitating cooperation among universities, hospitals, research centers, and businesses. With this goal in mind, translational research projects participated in by KIST, Korea University Medical Center, Kyung Hee University Medical Center, and Seoul Bio Hub will be expanded. The Project Group also plans to build a testbed where experiments, clinical studies, and verifications can be conducted for the innovative technologies. It also plans to develop a public design for the Hongneung Cluster to create a unique identity and culture in the area.

Another main objective of the Hongneung Complex is to become a hub for startups and new jobs. The Project Group will encourage the creation of high-quality jobs by establishing a sophisticated system to support startups, such as by raising investment funds for Hongneung and jointly operating an organization for technology commercialization. There is a commitment to provide startups and venture capital companies with access to R&D facilities at universities and research centers with the ultimate goal of breaking down barriers between institutions and establishing a "one-campus" concept.

To this end, the Project Group is working for Hongneung to be named an "InnoTown" by the Ministry of Science and ICT and win designation as an Regeneration New Deal Project by the Ministry of Land, Infrastructure, and Transport. If named an InnoTown, Hongneung will benefit from regulatory sandbox status, R&DB commercialization support, and tax reduction. The Project Group is planning to apply for InnoTown designation next year.

Uncomfortable Yet Unavoidable Truth About Cancer

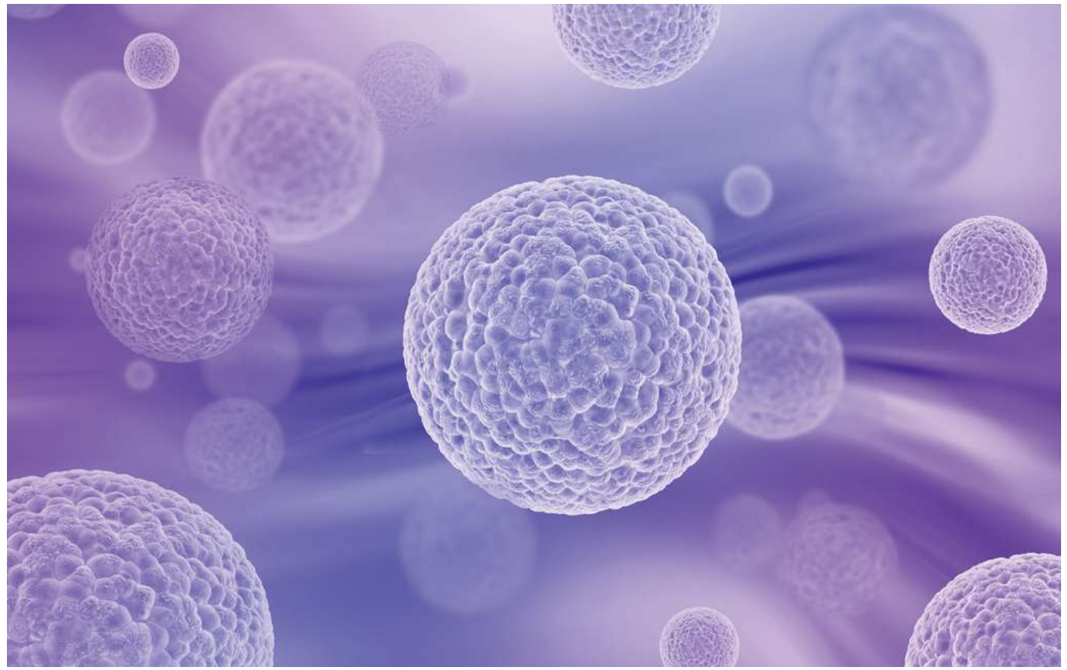

In San KIM
Principal Researcher
Center for Theragnosis
Biomedical Research Insitute

iskim14@kist.re.kr

In his State of the Union Address in 2016, then U.S. President Barack Obama announced another war on cancer. There was even an emotional moment when he assigned his vice president, Joe Biden, who had just lost his 47-year old son to a brain tumor, head of "mission control." Ever since Richard Nixon announced his administration's war on cancer and signed the National Cancer Act in 1971, America has led the global effort in developing remarkable technologies for treating cancer. Unfortunately, almost 50 years later, we are witnessing more and more people suffering from the illness.

Cancer is no longer someone else's business since one out of two people will ultimately be diagnosed with it. We find ourselves shocked when someone close has cancer, but if you think about it, having cancer is hardly surprising. A sperm and egg fertilize in a mother's womb to become a single cell. Over the next nine months, that cell becomes a human being with trillions of cells. It is astounding that one cell can multiply into that many cells in such a short period - and cancer cells are no different.

Despite such an active proliferating capacity, trillions of cells exist harmoniously with one another, which is a miracle indeed. In fact, we should be surprised to see our cells not turning into cancer cells or causing any trouble. In an era of longevity, we have to accept the uncomfortable truth that, just like death, cancer is a natural phenomenon we cannot avoid. But the suffering and fear of cancer is simply too great to accept it gracefully.

When diagnosed with diabetes or hypertension, we simply remind ourselves to be cautious and take care of ourselves. They are, after all, conditions we can control by taking drugs. This leads to the question: why can't treating cancer be more like treating hypertension? Can't cancer be something we can deal with through treatment, even if more complex or painful? Treatment for chronic diseases such as hypertension and diabetes control the function of cells. Cancer treatment, on the other hand, aims to kill the cancer cells. Treatment for cancer until now has involved injecting as much of the targeting drugs as the patient could tolerate. As a side effect of this process, normal cells are also attacked, often causing considerable pain to the patients. Furthermore, despite such drastic treatments, cancer cells frequently survive. A living organism's nature to survive and reproduce is the reason why it is so difficult to eradiate cancer.

Looking at a cancer cell as a living organism makes it easy to understand this. Just like any microorganism, a cancer cell constantly undergoes cell division, and if its environment changes, it will do all it can to adjust to the changes through mutation. An example of this is the endless arms race between researchers developing antibiotics and viruses resisting them. Likewise, we are witnessing a never-ending arms race between cancer treatments and cancer cells. If we view viruses as something we can never eradicate, perhaps we can also view cancer in terms of coexistence rather than something we need to conquer.

Yet we are faced with another uncomfortable truth. A person entirely cured of cancer is two to three times more likely to be diagnosed again with cancer compared to those with no cancer history. The more advanced cancer treatments become, the longer people will live, and this increases the number of people who are highly likely to develop cancer again. This leads to a contradiction that the more we develop technologies to eradicate cancer, the more we are likely to be diagnosed with it. We have to realize the inevitable truth that since all our body cells can potentially become cancer cells, we must learn to live not only with healthy cells, but also those that go rogue.

The reason President Obama once again announced a war on cancer is because carcinogenic strategies using the immune system had started to show results. Despite remarkable progress, however, immunotherapy has so far been effective against only a few forms of cancer and in less than 30% of patients treated. Many patients are still left with no effective cure. So the conclusion must be, while there is a ray of hope, the light is still too weak and we must accept the notion of living with the disease as we continue to search for ways to improve treatments.

"Think as a physicist, and work as an engineer"

Interview with Dr. Young Wook CHO from Center for Quantum Information

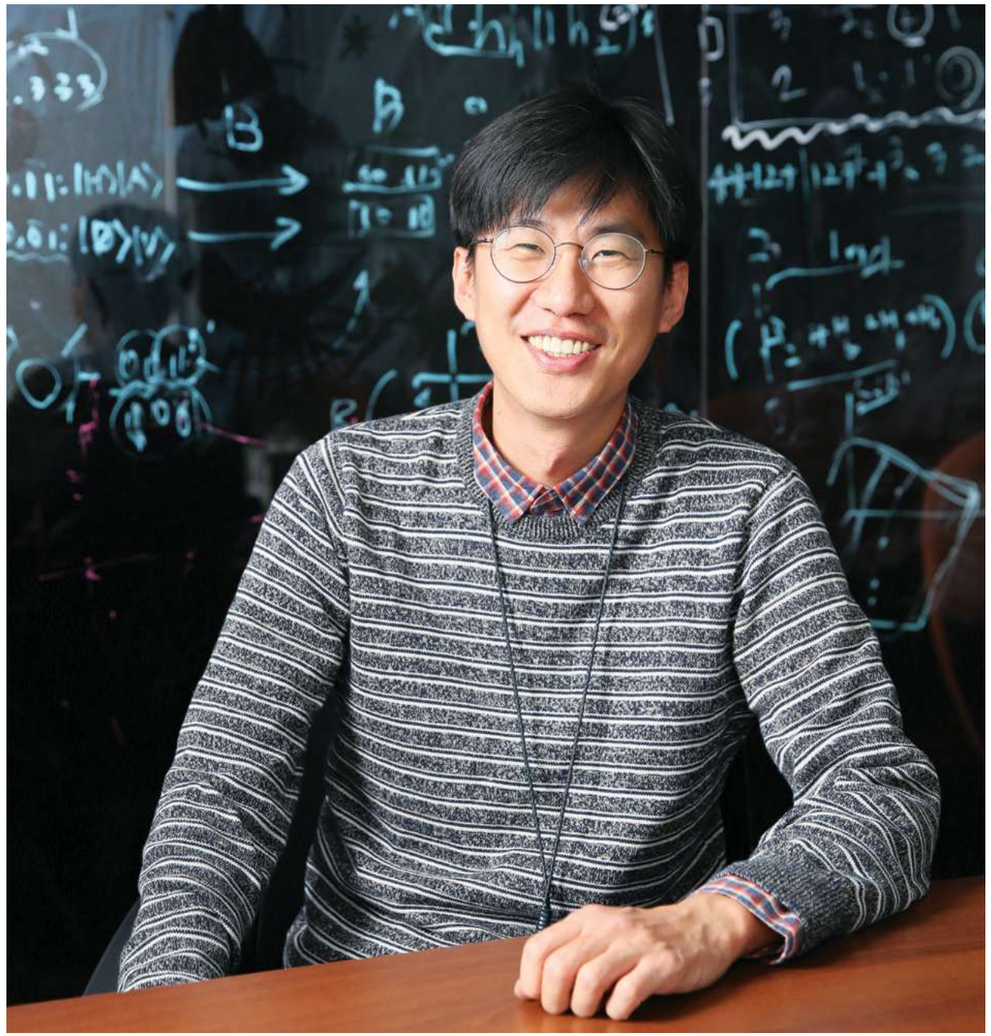

Quantum computers, which outperform supercomputers, are currently the center of global scientific interest. Dr. Young Wook CHO from KIST's Center for Quantum Information, in concert with a team from Pohang University of Science and Technology (POSTECH) led by Prof. Yoon Ho KIM, has discovered a new method to efficiently verify the quantum computing process.

How did you begin this research?

The research was part of the quantum computing Open Research Program (ORP), which took a slightly different approach compared to typical research projects. Normally, applicability is paramount when considering research outcomes, which is why research is usually conducted on performance-enhancing technologies with predetermined applications in mind. But this research began without such a consideration. It began instead with a single goal: the experimental measurement of the sequential weak value—a rather special method of quantum measurement. Our calculations during the experimental design phase demonstrated that it could assist with quantum process tomography, a technique for analyzing the quantum computing process.

Research overview

The uncertainty principle in quantum physics states that two incompatible observables can't be measured simultaneously. For example, you can't determine the exact position and momentum of a certain particle at a given point, because the act of quantum measuring collapses the quantum state. We therefore used the sequential weak value measurement technique to prevent complete disturbance of the quantum state and, in this way, succeeded in measuring incompatible observables. This quantum measurement technique enabled us to demonstrate, through experiments using a single-photon qubit, the possibility of a new and efficient way to verify the quantum computing process.

Research conducted in cooperation with other teams

Conducting an ORP project meant that we cooperated with other teams on the research. We didn't experience any difficulties or conflict with this arrangement; on the contrary, it helped produce results faster, giving us a distinct advantage. In the fiercely competitive world of research, you must race to publish your findings before another team beats you to it. Speed is imperative. In my case, I was able to put theory into practice at a much faster pace thanks to our collaborative arrangement with POSTECH.

What made you study quantum information and what do you like most about quantum physics?

To be honest, I didn't choose physics—or specifically, quantum information—as my major for any special reason. When I was an undergraduate, I had the chance to participate in a graduate school research project in a

Interview

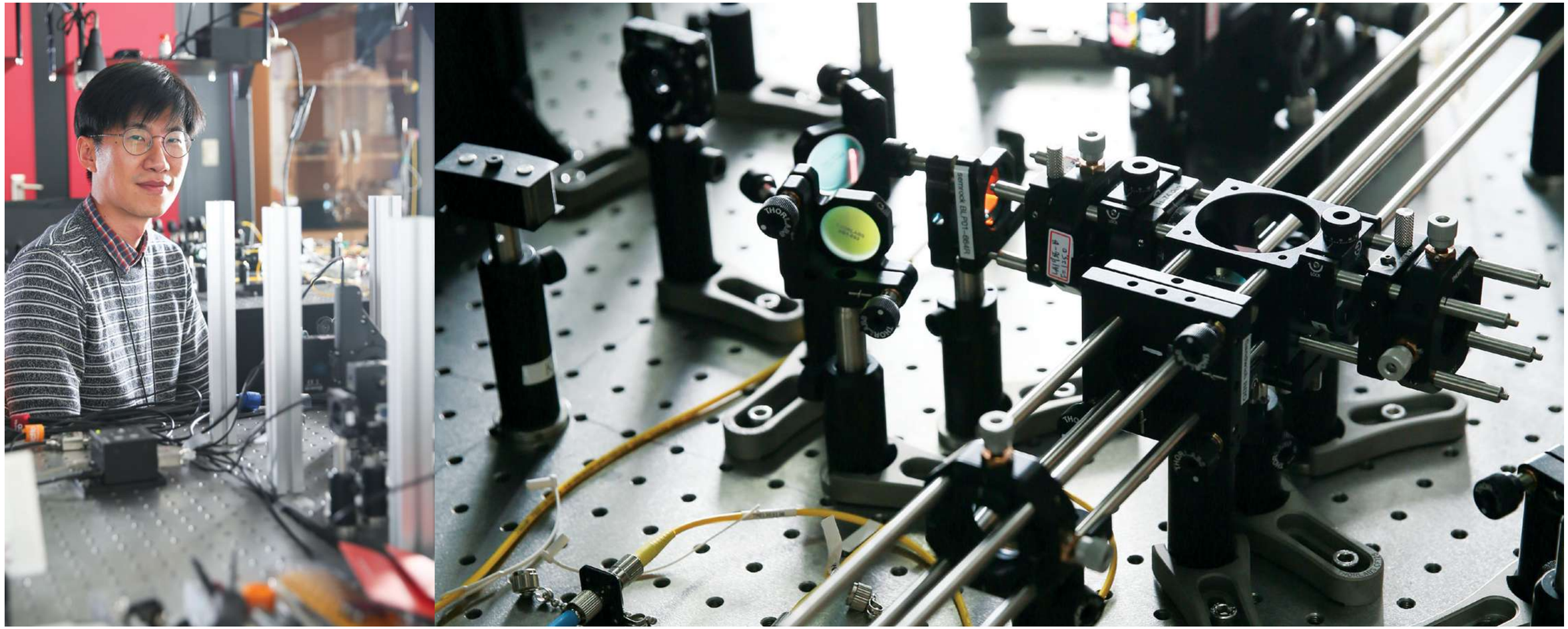

quantum optics/quantum information lab. I participated for just a few months, but eventually chose this field because of the professor and good lab atmosphere.

Afterwards, the more I did research on quantum information technology, the more attracted I was to this field. Research on quantum information technology is mostly fundamental research on quantum physics. I'm personally interested in fundamental research, also known as basic science, but such research is difficult to justify or explain. Because unlike quantum information, it has no direct application.

How are classical physics and quantum physics different?

I think the biggest difference lies in the concept of measurement. In classical physics, or measurement in general, the act of measuring something doesn't alter its physical quantity. For example, you don't change the length of a desk simply by measuring it. But in quantum physics, measurement is an action that causes the quantum state to collapse, resulting in an eigenstate. This, I believe, is the biggest difference between the two fields.

A difficult area of research to explain

Since research into quantum physics is so difficult to explain in terms of classical physics, I use metaphors to make explanation easier—though the metaphors are often misunderstood, too. Explaining our research is every bit as difficult as conducting it, and this holds true not just for the scientific layman but for scientists and engineers, as well. For example, when my daughter recently asked me the meaning of "quantum" after watching the movie Ant-Man and the Wasp, I found myself struggling to answer.

Possible applications for quantum information technology

There are three primary application areas for quantum information technology: quantum computing, quantum communications, and quantum sensors. All three sound confusing with the word "quantum" attached.

The closest that our center comes to research with commercialization potential is in regard to quantum cryptography, which is the primary research focus of Dr. Sung Wook MOON and Dr. Sang Wook HAN. Our center developed equipment for a quantum cryptography network, and we currently collaborate with KT to test the equipment both in the lab and out in the real world.

Do you think quantum computers will be commercialized?

This is the hardest, most frequently asked question I receive. Truthfully, I don't know. But quantum information is no longer just a theory. Back in 2000, the field of quantum information was brand new, and when I started working on my degree in the late 2000s, few people had any idea of how to put quantum information to practical use. But these days, the potential for commercialization is often discussed, and there is increased interest within the private sector. So, commercialization has become a real possibility.

How is quantum information technology different from other technologies?

The biggest difference is that, to develop new quantum information technologies, you need collaboration between scientists and engineers. By its very nature, the field is rooted in physics, and without an understanding thereof, you can't expect to get anywhere. At the same time, quantum information technology is created by controlling "quantum," and this can't be done without help from engineers. I believe the phrase "Think like a physicist and work like an engineer" expresses the right approach to developing new quantum information technologies.

Research outlook

The biggest problem the field of quantum information faces today is too few researchers, which is why we need to make a greater investment in this kind of training. Next, we must establish a long-term vision for the research we do. For example, when it comes to quantum computing, research on ion traps and superconductivity currently leads the field. But such research has only been around for a decade or so, and we don't really know where the future will take us. At present, our research into a hybrid system of solid-state point defect qubits and photonic qubits is a latecomer in the field, but there is a good chance it will lead to a future source technology.

Science Cartoon

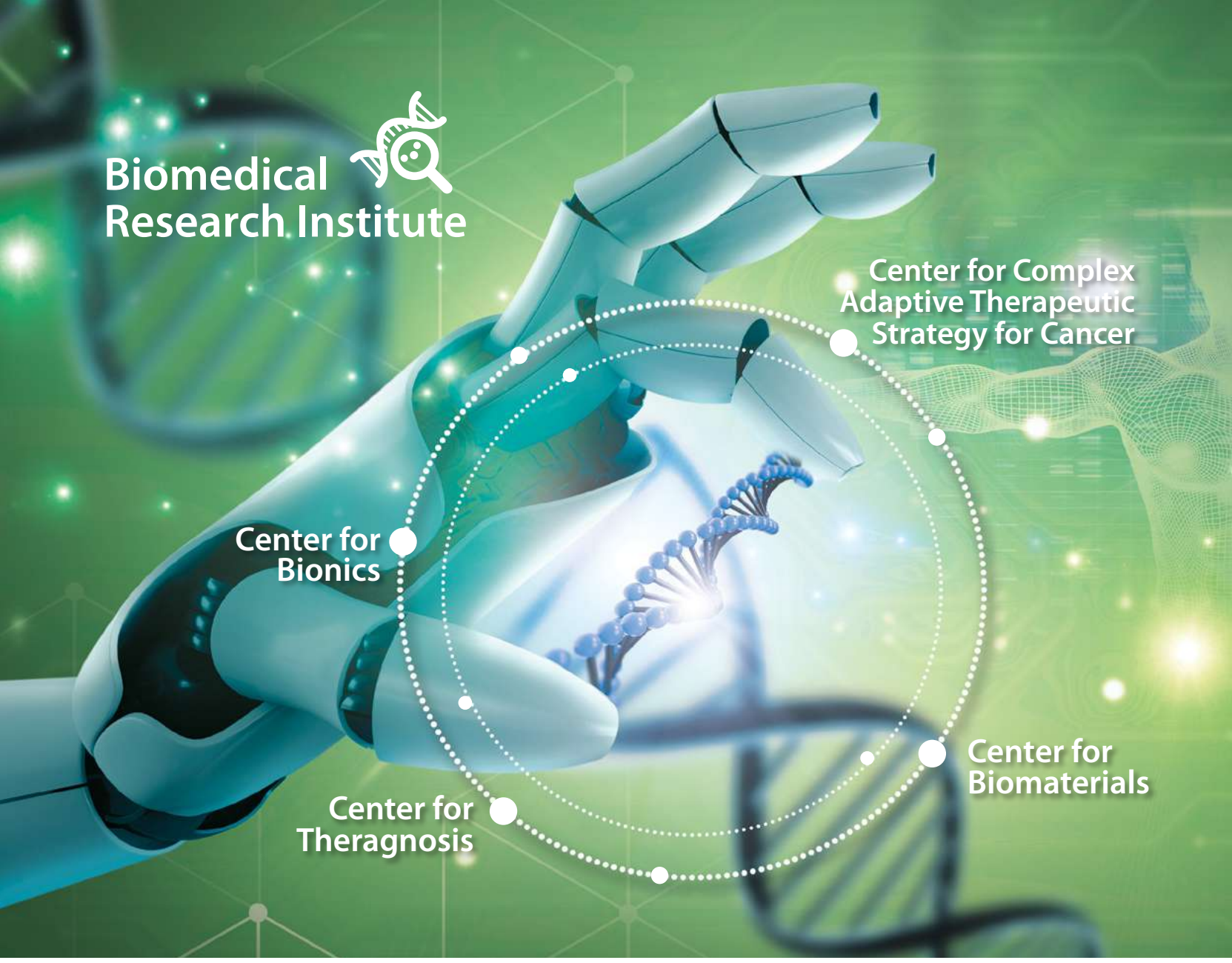

Biomedical Research Institute

We are dedicated to improving human health and quality of life by developing revolutionary technologies for unmet biomedical needs

As KIST is seeking ways for people to live longer and healthier, the KIST Biomedical Research Institute is committed to integrating the engineering and biological sciences with the clinical sciences to lead biomedical innovation. We develop cognitive and physical rehabilitation technologies to promote quality of life for the elderly and/or disabled, and devise strategies for repair-and-regeneration, and functional materials for replacing human tissues and organs. The institute is also heavily involved in the study of cutting-edge medical technologies enabling improved diagnosis and treatment for personalized medicine, thereby positioning itself as the epicenter of biomedical research in Korea.

KIST
Korea Institute of
Science and Technology